

**Statistical considerations in high precision U-Pb
geochronology, with an application to the tectonic
evolution of the North Cascades, Washington**

by

Noah Morgan McLean

B.S., University of North Carolina, Chapel Hill (2004)

Submitted to the Department of Earth, Atmospheric, and Planetary
Sciences

in partial fulfillment of the requirements for the degree of

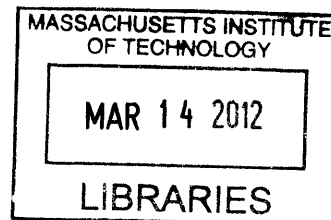
Doctor of Philosophy

at the


MASSACHUSETTS INSTITUTE OF TECHNOLOGY


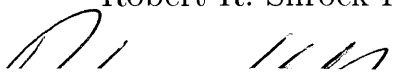
February 2012

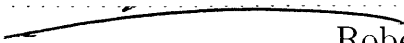
ARCHIVES



© Massachusetts Institute of Technology 2012. All rights reserved.

Author
Department of Earth, Atmospheric, and Planetary Sciences
 December 16, 2011

Certified by.....
 Samuel A. Bowring
Robert R. Shrock Professor of Geology
 Thesis Supervisor

Accepted by.....
 Robert D. van der Hilst
Schlumberger Professor of Geosciences
Head, Department of Earth, Atmospheric and Planetary Sciences

**Statistical considerations in high precision U-Pb
geochronology, with an application to the tectonic evolution
of the North Cascades, Washington**

by

Noah Morgan McLean

Submitted to the Department of Earth, Atmospheric, and Planetary Sciences
on December 16, 2011, in partial fulfillment of the
requirements for the degree of
Doctor of Philosophy

Abstract

The range of geologic problems that may be addressed by U-Pb geochronology is governed by the precision to which U-Pb dates can be measured, expressed as their estimated uncertainties. Accurate and precise knowledge of both the value and uncertainty of an isotopic date are imperative to its correct interpretation. This thesis focuses on quantitatively addressing the large volume of information that contributes to the calculation of published high-precision U-Pb dates. A new algorithm (Chapter 2) outlines the equations that transform measured isotope ratios, along with a host of laboratory and instrumental parameters, into a U-Pb date. The algorithm propagates all known random and systematic uncertainties, resulting in an adaptable framework will remain usable as analytical and computational advances change the main uncertainty contributions. The data reduction and uncertainty propagation algorithm, as well as a new method for calculating weighted means that correctly treats systematic uncertainties, have been incorporated into the open-source software program U-Pb_Redux. Chapter 3 explores the mechanisms of isotopic fractionation, the largest instrumental correction to measured U-Pb data, using a new linear regression algorithm. The algorithm rapidly regresses a straight line through large datasets in multiple dimensions using a novel simplification to the maximum likelihood objective equation, and is used to demonstrate that Pb undergoes mass-independent fractionation in the source of a thermal ionization mass spectrometer. Chapter 4 addresses the largest source of systematic uncertainty considered when confederating datasets from different labs, the calibration of the tracer used for isotope dilution. The calibration assumes only first-principles mass and purity measurements traceable to SI units, then defines a measurement model that utilizes $>10^5$ measurements in a series of overdetermined inverse problems to estimate the tracer isotopic composition. The result is a reduction by a factor of almost four in the tracer uncertainty contribution to a U-Pb date. In Chapter 5, I use the new algorithms to explore regional geology. High-precision U-Pb dates from the metamorphic core of the North Cascades

and from ash beds in three fluvial basins that flank it show that Eocene magmatism, solid-state deformation, and exhumation of the metamorphic core are coincident with rapid basin subsidence.

Thesis Supervisor: Samuel A. Bowring

Title: Robert R. Shrock Professor of Geology

Acknowledgments

I would like to thank my family and friends for their support, and in particular the past and present denizens of the MIT Isotope Geochemistry Laboratory, who have become both family and friends.

Contents

1	Introduction	15
2	An Algorithm for U-Pb Isotope Dilution Data Reduction and Uncertainty Propagation	21
2.1	Introduction	22
2.2	U-Pb Data Reduction	24
2.2.1	Inputs	25
2.2.2	Data Reduction	28
2.3	Uncertainty Propagation Principles	39
2.3.1	Determining the Uncertainties of Inputs	39
2.3.2	Uncertainty Propagation Equation	41
2.3.3	Covariance and Correlation	43
2.4	Propagating Uncertainty with Matrices	44
2.4.1	Covariance and Jacobian Matrices	45
2.4.2	Calculating the Total Derivative	47
2.4.3	Uncertainty Propagation Equation	49
2.5	Weighted Means	50
2.5.1	Conventional Weighted Mean of Independent Data	50
2.5.2	The Date Covariance Matrix	52
2.5.3	Generalized Weighted Mean of Correlated Data	54
2.5.4	Application to U-Pb Geochronology	57
2.6	Verification by Monte Carlo Method	58
2.6.1	Monte Carlo Experimental Setup	59

2.6.2	Results	60
2.7	Conclusions	61
2.8	Appendix: Disequilibrium Corrections and Initial Common Pb Models	62
2.8.1	Th correction derivation	63
2.8.2	Th correction implementation	66
2.8.3	Pa correction	68
2.8.4	Simultaneous Th- and Pa-correction	69
2.8.5	Initial Common Pb Correction	69
2.9	Figure captions	71

3 Straight Line Regression through Data With Correlated Uncertainties in Two or More Dimensions **79**

3.1	Introduction	80
3.2	Estimation of Regression Parameters	83
3.2.1	Vector from a Point to a Line	83
3.2.2	Maximum Likelihood and the Minimum Distance	84
3.2.3	Probability Density and Likelihood Functions	87
3.3	Solving for the Best Fit Line	88
3.3.1	Uncertainty in Fit Parameters	89
3.3.2	Other Linear Regression Algorithms	90
3.4	Application to Kinetic Isotope Fractionation	92
3.4.1	Rayleigh and Exponential Fractionation Equations	93
3.4.2	Application to Pb Measurements by TIMS	95
3.5	Isochrons, Mixing Lines, and the Statistics of Compositional Data . .	98
3.5.1	Some Pitfalls of Conventional Multivariate Statistics for Isotope Ratios	99
3.5.2	Application of Compositional Data Methods to Exponential Mass Fractionation	100
3.6	Summary and Conclusions	102

3.7	Appendix A: Second Derivatives of log-Likelihood Equation for Best Fit Line	103
3.8	Appendix B: Multivariate weighted mean	103
3.9	Figure captions	105
4	Evaluating Analytical and Systematic Uncertainty in Mixed U-Pb Tracer Calibration	111
4.1	Introduction	112
4.1.1	First Principles	113
4.2	Application of Inverse Methods	115
4.2.1	Measurement Model	115
4.2.2	Solving the Inverse Problem	116
4.3	Inter-calibration of Pb and U standards	118
4.3.1	U Standard Inter-calibration	119
4.3.2	Pb Standard Inter-calibration	119
4.4	Determining the Pb IC of the Tracer and Blank	126
4.4.1	Determining the mixing line parameters	127
4.4.2	Results	130
4.4.3	Application to TIMS Pb measurements	131
4.5	Determining the U IC of the Tracer with Critical Mixtures	132
4.5.1	Model	133
4.5.2	Algorithm and Results	135
4.5.3	Correlation with Sample $^{238}\text{U}/^{235}\text{U}$	136
4.5.4	Sample Fractionation Correction with a ^{233}U - ^{235}U Tracer	137
4.6	U/Pb Ratios of the Gravimetric Standards	138
4.6.1	Uncertainty in Mass Determinations	138
4.6.2	Uncertainty in Purity of Pb Isotopic Standards	139
4.6.3	Purity of U Isotopic Standards	141
4.6.4	Gravimetric U/Pb ratio	141
4.7	Gravimetric-Tracer Mixtures	142

4.7.1	Equations	142
4.7.2	Algorithm and Results	145
4.8	Discussion	146
4.9	Conclusions	148
4.10	Figure captions	150
5	Exhumation of the North Cascades core coincident with rapid sedi- mentation in adjacent nonmarine basins	161
5.1	Introduction	162
5.2	Geologic Setting	162
5.3	U-Pb dates in the Skagit Gneiss	163
5.4	U-Pb dates in non-marine basins	165
5.5	Discussion	166
5.6	Conclusions	167

List of Figures

2-1	Flow chart for U-Pb data reduction	75
2-2	U-Pb sample components	76
2-3	Uncertainty propagation in one dimension	77
2-4	Monte Carlo simulation results	77
3-1	Linear regression parameters	108
3-2	Maximum likelihood by Cholesky transformation	108
3-3	Observed isotopic fractionation for a single analysis of NBS 982	109
4-1	Mass independent fractionation of Pb.	156
4-2	Monte Carlo simulations of the best-fit value of $^{208}\text{Pb}/^{206}\text{Pb}$ of NBS 982.	157
4-3	Measurements of the laboratory Pb blank isotopic composition.	158
4-4	Probability distribution functions for the purity of four commonly used Pb standards.	158
4-5	Relative uncertainty contribution (2σ , ppm) to the $^{206}\text{Pb}/^{238}\text{U}$ date from uncertainty in the tracer IC.	159
5-1	North Cascades map and U-Pb data	168

List of Tables

2.1	Measured Isotope Ratios	73
2.2	Isotopic Tracer Parameters	73
2.3	Laboratory and Sample Parameters	74
3.1	Maximum likelihood estimates, uncertainties, and correlation coefficients for the best fit line parameters to the NBS 982 Pb fractionation data.	107
4.1	Weighted mean $^{238}\text{U}/^{235}\text{U}$ values and their random, and combined random and systematic uncertainties for the U isotopic standards CRM 112a, CRM 115, and CRM U500 used for tracer calibration. Reported ratios are all fractionation-corrected using IRMM 3636(a) (Verbruggen et al., 2008) for fractionation correction.	152
4.2	Matrix of correlation coefficients between the uncertainties reported in Table 4.1	152
4.3	Least squares solutions, random, and combined random and systematic uncertainties for the the Pb isotopic standards NBS 981, NBS 982, and Puratronic Pb used for tracer calibration, calculated with data reported in Amelin and Davis (2006)	153
4.4	Matrix of correlation coefficients between the uncertainties in the Pb ICs used for tracer calibration. These uncertainties are correlated because they share common sources of uncertainty, largely due to common ratios being used for the fractionation correction. Correlation coefficients close to -1 or 1 indicate a high degree of correlation. . . .	153

4.5	Results of linear fit for tracer - blank mixing line	154
4.6	Correlation coefficient matrix for ET535 and loading blank Pb IC. . .	154
4.7	Derivatives of the U IC of ET(2)535 with respect to IRMM 3636. These values can be used to determine the covariance between a measured $^{238}\text{U}/^{235}\text{U}$ and the tracer, for propagating uncertainty in U-Pb dates.	154
4.8	The U isotopic composition of ET(2)535 from the critical mixture experiment. The tracer was mixed with CRM 112a and SRM U500, whose ICs, uncertainties, and correlation coefficient are given in Section 4.3.1.	155
4.9	Purities of Pb isotopic standards measured by glow discharge mass spectrometry, with estimated symmetric 95% confidence intervals . .	155
4.10	Results of the gravimetric solution - tracer mixtures.	155
5.1	U-Pb Data Table 1	169
5.2	U-Pb Data Table 2	170
5.3	U-Pb Data Table 3	171

Chapter 1

Introduction

The power of a high-precision U-Pb dataset largely lies in the techniques ability to produce an absolute measure of geologic time with the smallest possibly uncertainties. Indeed, the range of geologic problems that U-Pb data is employed to solve, from global timescale calibration to regional geologic correlations, is determined by the achievable precision. At the cutting edge of geochronology awaits new discoveries made possible by technical and computational improvements and the insights they afford. This thesis takes a statistical approach to the analysis of U-Pb geochronological data, and seeks to provide the tools required for the next generation of U-Pb geochronology.

As U-Pb analytical techniques have advanced, formerly small sources of uncertainty have become increasingly important, and thus previous simplifications for data reduction and uncertainty propagation are no longer valid. Newly prominent analytical uncertainty contributions include instrumental and laboratory parameters, like the isotopic composition of the laboratory Pb blank and the magnitude and even the mode of isotopic fractionation. Uncertainty contributions from systematic effects include the isotopic composition of the tracer used for isotope dilution calculations. These uncertainty components combine to determine the overall uncertainty budget of a U-Pb analysis.

Although previous efforts have treated propagation of correlated uncertainties for the U-Pb system, the equations, uncertainties, and correlations have been limited in

number and subject to simplification during propagation through intermediary calculations. Chapter 2 provides a new computational framework for U-Pb data reduction and uncertainty propagation using linear algebraic methods. Rather than modifying notable past algorithms, this contribution re-derives the governing equations that transform the raw data and inputs for U-Pb geochronology into U-Pb and Pb-Pb dates. A linear uncertainty propagation algorithm with an important extension for systematic uncertainties is proved to approximate the true probability density functions of all calculated U-Pb and Pb-Pb dates to sufficient numerical precision using Monte Carlo methods.

The contents of this chapter have been previously published in an article in *Geochemistry, Geophysics, Geosystems*: McLean, N. M., Bowring, J. F., and Bowring, S. A. (2011) An algorithm for U-Pb isotope dilution data reduction and uncertainty propagation. *Geochem. Geophys. Geosyst.* doi: 10.1029/2010GC003478 along with a companion paper that describes an open source software package, U Pb_Redux, that employs the new algorithms to create a dynamic visualizations and archive the data in a public database.

Chapter 3 delves more deeply into the statistics of isotope ratio data. Linear regression algorithms are used frequently for measured data that contain non-negligible uncertainties in each variable. The highly-cited algorithm of York (1968) solves the linear regression problem for data with correlated uncertainties in two dimensions, but it omits an important term for evaluating confidence intervals about the regression line and it is not generalizable to higher dimensions. I apply the maximum likelihood method to determine the best-fit line and its uncertainty through data with correlated uncertainties in any number of dimensions, notably simplifying the resulting vector equations for rapid computation.

The new algorithm is then used to reduce a large dataset of highly time-resolved Pb measurements made with a silica gel activator on a thermal ionization mass spectrometer (TIMS). I test the commonly made assumption that isotopic fractionation, or the preferential evaporation, ionization, and detection of lighter isotopes over heavier ones, is exponentially mass-dependent. If this hypothesis is true, then the measured

data should fall along a line in log-ratio space with a predictable direction vector (slope). Instead, measured isotope log-ratios fall along a different line, whose direction vector components with odd-numbered isotopic mass (here, ^{207}Pb) is significantly different than those predicted by the mass-dependent theory. This mass-independent fractionation (MIF) effect has been described for other isotopic systems, such as Cd, Hf, Hg, and Tl in natural and laboratory settings, but it has never been shown to act systematically on Pb analyses.

The discovery and quantification of systematic MIF during Pb analyses using the new linear regression algorithm impacts high precision U-Pb dates. The degree of MIF observed in this paper and in Chapter 4 would increase the estimated amount of ^{206}Pb by up to 0.03%, depending on analytical parameters. This change would make $^{206}\text{Pb}/^{238}\text{U}$ dates, which play an important role in Phanerozoic timescale calibration, older by close to the same factor, and $^{207}\text{Pb}/^{206}\text{Pb}$ dates, which are used to date Paleozoic and older rocks and meteorites, younger by about 0.01%. Both of the changes are significant compared with the analytical uncertainties achievable on weighted means of large datasets.

This chapter will be submitted to *Geochimica et Cosmochimica Acta*.

Chapter 4 applies many of the techniques and results of Chapters 2 and 3 to the problem of calibrating a mixed U-Pb isotopic tracer created by the EARTHTIME initiative to facilitate collaborative timescale calibration. Because a thermal ionization mass spectrometer is not capable of measuring Pb and U at the same time, the ratio of U and Pb, and therefore the U-Pb date of a sample, cannot be directly determined by TIMS. Instead, an isotopic tracer with known amounts of the artificially enriched isotopes ^{235}U and ^{205}Pb are added to the sample, and the sample and tracer are measured together. The ratios of the sample to the tracer isotopes for each element are then combined with the ratio of ^{235}U to ^{205}Pb in the tracer to indirectly determine the samples U/Pb ratio, a method known as isotope dilution (the ID in ID-TIMS). In this way, all sample U/Pb ratios are measured relative to the tracer U/Pb ratio.

To determine the U/Pb ratio of the tracer, I assume only measurements that can be traced back to first principles measurements of mass and purity, and therefore to SI

units. These systematic uncertainties are then propagated through a series of inverse problems that combine data measured from mixtures of the tracer and gravimetrically calibrated solutions to constrain the isotopic composition (IC) of the tracer. As an intermediate step, the ICs of many important Pb and U standards are inter-calibrated with one another and for the first time relate their uncertainties to one another and back to SI units. The tracer calibration uncertainty derived in this way is smaller by a factor of almost four than previously assumed, reducing an important component of systematic uncertainty common to all U-Pb analyses made with the EARTHTIME tracers. Other tracers may be calibrated using the same numerical methods and fundamental assumptions, facilitating inter-laboratory comparison and collaboration at the sub-per-mil level.

This chapter will be submitted, along with a companion paper that describes the creation of the EARTHTIME tracers, to *Geochimica et Cosmochimica Acta*.

The fifth and final chapter of this thesis explores the application of high-precision U-Pb geochronology to the geology of the North Cascades, Washington. The North Cascades metamorphic core is the southern terminus of the Coast Plutonic Complex, and represents the exhumed root of a Cretaceous continental magmatic arc. Biotite, muscovite, and hornblende ^{40}Ar - ^{39}Ar cooling dates from the Cascades core overlap at ca. 45-48 Ma and imply rapid Eocene exhumation. Flanking the Cascades core is a series of deep nonmarine, fault-bounded basins that have long been thought to be the same age. A major unresolved question in the geologic history of the North Cascades is how the two are related.

Using U-Pb dates of zircons in igneous intrusion with solid-state deformation throughout the metamorphic core of the North Cascades, I demonstrate a previously unrecognized widespread episode of Eocene magmatism that follows a period of Paleocene quiescence. Three nonmarine basins contain volcanic tuffs with depositional ages that overlap with the timing of magmatism in the metamorphic core and ^{40}Ar - ^{39}Ar cooling ages. Taken together, available age constraints imply a dynamic relationship between rapid basin development and exhumation of the North Cascades core, consistent with a degree of coupling between the upper and lower crust during

the major plate transition to the modern Cascades arc.

This paper was written for submission to *Geology*.

Chapter 2

An Algorithm for U-Pb Isotope Dilution Data Reduction and Uncertainty Propagation

Abstract

High precision U-Pb geochronology by isotope dilution thermal ionization mass spectrometry (ID-TIMS) is integral to a variety of earth science disciplines, but its ultimate resolving power is quantified by the uncertainties of calculated U-Pb dates. As analytical techniques have advanced, formerly small sources of uncertainty are increasingly important, and thus previous simplifications for data reduction and uncertainty propagation are no longer valid. Although notable previous efforts have treated propagation of correlated uncertainties for the U-Pb system, the equations, uncertainties, and correlations have been limited in number and subject to simplification during propagation through intermediary calculations. We derive and present a transparent U-Pb data reduction algorithm that transforms raw isotopic data and measured or assumed laboratory parameters into the isotopic ratios and dates geochronologists interpret without making assumptions about the relative size of sample components. To propagate uncertainties and their correlations, we describe, in detail, a linear al-

gebraic algorithm that incorporates all input uncertainties and correlations without limiting or simplifying covariance terms to propagate them through intermediate calculations. Finally, a weighted mean algorithm is presented that utilizes matrix elements from the uncertainty propagation algorithm to propagate random and systematic uncertainties for data comparison between other U-Pb labs and other geochronometers. The linear uncertainty propagation algorithms are verified with Monte Carlo simulations of several typical analyses. We propose that our algorithms be considered by the community for implementation to improve the collaborative science envisioned by the EARTHTIME initiative.

2.1 Introduction

U-Pb geochronology by isotope dilution thermal ionization mass spectrometry (ID-TIMS) has become the gold standard for calibrating geologic time due to precisely determined uranium decay constants, high-precision measurement methods, and an internal check for open-system behavior provided by the dual decay of ^{235}U and ^{238}U . Precise, accurate ID-TIMS dates have been used to test and calibrate detailed tectonic models (e.g. Schoene et al. (2008)), determine the timing and tempo of mass extinctions and ecological recovery (Bowring et al., 1998), calibrate a global geologic timescale (Davydov et al., 2010), and establish a precise chronology for the early solar system (Amelin et al., 2002). These results rely on analysis and interpretation of precisely measured data, for which correct and transparent data reduction and error propagation are imperative.

U-Pb ID-TIMS dates are measured by dissolving a U-bearing phase with a mixed isotopic tracer enriched in isotopes of U and Pb, then purifying the U and Pb from the resulting solution. The ratios of Pb and U in the sample to those in the tracer are measured precisely by TIMS to determine radiogenic isotope ratios of U and Pb, which are used to calculate dates. The relatively high precision of ID-TIMS dates stems from clean laboratory protocols, which minimize the magnitude and uncertainty of the laboratory blank correction, stable isotope beams with per mil

level isotopic fractionation, which minimize measurement uncertainties, and well-characterized isotopic tracers, which leverage the ability of the TIMS to accurately measure isotope ratios. The accuracy of the most common geochronometer, zircon, is greatly enhanced by the chemical abrasion method, or CA-TIMS (Mattinson, 2005a), which minimizes or eliminates any correction for loss of Pb.

The last decade of developments in mass spectrometry, clean laboratory protocols, and pre-treatment of zircons has increased measurement precision and decreased the magnitude of corrections for common Pb (Pbc) and open system behavior. However, the algorithms presently used for U-Pb data reduction and uncertainty propagation still maintain many simplifications and omissions better suited to past datasets. Furthermore, as random sources of uncertainty, such as ion counting statistics, have been reduced, systematic uncertainties such as calibration of the isotopic tracer have come to dominate the overall uncertainty budget. Thus, the quality of data has outstripped the algorithms for data reduction.

Several recent inter-laboratory comparisons between established ID-TIMS U-Pb geochronology labs have revealed statistically significant discrepancies in measurements of the same samples. These differences likely arise from the now dominant systematic uncertainties, and represent a significant impediment to data inter-comparison in collaborative science. In order to achieve the external reproducibility required by, for example timescale calibration, a common framework that transforms raw data into geological interpretation and correctly propagates systematic uncertainties is critical. The geochronology community would be well served by agreeing upon and adopting a universally accepted data reduction and uncertainty propagation algorithm for publishing and archiving data.

Rather than modifying notable past data reduction and uncertainty propagation algorithms (e.g., Ludwig, 1980; Roddick, 1987; Schmitz and Schoene, 2007), this contribution re-derives the governing equations that transform the raw data and inputs for U-Pb ID-TIMS geochronology into U-Pb and Pb-Pb dates. The equations support dating U-bearing phases with and without initial common Pb, use of several mixed U-Pb tracers, and include corrections for initial daughter isotope disequilibrium and

for time-varying instrumental parameters like isotopic fractionation.

A novel algorithm for propagating the input uncertainties precludes neglecting or simplifying terms in the complicated expressions for the uncertainty of U-Pb dates, thus incorporating all known sources of error. Utilizing matrices of covariance terms and partial derivatives, the uncertainty propagation algorithm also determines the statistical relationships between the U-Pb and Pb-Pb dates and is capable of breaking down the uncertainty contributions from individual sources. Contributions to the combined uncertainty from random and systematic components can then be propagated separately for each analysis, including only those systematic uncertainties necessary to compare datasets. This algorithm is extensible, so that it can accommodate future improvements in analytical methods and the uncertainty correlations arising from tracer calibrations or inter-calibrated U decay constants.

Data reduction and uncertainty propagation algorithms are packaged in the open-source, publicly distributed program *U-Pb_Redux*, which includes a laboratory workflow manager and an interactive graphical user interface that performs statistical calculations and plotting (Bowring et al., 2011). *U-Pb_Redux* is also capable of exporting all of the calculated dates, interpretations, and supporting data to an online database, then downloading datasets for further interpretation and compilation with new data from multiple users. Community adoption of a common, transparent algorithm like the one in *U-Pb_Redux* would ensure that data from different users in different labs can be compared and combined.

2.2 U-Pb Data Reduction

A number of corrections and calculations are required to transform measured isotopic ratios and lab parameters into meaningful isotopic dates, as illustrated in Figure 2-1. If isobaric interferences are present, they must be measured and subtracted before each isotope ratio is corrected for instrumental mass fractionation, or mass bias, caused by lighter isotopes evaporating and ionizing more easily than heavier isotopes. The numerator and denominator of a measured, corrected isotope ratio then repre-

sent mixtures of multiple components: the parent or radiogenic daughter isotope; the isotopic tracer used; common Pb and U added during laboratory procedures, known as laboratory blank; and if present, initial common Pb incorporated during crystallization of the phase (Figure 2-2).

There are three ways to calculate isotopic dates from fractionation- and interference-corrected ratios. If the isotopic composition (IC) of the common Pb components are known, they may be subtracted along with the tracer contribution to directly determine radiogenic isotope ratios; along with appropriate decay constants, these determine the isotopic date. Alternatively, after subtracting the estimated laboratory blank and isotopic tracer contributions, the resulting isotope ratios may represent variable mixtures of a single initial common Pb isotopic composition and an amount of radiogenic Pb proportional to the amount of parent isotope present. Assuming a closed system, both the sample date and the isotopic composition of the initial common Pb can be calculated using an isochron technique. Finally, a linear regression through discordant U-Pb analyses can be extrapolated to concordia intercepts that may be interpreted in terms of a single episode of open system behavior.

This section explores the inputs required and the mechanism used for accurate U-Pb data reduction. Text accompanying each equation in the data reduction algorithm explains its applicability and purpose.

2.2.1 Inputs

A weighted mean, isochron, or concordia intercept date is calculated from a number of paired U and Pb analyses, here termed ‘fractions’ (Bowring et al., 2011). Examples include single mineral grains or grain fragments, as well as a bulk leach or a whole rock analysis. Between twenty and forty separate input variables are required to calculate an isotopic date for each fraction, and each is described below. These inputs, as well as the symbols used to represent them in the following data reduction algorithm, are listed in Table 2.1, Table 2.2, and Table 2.3.

All data must be reduced with a self-consistent set of physical constants, such as decay constants and atomic masses. Decay constants used for isotopic date calcu-

lation and disequilibrium correction include those for ^{231}Pa , ^{230}Th , ^{232}Th , ^{235}U , and ^{238}U . The atomic masses of the isotopes, which are the only inputs not assigned an uncertainty, are used to convert between masses and moles of elements or isotopes.

An isotopic tracer is a mixture of well-determined quantities of enriched isotopes. The equations presented here apply to the most commonly used isotopic tracers for U-Pb ID-TIMS geochronology, which are enriched in either ^{205}Pb or both ^{202}Pb and ^{205}Pb , as well as either ^{235}U , both ^{233}U and ^{235}U , or both ^{233}U and ^{236}U . In addition to the enriched isotopes, tracer solutions inevitably contain minor amounts of other naturally occurring isotopes, whose proportions must be known for full characterization of the U and Pb IC of the tracer. Finally, isotope dilution calculations utilize the concentrations of the artificial Pb and U isotopes (Table 2.2).

Fractions analyzed on the same mass spectrometer with the same laboratory procedures will have additional parameters in common. For elements with at least two enriched isotopes present in the tracer, isotopic fractionation during each run can be calculated either on average or point-by-point by comparing the known ratio to the measured ratio (see Sections 2.2.2, 2.2.2, and 2.2.2). However, if only one enriched isotope is present (e.g. a single ^{205}Pb or ^{235}U tracer), the magnitude and variability of mass-dependent fractionation must be assessed by repeated analyses of a standard for input to data reduction. A linear fractionation law is used here for ID-TIMS analyses, which is virtually indistinguishable from an exponential or power law correction at low (ca. 0.1% per u) magnitudes of isotopic fractionation.

Two methods to allocate common Pb are implemented in *U-Pb_Redux*. The first assumes that all common Pb (Pbc) in the analysis is laboratory blank. This assumption is justified when total procedural blank measurements are the same magnitude as the total common Pb measurements of analyses, as demonstrated for chemically abraded zircon (e.g. Davydov et al. (2010)). The laboratory blank isotopic composition should be measured for each sample preparation procedure (e.g., HCl- vs. HBr-based anion exchange chemistry), then subtracted from each analysis, as described in Sections 2.2.2 and 2.2.2.

When the dated phase contains initial common Pb, its IC can be determined

in one of three ways. With no a priori knowledge, a terrestrial Pb ore model like that of Stacey and Kramers (1975) or Cumming and Richards (1975) can be used to estimate its IC, using the approximate age of the sample. Leaching experiments on co-magmatic low-U phases such as alkali feldspar, if present, can precisely determine the initial common Pb IC (Housh and Bowring, 1991). Finally, if several fractions formed closed systems at the same time, share the same initial Pb isotopic composition, and remained closed systems until analysis, then an isochron approach may be used to solve for both their initial common Pb IC and date simultaneously.

Several additional parameters are needed to reduce U data (Table 2.3). Unless it has been determined independently, the user must specify the $^{238}\text{U}/^{235}\text{U}$ ratio of the sample. Canonically, this value has been accepted as 137.88 (Steiger and Jager, 1977), but recent studies have shown that it may vary significantly in nature (Stirling et al., 2007; Weyer et al., 2008; Brennecke et al., 2010). The mass and the $^{238}\text{U}/^{235}\text{U}$ ratio of the U blank are also necessary. Finally, if the U is measured as a UO_2^+ species with a mixed ^{233}U - ^{235}U tracer, the $^{18}\text{O}/^{16}\text{O}$ ratio of the uranium oxide is used to correct for the isobaric interferences of $^{233}\text{U}^{16}\text{O}^{18}\text{O}$ or $^{233}\text{U}^{16}\text{O}^{18}\text{O}$ on $^{235}\text{U}^{16}\text{O}^{16}\text{O}$.

Initial isotopic disequilibrium in either the ^{238}U or ^{235}U decay chains can result in systematic errors due to excess or deficit radiogenic daughter. In U-Pb geochronology, it is often assumed that the magma from which the dated phase crystallized was close to secular equilibrium. As the phase crystallizes, it may preferentially incorporate or exclude an intermediate daughter element from the ^{238}U or ^{235}U decay chain. For instance, monazite preferentially incorporates ^{230}Th in the ^{238}U decay chain (Schärer, 1984), while zircon excludes it (Mattinson, 1973), resulting in enrichment or depletion in ^{206}Pb , respectively. The magnitude of the disequilibrium correction is modeled using the ^{208}Pb content of a mineral to determine its Th/U ratio, then comparing to a user-input Th/U ratio of the magma. Another long-lived intermediate daughter isotope is ^{231}Pa , in the ^{235}U decay chain. Because there is no abundant long-lived Pa isotope, the initial $^{231}\text{Pa}/^{235}\text{U}$ activity ratio or the ratio of Pa and U distribution coefficients must be input by the user to make this correction, described in Appendix 2.8.

Although multiple analyses may share many of the above parameters, each will

have a unique set of measured Pb and U ratios. The measured ratios are the same as those needed for tracer characterization: the ratio of each naturally occurring isotope to a tracer isotope, and if multiple enriched isotopes are present, their ratio to one another (Table 2.1). The mass of tracer solution added to the analysis before measurement is also required to calculate the molar quantities of the sample and tracer isotopes.

2.2.2 Data Reduction

The algorithm that transforms the input parameters into isotopic dates can be broken down into three stages: Pb calculations, U calculations, and isotopic date determination. Each category entails calculation of multiple intermediate parameters, and the algorithm depends upon the tracer used and whether or not initial common Pb is present. Figure 2-1 illustrates the data reduction algorithm as a flow chart, with numbered ovals corresponding to the text section where each calculation appears.

Pb calculations

The Pb calculations are detailed in the top left panel of Figure 2-1 and the ovals contain section references to the text that follows.

Tracer

Isotope dilution uses a known quantity of a synthetic tracer isotope to determine the unknown amount of sample present. ^{205}Pb is ubiquitously used as the artificially enriched Pb isotope, and its abundance can be calculated from the measured mass of the tracer and its known concentration of ^{205}Pb .

$$\text{moles}(^{205}\text{Pb})_{tr} = \text{conc}(^{205}\text{Pb})_{tr} \cdot \text{mass}_{tr} \quad (2.1)$$

If a ^{202}Pb - ^{205}Pb tracer is used, the linear isotopic fractionation factor α_{Pb} is pro-

portional to the difference between the measured and true $^{202}\text{Pb}/^{205}\text{Pb}$ ratios.

$$\alpha_{\text{Pb}} = \frac{1}{3} \left[1 - \left(\frac{^{202}\text{Pb}}{^{205}\text{Pb}} \right)_{tr} / \left(\frac{^{202}\text{Pb}}{^{205}\text{Pb}} \right)_{meas} \right] \quad (2.2)$$

If a tracer containing only ^{205}Pb is used, then α_{Pb} must be determined from repeated measurements of an isotopic standard, such as NBS981 or NBS982, or from other analyses with the ^{202}Pb - ^{205}Pb tracer.

Because ^{204}Pb has no radiogenic component, the fractionation-corrected $^{204}\text{Pb}/^{205}\text{Pb}$ ratio can be used to determine the mass of common Pb (Pbc). Figure 2-2 illustrates the relationship between sample Pb components.

$$\left(\frac{^{204}\text{Pb}}{^{205}\text{Pb}} \right)_{fc} = \left(\frac{^{204}\text{Pb}}{^{205}\text{Pb}} \right)_{meas} \cdot (1 - \alpha_{\text{Pb}}) \quad (2.3)$$

Laboratory blank and initial common Pb

If initial common Pb is present, then the ^{204}Pb in the analysis must be apportioned between tracer, laboratory blank, and initial common Pb contributions. These relative contributions are illustrated in Figure 2-2a. When the isotopic composition of the initial common Pb has not been or cannot be measured directly, a popular alternative, albeit imperfect, is to use a Pb ore evolution model such as that of Stacey and Kramers (1975), which is reproduced in Appendix 2.8.

When initial common Pb is present, the total common Pb is apportioned by assuming the mass of the laboratory Pb blank, usually an average of several contemporaneous total procedural blank measurements. To calculate the moles of each isotope present from its mass and isotopic composition, it is helpful to first calculate the grams of laboratory Pb blank per mole of ^{204}Pb in the blank:

$$\begin{aligned} \left[\frac{\text{grams}(\text{Pb})}{\text{mole}(^{204}\text{Pb})} \right]_{bl} &= \frac{\text{grams}(^{204}\text{Pb})}{\text{mole}(^{204}\text{Pb})} + \left(\frac{^{206}\text{Pb}}{^{204}\text{Pb}} \right)_{bl} \cdot \frac{\text{grams}(^{206}\text{Pb})}{\text{mole}(^{206}\text{Pb})} \\ &+ \left(\frac{^{207}\text{Pb}}{^{204}\text{Pb}} \right)_{bl} \cdot \frac{\text{grams}(^{207}\text{Pb})}{\text{mole}(^{207}\text{Pb})} + \left(\frac{^{208}\text{Pb}}{^{204}\text{Pb}} \right)_{bl} \cdot \frac{\text{grams}(^{208}\text{Pb})}{\text{mole}(^{208}\text{Pb})} \quad (2.4) \end{aligned}$$

The moles of ^{204}Pb in the laboratory blank can now be determined from the blank mass input by the user,

$$\text{moles}(^{204}\text{Pb})_{bl} = \text{mass}(\text{Pb})_{bl} / \left[\frac{\text{grams}(\text{Pb})}{\text{mole}(^{204}\text{Pb})} \right]_{bl} \quad (2.5)$$

and the moles ^{206}Pb , ^{207}Pb , and ^{208}Pb in the laboratory blank are computed using (2.5) and the Pb blank IC.

$$\text{moles}(^{206}\text{Pb})_{bl} = \frac{\left(\frac{^{206}\text{Pb}}{^{204}\text{Pb}} \right)_{bl} \cdot \text{mass}(\text{Pb})_{bl}}{\left[\frac{\text{grams}(\text{Pb})}{\text{mole}(^{204}\text{Pb})} \right]_{bl}} \quad (2.6)$$

$$\text{moles}(^{207}\text{Pb})_{bl} = \frac{\left(\frac{^{207}\text{Pb}}{^{204}\text{Pb}} \right)_{bl} \cdot \text{mass}(\text{Pb})_{bl}}{\left[\frac{\text{grams}(\text{Pb})}{\text{mole}(^{204}\text{Pb})} \right]_{bl}} \quad (2.7)$$

$$\text{moles}(^{208}\text{Pb})_{bl} = \frac{\left(\frac{^{208}\text{Pb}}{^{204}\text{Pb}} \right)_{bl} \cdot \text{mass}(\text{Pb})_{bl}}{\left[\frac{\text{grams}(\text{Pb})}{\text{mole}(^{204}\text{Pb})} \right]_{bl}} \quad (2.8)$$

The total molar quantity of ^{204}Pb from common Pb, composed of both initial common Pb and laboratory blank, is the total moles of ^{204}Pb analyzed minus the contribution from the tracer.

$$\text{moles}(^{204}\text{Pb})_{tc} = \text{moles}(^{205}\text{Pb})_{tr} \cdot \left[\left(\frac{^{204}\text{Pb}}{^{205}\text{Pb}} \right)_{fc} - \left(\frac{^{204}\text{Pb}}{^{205}\text{Pb}} \right)_{tr} \right] \quad (2.9)$$

Because the total common Pb is composed of laboratory blank Pb and initial Pbc, the additional ^{204}Pbc in excess of the laboratory blank is assumed to be initial Pbc.

$$\text{moles}(^{204}\text{Pb})_{com} = \text{moles}(^{204}\text{Pb})_{tc} - \text{moles}(^{204}\text{Pb})_{bl} \quad (2.10)$$

The initial Pbc contributions to other Pb isotopes can be calculated from the initial ^{204}Pbc using the initial common Pb IC determined by the user or from a

model, such as equations (2.100) to (2.105).

$$moles(^{206}\text{Pb})_{com} = \left(\frac{^{206}\text{Pb}}{^{204}\text{Pb}} \right)_{com} \cdot moles(^{204}\text{Pb})_{com} \quad (2.11)$$

$$moles(^{207}\text{Pb})_{com} = \left(\frac{^{207}\text{Pb}}{^{204}\text{Pb}} \right)_{com} \cdot moles(^{204}\text{Pb})_{com} \quad (2.12)$$

$$moles(^{208}\text{Pb})_{com} = \left(\frac{^{208}\text{Pb}}{^{204}\text{Pb}} \right)_{com} \cdot moles(^{204}\text{Pb})_{com} \quad (2.13)$$

Laboratory blank, no initial common Pb

When the dated phase incorporates no initial common Pb, the moles of ^{204}Pb in the laboratory blank can be expressed as the total moles of ^{204}Pb in the analysis minus any contribution from the tracer (Figure 2-2b). The moles of ^{204}Pb in the laboratory blank, along with its average isotopic composition, are then used to calculate the moles of ^{206}Pb , ^{207}Pb , and ^{208}Pb in the laboratory blank.

$$moles(^{204}\text{Pb})_{bl} = moles(^{205}\text{Pb})_{tr} \cdot \left[\left(\frac{^{204}\text{Pb}}{^{205}\text{Pb}} \right)_{fc} - \left(\frac{^{204}\text{Pb}}{^{205}\text{Pb}} \right)_{tr} \right] \quad (2.14)$$

$$moles(^{206}\text{Pb})_{bl} = moles(^{205}\text{Pb})_{tr} \cdot \left(\frac{^{206}\text{Pb}}{^{204}\text{Pb}} \right)_{bl} \cdot \left[\left(\frac{^{204}\text{Pb}}{^{205}\text{Pb}} \right)_{fc} - \left(\frac{^{204}\text{Pb}}{^{205}\text{Pb}} \right)_{tr} \right] \quad (2.15)$$

$$moles(^{207}\text{Pb})_{bl} = moles(^{205}\text{Pb})_{tr} \cdot \left(\frac{^{207}\text{Pb}}{^{204}\text{Pb}} \right)_{bl} \cdot \left[\left(\frac{^{204}\text{Pb}}{^{205}\text{Pb}} \right)_{fc} - \left(\frac{^{204}\text{Pb}}{^{205}\text{Pb}} \right)_{tr} \right] \quad (2.16)$$

$$moles(^{208}\text{Pb})_{bl} = moles(^{205}\text{Pb})_{tr} \cdot \left(\frac{^{208}\text{Pb}}{^{204}\text{Pb}} \right)_{bl} \cdot \left[\left(\frac{^{204}\text{Pb}}{^{205}\text{Pb}} \right)_{fc} - \left(\frac{^{204}\text{Pb}}{^{205}\text{Pb}} \right)_{tr} \right] \quad (2.17)$$

The total mass of laboratory blank Pb, frequently reported in data tables, should be calculated from the moles of Pb isotopes in the blank and their gram-atomic masses.

Radiogenic and sample Pb

The tracer IC, along with the moles of laboratory blank and initial Pbc, provide enough information to determine the radiogenic components of ^{206}Pb , ^{207}Pb , and ^{208}Pb in the analysis. First, the measured ratios of Pb isotopes relative to ^{205}Pb in the tracer are fractionation corrected, and the tracer contribution is subtracted.

Multiplying this by the moles of ^{205}Pb in the tracer gives the molar quantity of each Pb isotope in the sample, from which the Pb blank and initial Pbc components are subtracted.

$$\begin{aligned} \text{moles}(^{206}\text{Pb})_{rad} &= \text{moles}(^{205}\text{Pb})_{tr} \cdot \left[\left(\frac{^{206}\text{Pb}}{^{205}\text{Pb}} \right)_{meas} \cdot (1 + \alpha_{\text{Pb}}) - \left(\frac{^{206}\text{Pb}}{^{205}\text{Pb}} \right)_{tr} \right] \\ &\quad - \text{moles}(^{206}\text{Pb})_{bl} - \text{moles}(^{206}\text{Pb})_{com} \end{aligned} \quad (2.18)$$

$$\begin{aligned} \text{moles}(^{207}\text{Pb})_{rad} &= \text{moles}(^{205}\text{Pb})_{tr} \cdot \left[\left(\frac{^{207}\text{Pb}}{^{205}\text{Pb}} \right)_{meas} \cdot (1 + 2\alpha_{\text{Pb}}) - \left(\frac{^{207}\text{Pb}}{^{205}\text{Pb}} \right)_{tr} \right] \\ &\quad - \text{moles}(^{207}\text{Pb})_{bl} - \text{moles}(^{207}\text{Pb})_{com} \end{aligned} \quad (2.19)$$

$$\begin{aligned} \text{moles}(^{208}\text{Pb})_{rad} &= \text{moles}(^{205}\text{Pb})_{tr} \cdot \left[\left(\frac{^{208}\text{Pb}}{^{205}\text{Pb}} \right)_{meas} \cdot (1 + 3\alpha_{\text{Pb}}) - \left(\frac{^{208}\text{Pb}}{^{205}\text{Pb}} \right)_{tr} \right] \\ &\quad - \text{moles}(^{208}\text{Pb})_{bl} - \text{moles}(^{208}\text{Pb})_{com} \end{aligned} \quad (2.20)$$

If an isochron technique is employed, the initial Pbc isotopic composition for a group of fractions is calculated or constrained at the same time as their date. Only the common Pb from the laboratory blank and tracer should be subtracted in this case, leaving the mass of each isotope of Pb from the sample.

$$\begin{aligned} \text{moles}(^{206}\text{Pb})_{spl} &= \text{moles}(^{205}\text{Pb})_{tr} \cdot \left[\left(\frac{^{206}\text{Pb}}{^{205}\text{Pb}} \right)_{meas} \cdot (1 + \alpha_{\text{Pb}}) - \left(\frac{^{206}\text{Pb}}{^{205}\text{Pb}} \right)_{tr} \right] \\ &\quad - \text{moles}(^{206}\text{Pb})_{bl} \end{aligned} \quad (2.21)$$

$$\begin{aligned} \text{moles}(^{207}\text{Pb})_{spl} &= \text{moles}(^{205}\text{Pb})_{tr} \cdot \left[\left(\frac{^{207}\text{Pb}}{^{205}\text{Pb}} \right)_{meas} \cdot (1 + 2\alpha_{\text{Pb}}) - \left(\frac{^{207}\text{Pb}}{^{205}\text{Pb}} \right)_{tr} \right] \\ &\quad - \text{moles}(^{207}\text{Pb})_{bl} \end{aligned} \quad (2.22)$$

$$\begin{aligned} \text{moles}(^{208}\text{Pb})_{spl} &= \text{moles}(^{205}\text{Pb})_{tr} \cdot \left[\left(\frac{^{208}\text{Pb}}{^{205}\text{Pb}} \right)_{meas} \cdot (1 + 3\alpha_{\text{Pb}}) - \left(\frac{^{208}\text{Pb}}{^{205}\text{Pb}} \right)_{tr} \right] \\ &\quad - \text{moles}(^{208}\text{Pb})_{bl} \end{aligned} \quad (2.23)$$

U calculations

The U calculations are detailed in the bottom left panel of Figure 2-1 and the ovals contain section references to the text that follows.

Oxide correction

Uranium is commonly measured by TIMS in two forms, as a metal (U^+) species, or as an oxide (UO_2^+). Although the oxide species ionizes more efficiently, it introduces possible isobaric interferences. About 99.8% of oxygen is ^{16}O and 0.2% is ^{18}O . Using a mixed ^{233}U - ^{235}U tracer, the ^{18}O creates a significant isobaric interference: $^{233}\text{U}^{18}\text{O}^{16}\text{O}$ (mass = 267) on $^{235}\text{U}^{16}\text{O}^{16}\text{O}$ (mass = 267). Because both $\text{U}^{18}\text{O}^{16}\text{O}$ and $\text{U}^{16}\text{O}^{18}\text{O}$ permutations are possible, the $^{233}\text{UO}_2$ with one ^{18}O will be approximately (0.2% ^{18}O abundance) \times (2 UO_2 permutations) = 0.4% as abundant as $^{233}\text{U}^{16}\text{O}^{16}\text{O}$. The precise correction depends on the $^{18}\text{O}/^{16}\text{O}$ in the UO_2^+ species, which can be measured during the analysis on high-intensity ion beams, or inferred for smaller samples from the mean value of the larger runs.

Because the isobaric interference is underneath the ^{235}U peak, both the measured $^{238}\text{U}/^{235}\text{U}$ oxide (mass 270/267) and $^{233}\text{U}/^{235}\text{U}$ oxide (mass 265/267) ratios must be corrected.

$$\left(\frac{^{233}\text{U}}{^{235}\text{U}}\right)_{oc} = \frac{\left(\frac{^{265}\text{UO}_2}{^{267}\text{UO}_2}\right)_{meas}}{1 - 2 \left(\frac{^{18}\text{O}}{^{16}\text{O}}\right)_{Uox} \cdot \left(\frac{^{265}\text{UO}_2}{^{267}\text{UO}_2}\right)_{meas}} \quad (2.24)$$

$$\left(\frac{^{238}\text{U}}{^{235}\text{U}}\right)_{oc} = \frac{\left(\frac{^{270}\text{UO}_2}{^{267}\text{UO}_2}\right)_{meas}}{1 - 2 \left(\frac{^{18}\text{O}}{^{16}\text{O}}\right)_{Uox} \cdot \left(\frac{^{265}\text{UO}_2}{^{267}\text{UO}_2}\right)_{meas}} \quad (2.25)$$

U blank and tracer masses

Regardless of the tracer used, the mass of both the U blank and tracer contributions are calculated from their input masses and isotopic compositions.

$$moles(^{235}\text{U})_{bl} = \frac{mass(\text{U})_{bl}}{\frac{grams(^{235}\text{U})}{mole(^{235}\text{U})} + \left(\frac{^{238}\text{U}}{^{235}\text{U}}\right)_{bl} \cdot \frac{grams(^{238}\text{U})}{mole(^{238}\text{U})}} \quad (2.26)$$

$$moles(^{238}\text{U})_{bl} = \left(\frac{^{238}\text{U}}{^{235}\text{U}}\right)_{bl} \cdot moles(^{235}\text{U})_{bl} \quad (2.27)$$

$$moles(^{235}\text{U})_{tr} = conc(^{235}\text{U})_{tr} \cdot mass_{tr} \quad (2.28)$$

$$moles(^{238}\text{U})_{tr} = \left(\frac{^{238}\text{U}}{^{235}\text{U}} \right)_{tr} \cdot moles(^{235}\text{U})_{tr} \quad (2.29)$$

If the tracer contains the synthetic isotope ^{233}U , then its molar quantity must also be calculated before determining the radiogenic components of the sample.

$$moles(^{233}\text{U})_{tr} = \left(\frac{^{233}\text{U}}{^{235}\text{U}} \right)_{tr} \cdot moles(^{235}\text{U})_{tr} \quad (2.30)$$

Simultaneous fractionation correction and isotope dilution:

A: Fractionation correction and isotope dilution for a mixed ^{233}U - ^{235}U tracer

Using a mixed ^{233}U - ^{235}U tracer, such as the EARTHTIME-distributed ‘ET535 tracer’, requires simultaneous fractionation correction and isotope dilution, and blank and tracer subtraction calculations. This yields an expression for both the amount of parent U present and the linear fractionation factor α_U .

To begin, the contributions to the three measured U isotopes are (Figure 2-2)

$$moles(^{233}\text{U})_{tot} = moles(^{233}\text{U})_{tr} \quad (2.31)$$

$$moles(^{235}\text{U})_{tot} = moles(^{235}\text{U})_{tr} + moles(^{235}\text{U})_{bl} + moles(^{235}\text{U})_{spl} \quad (2.32)$$

$$moles(^{238}\text{U})_{tot} = moles(^{238}\text{U})_{tr} + moles(^{238}\text{U})_{bl} + moles(^{238}\text{U})_{spl} \quad (2.33)$$

After fractionation correction, the oxide-corrected ratios in (2.24) and (2.25) or the $^{233}\text{U}/^{235}\text{U}$ and $^{238}\text{U}/^{235}\text{U}$ ratios measured as a metal represent the molar ratios of the quantities in equations (2.31) and (2.33) to those in (2.32).

$$\left(\frac{^{233}\text{U}}{^{235}\text{U}} \right)_{oc} \cdot (1 - 2\alpha_U) = \frac{moles(^{233}\text{U})_{tr}}{moles(^{235}\text{U})_{tr} + moles(^{235}\text{U})_{bl} + moles(^{235}\text{U})_{spl}} \quad (2.34)$$

$$\left(\frac{^{238}\text{U}}{^{235}\text{U}} \right)_{oc} \cdot (1 + 3\alpha_U) = \frac{moles(^{238}\text{U})_{tr} + moles(^{238}\text{U})_{bl} + moles(^{238}\text{U})_{spl}}{moles(^{235}\text{U})_{tr} + moles(^{235}\text{U})_{bl} + moles(^{235}\text{U})_{spl}} \quad (2.35)$$

The two equations (2.34) and (2.35) have three unknowns, α_U and the moles of ^{235}U and ^{238}U . The rest of the terms are defined in equations (2.26) to (2.30). To

eliminate a variable, the moles of ^{238}U can be expressed as the moles of ^{235}U multiplied by the $^{238}\text{U}/^{235}\text{U}$ of the sample. Making this substitution and solving the system of equations for the moles of ^{235}U in the sample and α_{U} yields

$$\begin{aligned} \text{moles}(^{235}\text{U})_{spl} = & \left[3 \left(\frac{^{238}\text{U}}{^{235}\text{U}} \right)_{oc} / \left(\frac{^{233}\text{U}}{^{235}\text{U}} \right)_{oc} \cdot \text{moles}(^{233}\text{U})_{tr} \right. \\ & - 5 \left(\frac{^{238}\text{U}}{^{235}\text{U}} \right)_{oc} \cdot \left(\text{moles}(^{235}\text{U})_{bl} + \text{moles}(^{235}\text{U})_{tr} \right) \\ & \left. + 2 \left(\text{moles}(^{238}\text{U})_{bl} + \text{moles}(^{238}\text{U})_{tr} \right) \right] \\ & / \left[5 \left(\frac{^{238}\text{U}}{^{235}\text{U}} \right)_{oc} - 2 \left(\frac{^{238}\text{U}}{^{235}\text{U}} \right)_{spl} \right] \end{aligned} \quad (2.36)$$

The moles of ^{238}U in the sample can now be determined using the $^{238}\text{U}/^{235}\text{U}$ ratio of the sample.

$$\text{moles}(^{238}\text{U})_{spl} = \text{moles}(^{235}\text{U})_{spl} \cdot \left(\frac{^{238}\text{U}}{^{235}\text{U}} \right)_{spl} \quad (2.37)$$

Although the solution to the system of equations in (2.34) and (2.35) yields an expression for α_{U} , a simpler expression is obtained by substituting the moles of ^{235}U in the sample derived in (2.36) into equation (2.34), then solving for α_{U} .

$$\alpha_{\text{U}} = \frac{1}{2} - \text{moles}(^{233}\text{U})_{tr} / \left[2 \left(\frac{^{233}\text{U}}{^{235}\text{U}} \right)_{oc} \cdot \left(\text{moles}(^{235}\text{U})_{spl} + \text{moles}(^{235}\text{U})_{tr} + \text{moles}(^{235}\text{U})_{bl} \right) \right] \quad (2.38)$$

B: Fractionation correction and isotope dilution for a single ^{235}U tracer

As with Pb, fractionation for a single-isotope tracer must be determined by repeated analyses of a standard. For U isotope measurements by TIMS, a single ^{235}U tracer is most common, with isotopic fractionation determined by repeated analysis of CRM U500. Only the $^{238}\text{U}/^{235}\text{U}$ ratio is measured, no oxide correction is needed, and the components of ^{238}U and ^{235}U are given by equation (2.35). Representing the the sample ^{238}U as the moles of ^{235}U multiplied by the $^{238}\text{U}/^{235}\text{U}$ of the sample, the resulting equation may be solved for the moles of ^{235}U .

$$\begin{aligned}
\text{moles}({}^{235}\text{U})_{spl} = & \hspace{20em} (2.39) \\
& \frac{\text{moles}({}^{238}\text{U})_{bl} + \text{moles}({}^{238}\text{U})_{tr} - \left(\frac{{}^{238}\text{U}}{{}^{235}\text{U}}\right)_{meas} (1 + 3\alpha_U) (\text{moles}({}^{235}\text{U})_{bl} + \text{moles}({}^{235}\text{U})_{tr})}{\left(\frac{{}^{238}\text{U}}{{}^{235}\text{U}}\right)_{meas} (1 + 3\alpha_U) - \left(\frac{{}^{238}\text{U}}{{}^{235}\text{U}}\right)_{spl}}
\end{aligned}$$

The moles of ${}^{238}\text{U}$ is calculated with equation (2.37).

C: Fractionation correction and isotope dilution for a mixed ${}^{233}\text{U}$ - ${}^{236}\text{U}$ tracer

Using a mixed ${}^{233}\text{U}$ - ${}^{236}\text{U}$ tracer, the magnitude of isotopic fractionation α_U can be determined for each ratio measured, or on the mean of the measured ratios.

$$\alpha_U = \frac{1}{3} \left[1 - \left(\frac{{}^{233}\text{U}}{{}^{236}\text{U}}\right)_{tr} / \left(\frac{{}^{233}\text{U}}{{}^{236}\text{U}}\right)_{meas} \right] \quad (2.40)$$

The moles of ${}^{236}\text{U}$ in the tracer is equal to the concentration of ${}^{236}\text{U}$ in the tracer multiplied by the measured tracer mass,

$$\text{moles}({}^{236}\text{U})_{tr} = \text{conc}({}^{236}\text{U})_{tr} \cdot \text{mass}_{tr} \quad (2.41)$$

If the U is analyzed as an oxide species, then the measured ${}^{238}\text{U}/{}^{236}\text{U}$ requires oxide correction for the isobaric interference of ${}^{236}\text{U}^{18}\text{O}^{16}\text{O}$ (mass 270) on ${}^{238}\text{U}^{16}\text{O}^{16}\text{O}$ (mass 270), analogous to the case presented in Section 2.2.2 for a ${}^{233}\text{U}$ - ${}^{235}\text{U}$ tracer. Neglecting the insignificant isobaric interference of ${}^{235}\text{U}^{17}\text{O}^{16}\text{O}$ on ${}^{236}\text{U}^{16}\text{O}^{16}\text{O}$ because the tracer and sample ${}^{235}\text{U}$ and the ${}^{17}\text{O}$ abundances are all relatively small, the oxide-corrected uranium ratios become

$$\left(\frac{{}^{233}\text{U}}{{}^{236}\text{U}}\right)_{oc} = \left(\frac{{}^{265}\text{UO}_2}{{}^{268}\text{UO}_2}\right)_{meas} \quad (2.42)$$

$$\left(\frac{^{238}\text{U}}{^{236}\text{U}}\right)_{oc} = \left(\frac{^{270}\text{UO}_2}{^{268}\text{UO}_2}\right)_{meas} - 2 \left(\frac{^{18}\text{O}}{^{16}\text{O}}\right) \quad (2.43)$$

where the result of equation (2.42) can be used to calculate the magnitude of isotopic fractionation in equation (2.40).

Using the $^{238}\text{U}/^{236}\text{U}$ measured as a metal or oxide-corrected in equation (2.43) and solving for the moles of ^{238}U in the sample yields

$$\text{moles}(^{238}\text{U})_{spl} = \text{moles}(^{236}\text{U})_{tr} \cdot \left[\left(\frac{^{238}\text{U}}{^{236}\text{U}}\right)_{meas} (1 + 2\alpha_U) - \left(\frac{^{238}\text{U}}{^{236}\text{U}}\right)_{tr} \right] - \text{moles}(^{238}\text{U})_{bl} \quad (2.44)$$

where the moles of ^{238}U in the blank is calculated with equation (2.27).

The moles of ^{235}U in the sample is then determined using the $^{238}\text{U}/^{235}\text{U}$ of the sample,

$$\text{moles}(^{235}\text{U})_{spl} = \text{moles}(^{238}\text{U})_{spl} / \left(\frac{^{238}\text{U}}{^{235}\text{U}}\right)_{spl} \quad (2.45)$$

Calculation of Isotopic Ratios

Radiogenic isotope ratios, whose components have been corrected for fractionation and interferences as well as blank and tracer contributions, are used to calculate radiogenic isotope dates. They are also used for plotting conventional (Wetherill) and Tera-Wasserburg-type concordia diagrams.

$$\left(\frac{^{207}\text{Pb}}{^{206}\text{Pb}}\right)_{rad} = \frac{\text{moles}(^{207}\text{Pb})_{rad}}{\text{moles}(^{206}\text{Pb})_{rad}} \quad (2.46)$$

$$\left(\frac{^{206}\text{Pb}}{^{238}\text{U}}\right)_{rad} = \frac{\text{moles}(^{206}\text{Pb})_{rad}}{\text{moles}(^{238}\text{U})_{spl}} \quad (2.47)$$

$$\left(\frac{^{207}\text{Pb}}{^{235}\text{U}}\right)_{rad} = \frac{\text{moles}(^{207}\text{Pb})_{rad}}{\text{moles}(^{235}\text{U})_{spl}} \quad (2.48)$$

Isotopic Dates

A radiogenic isotope date for either the ^{238}U or ^{235}U system can be derived by solving the isotopic decay equation, $D/P = e^{\lambda t} - 1$ for t , the time elapsed, where D/P is the present radiogenic daughter to parent ratio.

$$t_{206/238} = \frac{1}{\lambda_{238}} \log \left[\left(\frac{^{206}\text{Pb}}{^{238}\text{U}} \right)_{rad} + 1 \right] \quad (2.49)$$

$$t_{207/235} = \frac{1}{\lambda_{235}} \log \left[\left(\frac{^{207}\text{Pb}}{^{235}\text{U}} \right)_{rad} + 1 \right] \quad (2.50)$$

To calculate a $^{207}\text{Pb}/^{206}\text{Pb}$ date, it is not possible to solve

$$\left(\frac{^{207}\text{Pb}}{^{206}\text{Pb}} \right)_{rad} = \left(\frac{^{238}\text{U}}{^{235}\text{U}} \right)_{spl}^{-1} \cdot \frac{\exp(\lambda_{235} \cdot t_{207/206}) - 1}{\exp(\lambda_{238} \cdot t_{207/206}) - 1} \quad (2.51)$$

directly for t . Instead, Newton's Method, an iterative numerical solution, is used by *U-Pb_Redux*.

Equations to correct the isotopic dates for initial daughter isotope disequilibrium are derived in Appendix 2.8.

Isochron Ratios and Dates

Alternatively, an isochron approach uses sample isotope ratios that incorporate an initial Pbc component (equations 2.21 to 2.23) to determine both the isotopic date and the common Pb IC. Both two-axis plots, common in meteorite and carbonate U-Pb studies (e.g., Patterson, 1956; Moorbath et al., 1987), and three axis plots (Ludwig, 1998a) that make optimum use of both U decay schemes are used.

Isotopic ratios popularly used in isochron calculations include $^{207}\text{Pb}/^{206}\text{Pb}$, $^{204}\text{Pb}/^{206}\text{Pb}$, $^{238}\text{U}/^{206}\text{Pb}$, $^{204}\text{Pb}/^{207}\text{Pb}$, $^{238}\text{U}/^{207}\text{Pb}$, $^{235}\text{U}/^{207}\text{Pb}$, $^{238}\text{U}/^{204}\text{Pb}$, and $^{235}\text{U}/^{204}\text{Pb}$, which may be calculated using the equations for sample molar quantities above.

2.3 Uncertainty Propagation Principles

In the terminology of metrology, uncertainty and error have different meanings. The uncertainty of a measured parameter refers to the dispersion of the values that could reasonably be attributed to it (BIPM et al., 2008b), while an error is the difference between the true (but unknown) value and the measured value.

Uncertainty propagation transforms a set of several inputs, with their associated uncertainties, into the uncertainties in one or more outputs. This transformation depends upon the values and uncertainties of the inputs as well as the sensitivity of the output(s) to them. There are several algorithms that can perform this transformation, but the most popular are linear uncertainty propagation and the Monte Carlo method (MCM).

Linear uncertainty propagation approximates functions in the neighborhood of their observed value by their derivative, and uses the observed values and uncertainties, assumed to be normally distributed, to find the maximum likelihood estimate of the output value. Instead of making these assumptions, the MCM uses many simulations of the uncertain value of each input to propagate their probability distribution through the data reduction equations, directly determining the expected distribution of the output. Although the MCM makes fewer assumptions, it requires 10^5 to 10^6 iterations and can thus be slow to implement for large datasets (BIPM et al., 2008a). For precisely measured data, the linear approximation returns the same quality result in significantly less time, as demonstrated in Section 2.6. *U-Pb_Redux* uses this approach in order to reduce large datasets and drive interactive visualizations.

2.3.1 Determining the Uncertainties of Inputs

Uncertainties in ID-TIMS measurements ultimately derive from either mass determinations with a balance (e.g., the mass of the tracer or the masses of the isotopic reference materials used to make gravimetrically calibrated solutions) or from isotope ratio determinations made with a TIMS. For routine ID-TIMS analyses, mass determinations contribute only negligibly to the analytical uncertainty budget, and

isotope ratio determinations contribute most. There are three common techniques for measuring isotope ratios with TIMS: with a static array of Faraday collectors, by a single ion counting detector such as a Daly or SEM (secondary electron multiplier), or with a combination of the two, and measurement uncertainty derives from different sources with each technique.

A fixed array of Faraday collectors at unit mass spacing can be used to measure very large ($>\sim 100\text{pg}$) Pb^* samples and average-size ($>\sim 1\text{ng}$) U samples as either metal (U^+) or oxide (UO_2^+) species. Static measurements using Faraday detectors have the advantage of measuring all isotopes simultaneously. However, the amplifier circuits containing large (10^{11} or 10^{12} Ω) resistors that are used to measure the ion beam supply some small but constant Johnson-Nyquist (thermal) noise to each signal, in addition to the ‘shot’ noise proportional to the ion beam intensity. Each of these uncertainty contributions manifests itself in the baseline-corrected isotopic ratio measurements. For sufficiently large, stable signals, successive static Faraday isotope ratio measurements should approximate multivariate normal distributions, and their mean and uncertainty can be directly input into uncertainty propagation algorithms.

The ion counter, by converting a single ion beam at a time into an electron multiplier or photomultiplier signal, is not subject to the Johnson-Nyquist noise of large resistors. However, because it is used to measure smaller ($<\sim 0.2$ pA) ion beams, the signal to noise ratio is generally lower due to shot noise. Several effects specific to ion counters also contribute to the isotope ratio uncertainty, including dark noise (essentially Johnson-Nyquist noise in the electron/photomultiplier circuit) and dead time, or the inability to resolve closely spaced ion arrivals. While the dark noise can be averaged out with a sufficiently long baseline determination, the dead time must be measured and monitored closely to ensure the accuracy of ratios significantly greater or less than one (e.g. $^{206}\text{Pb}/^{204}\text{Pb}$ for a radiogenic sample). Single collector measurements are subject to further uncertainty from interpolation between successive ion beam measurements as the ion beam grows and decays with time (e.g., Ludwig, 2009).

In order to measure small (<0.2 pA or $\sim 10^6$ cps) ^{204}Pb signals on an ion

counter concurrent with static measurements of ^{205}Pb to ^{208}Pb on Faraday detectors, a ‘FaraDaly’ routine is employed. The routine consists of two cycles, the first with ^{204}Pb in the ion counter and ^{205}Pb through ^{208}Pb beams in the high mass Faraday detectors, alternating with a second cycle with ^{205}Pb in the ion counter and ^{206}Pb to ^{208}Pb beams in the Faraday detectors. The relative Faraday/ion counter gain for each cycle can be derived from the $^{206}\text{Pb}/^{205}\text{Pb}$ ratio measured on the Faradays in the first cycle vs. the $^{206}\text{Pb}/^{205}\text{Pb}$ ratio measured in the second cycle, with the ^{205}Pb beam on the ion counter; ratios involving ^{204}Pb from the first cycle can then be corrected for this relative gain. Because the number of measured isotope ratios to ^{204}Pb is half that of the other isotopes, conventional covariance estimation techniques (see Section 2.3.3) are invalid, and an expectation-maximization algorithm must be employed (Dempster et al., 1977).

2.3.2 Uncertainty Propagation Equation

The linear uncertainty propagation equation can be derived from the Taylor series expansion of a function $f(x)$ around the point $x = \bar{x}$,

$$f(\bar{x} + \Delta x) = f(\bar{x}) + \Delta x f'(\bar{x}) + \Delta x^2 \frac{f''(\bar{x})}{2!} + \dots \quad (2.52)$$

the deviation of the function from its value at $x = \bar{x}$ is expressed as the sum of the terms after $f(\bar{x})$, beginning with the first-order term $\Delta x f'(\bar{x})$. For a deviation of $\Delta x = \sigma_x$ near $x = \bar{x}$, a first-order approximation of the average deviation of $y = f(x)$ is

$$\sigma_y \approx \sigma_x \frac{dy}{dx}, \quad (2.53)$$

where $\frac{dy}{dx}$ is evaluated at $x = \bar{x}$. Squaring both sides yields the conventional linear uncertainty propagation equation for a function of a single variable, illustrated geometrically in Figure 2-3:

$$\sigma_y^2 \approx \sigma_x^2 \left(\frac{dy}{dx} \right)^2. \quad (2.54)$$

The expected value of Δx^2 , or $(x_i - \bar{x})^2$ for a series of measurements x_i about

the mean \bar{x} is the variance of x , denoted σ_x^2 . Likewise, σ_y^2 is the resulting square of the average deviation in $y = f(x)$ due to the scatter in the measurements x_i . The derivative is evaluated at $x = \bar{x}$. In dropping the higher-order terms from the Taylor series, beginning with the Δx^2 term, this approach assumes that the uncertainty in x is relatively small compared to the curvature of $f(x)$, or that the function is locally linear at the scale of σ_x (see Figure 2-3).

Linear uncertainty propagation for multiple inputs requires the multivariate form of the Taylor series, here expressed for two variables $z = f(x, y)$,

$$\begin{aligned} f(\bar{x} + \Delta x, \bar{y} + \Delta y) &= f(\bar{x}, \bar{y}) \\ &+ [\Delta x f_x(\bar{x}, \bar{y}) + \Delta y f_y(\bar{x}, \bar{y})] \\ &+ \frac{1}{2!} [\Delta x^2 f_{xx}(\bar{x}, \bar{y}) + 2\Delta x \Delta y f_{xy}(\bar{x}, \bar{y}) + \Delta y^2 f_{yy}(\bar{x}, \bar{y})] \dots \end{aligned} \quad (2.55)$$

where f_x and f_{xx} are the first and second derivatives of $f(x, y)$ with respect to x , respectively. The higher-order terms may again be dropped, assuming that uncertainties are small and the differentiated functions are locally linear at the scale the uncertainties of their inputs. The linear term in equation (2.56) again represents the deviation from the measured value $z = f(x, y)$ encountered at a distance $(\Delta x, \Delta y)$ from (\bar{x}, \bar{y}) . Squaring the second term on the right hand side of equation (2.56) yields

$$\begin{aligned} \Delta z^2 &\approx \Delta x^2 f_x(\bar{x}, \bar{y})^2 + 2\Delta x \Delta y f_x(\bar{x}, \bar{y}) f_y(\bar{x}, \bar{y}) \\ &+ \Delta y^2 f_y(\bar{x}, \bar{y})^2. \end{aligned} \quad (2.56)$$

Thus the expression for the variance of a function of two variables introduces a new term, the expected value of $\Delta x \Delta y$, or $(x_i - \bar{x})(y_i - \bar{y})$, which is known as the covariance between x and y and denoted σ_{xy}^2 . Writing out the derivatives in equation (2.57), which are evaluated at $(x, y) = (\bar{x}, \bar{y})$, and making the above substitutions yields the conventional linear uncertainty propagation equation:

$$\sigma_z^2 = \sigma_x^2 \left(\frac{dz}{dx} \right)^2 + 2\sigma_{xy}^2 \left(\frac{dz}{dx} \right) \left(\frac{dz}{dy} \right) + \sigma_y^2 \left(\frac{dz}{dy} \right)^2. \quad (2.57)$$

2.3.3 Covariance and Correlation

When two uncertainties are correlated, both are dependent on a common parameter or effect. One example of correlated uncertainties is between two measured isotope ratios with the same isotope in the denominator, such as the measured $^{206}\text{Pb}/^{204}\text{Pb}$ and $^{207}\text{Pb}/^{204}\text{Pb}$ of a radiogenic sample or between the $^{206}\text{Pb}/^{205}\text{Pb}$ and $^{207}\text{Pb}/^{205}\text{Pb}$ of an under-spiked sample. In the first case, the uncertainty in the measurement of the less abundant ^{204}Pb denominator isotope is large, and the uncertainties of the two ratios will be highly correlated because most of the uncertainty in each isotope ratio derives from a common source, the ^{204}Pb measurement. If the uncertainty in the denominator isotope is relatively small compared to those in the numerators, such as the second case above, then their uncertainties are less correlated, since most of the uncertainty in each ratio is contributed by the independent measurements of the numerator isotopes, the less abundant ^{206}Pb and ^{207}Pb .

In both cases above, the correlation between a pair of measured isotope ratios can be determined empirically from the discrete measured data. The covariance is defined as the expected value of $\Delta x \Delta y$, or $(x_i - \bar{x})(y_i - \bar{y})$ above. An unbiased estimate of the covariance, σ_{xy}^2 can be calculated from a discrete sample of n independent measurements of x and y as

$$\sigma_{xy}^2 = \frac{1}{n-1} \sum_{i=1}^n (x_i - \bar{x})(y_i - \bar{y}) \quad (2.58)$$

The correlation coefficient ρ_{xy} is commonly cited because it does not depend on the magnitude of the uncertainty of x or y . It has a range of $[-1, 1]$ inclusive and can be calculated from the covariance term above, $\rho_{xy} = \sigma_{xy}^2 / (\sigma_x \sigma_y)$.

If discrete input data are not available, the covariance between two measured isotope ratios can be estimated using the uncertainty of a third isotope ratio that is the quotient of the first two (Schmitz and Schoene, 2007). For instance, the covariance between the measured $^{206}\text{Pb}/^{204}\text{Pb}$ and $^{207}\text{Pb}/^{204}\text{Pb}$ ratios could be estimated using their uncertainties and the uncertainty in the $^{206}\text{Pb}/^{207}\text{Pb}$ ratios from the same dataset. This approach assumes that the mean and standard error of all three ratios

are calculated from the same n measurements, i.e. that no data have been discarded one ratio and not another.

Other examples of variables with correlated uncertainties include isotope ratios or dates that have been subjected to a common correction, such as fractionation correction or blank and tracer subtraction. For instance, if x and y above are functions of a set of common variables a, b, \dots , then

$$\sigma_{xy}^2 = \sigma_a^2 \left(\frac{dx}{da} \right) \left(\frac{dy}{da} \right) + \sigma_b^2 \left(\frac{dx}{db} \right) \left(\frac{dy}{db} \right) + \sigma_{ab}^2 \left[\left(\frac{dx}{da} \right) \left(\frac{dy}{db} \right) + \left(\frac{dx}{db} \right) \left(\frac{dy}{da} \right) \right] + \dots \quad (2.59)$$

Here, a, b, \dots could for instance be the tracer IC and enriched isotope concentrations, whose uncertainties and covariance structure, $\sigma_a^2, \sigma_b^2, \sigma_{ab}^2, \dots$ are input by the user, and the calculated variables x and y could be the radiogenic $^{206}\text{Pb}/^{238}\text{U}$ and $^{207}\text{Pb}/^{235}\text{U}$ ratios. Because the variables x and y are interchangeable in equation (2.59), the covariance of x with y is the same as the covariance of y with x : $\sigma_{xy}^2 = \sigma_{yx}^2$.

Equations (2.57) and (2.59) can be expanded for any number of variables and corresponding uncertainties. However, for each new variable added to equation (2.57), a new variance term must be added, as well as covariance terms for each new pair of variables created. The number of covariance terms grows as n^2 , so that if 35 inputs and uncertainties required to reduce U-Pb data, up to 630 terms are required to completely describe their uncertainty. Furthermore, determining the total derivatives of the each output with respect to the each input through the complex series of equations presented in Section 2.2 is a daunting task by hand, but it is required for detailed linear analysis. The covariance terms and derivatives are most easily combined for uncertainty propagation by organizing them into covariance and Jacobian matrices, respectively, and employing linear algebraic techniques.

2.4 Propagating Uncertainty with Matrices

A linear algebraic framework is advantageous for uncertainty propagation because it efficiently organizes the covariance and derivative terms presented above into matri-

ces. Matrix multiplication is computationally fast, which enables rapid updates as the analyst explores parameter space in the graphical user interface of *U-Pb_Redux*. Derivatives of the intermediate reduction parameters and outputs calculated in equations (2.2) to (2.51) can be organized into Jacobian matrices (Section 2.4.1) according to simple rules, a process that can be automated with software (Bowring et al., 2011), ensuring accuracy in what would be many complex equations expressed longhand. The variance and covariance structure of the input variables are arranged in a single covariance matrix (Section 2.4.1), and all other correlation determinations are the product of straightforward matrix multiplication, so there is no propagation of uncertainty through multiple intermediate formulations. In this way, matrix representation ensures that covariance terms are carried through the entire uncertainty propagation calculation, and terms that may become important in the future are never ignored for simplicity. Finally, covariance and Jacobian matrices can be formulated with a block structure if analytical, tracer, and/or decay constant uncertainties are considered independent, so that matrix multiplication is broken down into small, quickly calculated pieces.

2.4.1 Covariance and Jacobian Matrices

Uncertainty propagation using matrix multiplication utilizes two types of matrices, covariance matrices and Jacobian matrices. A covariance matrix describes the uncertainties of a set of variables and how they relate to one another. For n variables, it takes the form

$$\Sigma = \begin{bmatrix} \sigma_1^2 & \sigma_{12}^2 & \cdots & \sigma_{1n}^2 \\ \sigma_{12}^2 & \sigma_2^2 & \cdots & \sigma_{2n}^2 \\ \vdots & \vdots & \ddots & \vdots \\ \sigma_{1n}^2 & \sigma_{2n}^2 & \cdots & \sigma_n^2 \end{bmatrix}$$

Matrix elements in the first row and first column of the covariance matrix relate to the first variable, elements in the second row or second column to the second variable, and so on. Terms on the diagonal of the covariance matrix (e.g. σ_1^2 and σ_2^2) are variances; the off-diagonal elements are covariance terms. For instance, the

matrix element in the first row and second column is the covariance between the first and second variable, σ_{12}^2 . The covariance matrix is symmetric because $\sigma_{12}^2 = \sigma_{21}^2$. Independent, uncorrelated variables have zero covariance.

The other component of linear algebraic uncertainty propagation, a Jacobian matrix, describes a linear transformation from the input parameters to the output variables. In the context of uncertainty propagation, the Jacobian matrix approximates the sensitivity of output variables to small changes in their input parameters as the partial derivative of the function of the output with respect to each input. For a set of m functions f_1 to f_m of n variables x_1 to x_n , a Jacobian matrix takes the form

$$\mathbf{J}_1 = \begin{bmatrix} \frac{\partial f_1}{\partial x_1} & \frac{\partial f_2}{\partial x_1} & \cdots & \frac{\partial f_m}{\partial x_1} \\ \frac{\partial f_1}{\partial x_2} & \frac{\partial f_2}{\partial x_2} & \cdots & \frac{\partial f_m}{\partial x_2} \\ \vdots & \vdots & \ddots & \vdots \\ \frac{\partial f_1}{\partial x_n} & \frac{\partial f_2}{\partial x_n} & \cdots & \frac{\partial f_m}{\partial x_n} \end{bmatrix}$$

Each row of the Jacobian corresponds to an input variable, x_1, x_2, \dots and each column an output, $f_1(x_1, x_2, \dots), f_2(x_1, x_2, \dots)$. Every entry in the matrix is the partial derivative of the column variable with respect to the row variable. If the function f_i is not defined in terms of the input x_j , then the value of the partial derivative $\partial f_i / \partial x_j$ is zero. These derivatives may be calculated after analytical differentiation (e.g., Schmitz and Schoene, 2007; Bowring et al., 2011) or approximated numerically (e.g., Roddick, 1987; Scaillet, 2000).

The data reduction equations (2.2) to (2.51) in Section 2.2 do not express the output variables (e.g. the $^{206}\text{Pb}/^{238}\text{U}$ date) as a lengthy single function of the input parameters (e.g. the measured $^{206}\text{Pb}/^{205}\text{Pb}$). The output isotopic dates and ratios are instead most straightforwardly written in terms of a series of intermediate parameters (e.g., $\text{moles}(^{206}\text{Pb})_{bl}$), which accomplish the calculation in several steps. However, the uncertainty propagation algorithm presented in equation (2.57) requires the partial derivatives of the output z with respect to the inputs x and y .

2.4.2 Calculating the Total Derivative

Because the output isotopic dates and ratios are not defined directly as a function of the input parameters, their partial derivatives are not defined as well. When several intermediate steps precede a final output, its total derivative is required for uncertainty propagation, which incorporates each way the output is contingent upon the input. For instance, the $^{207}\text{Pb}/^{206}\text{Pb}$ date depends on the measured $^{204}\text{Pb}/^{205}\text{Pb}$ in two ways. The measured $^{204}\text{Pb}/^{205}\text{Pb}$ is first fractionation corrected in equation (2.3), then used to calculate both the moles of ^{206}Pb and of ^{207}Pb in the laboratory blank in equations (2.15) and (2.16). The moles of blank of both isotopes are subsequently subtracted from the measured moles ^{206}Pb and ^{207}Pb in equations (2.18) and (2.19) to determine the radiogenic $^{207}\text{Pb}/^{206}\text{Pb}$ ratio (equation 2.46) and the $^{207}\text{Pb}/^{206}\text{Pb}$ date (equation 2.51). Thus the uncertainty in the $^{207}\text{Pb}/^{206}\text{Pb}$ date receives two contributions from the $^{204}\text{Pb}/^{205}\text{Pb}$ uncertainty – from the moles ^{206}Pb and ^{207}Pb . Both contributions are included in the total derivative.

In a linear algebraic framework, total derivatives are calculated by multiplying two or more Jacobian matrices. The rightmost matrix in the matrix product contains partial derivatives of the first set of intermediate parameters with respect to the inputs that define them. For instance, the first Jacobian matrix could contain the moles of ^{205}Pb in the tracer (equation 2.1) and the fractionation-corrected $^{204}\text{Pb}/^{205}\text{Pb}$ ratio (equation 2.3), which are both defined in terms of input parameters. If this matrix is left-multiplied by another Jacobian matrix containing the partial derivatives of the moles of ^{206}Pb and ^{207}Pb in the blank (equations 2.15 and 2.16) with respect to the moles of ^{205}Pb in the tracer and the fractionation-corrected $^{204}\text{Pb}/^{205}\text{Pb}$ ratio, the product will include the total derivative of the moles of ^{206}Pb and ^{207}Pb in the blank with respect to the input parameters.

If f_1 and f_2 are functions of the input parameters x_1 and x_2 , and g_1 and g_2 are in turn functions of f_1 and f_2 , then the total derivative of the functions g_1 and g_2 with

respect to x_1 and x_2 is the product of two Jacobian matrices, \mathbf{J}_1 and \mathbf{J}_2

$$\begin{bmatrix} \frac{dg_1}{dx_1} & \frac{dg_2}{dx_1} \\ \frac{dg_1}{dx_2} & \frac{dg_2}{dx_2} \end{bmatrix} = \begin{bmatrix} \frac{\partial f_1}{\partial x_1} & \frac{\partial f_2}{\partial x_1} \\ \frac{\partial f_1}{\partial x_2} & \frac{\partial f_2}{\partial x_2} \end{bmatrix} \begin{bmatrix} \frac{\partial g_1}{\partial f_1} & \frac{\partial g_2}{\partial f_1} \\ \frac{\partial g_1}{\partial f_2} & \frac{\partial g_2}{\partial f_2} \end{bmatrix} \quad (2.60)$$

$$\text{or} \quad \mathbf{J} = \mathbf{J}_1 \mathbf{J}_2$$

The first column of the matrix product \mathbf{J} is the total derivative of the output function g_1 with respect to each of the input variables x_1 and x_2 ; the second column contains the derivatives of g_2 . Expanding the matrix multiplication for the element in the first row and column of \mathbf{J} reveals

$$\frac{dg_1}{dx_1} = \frac{\partial g_1}{\partial f_1} \frac{\partial f_1}{\partial x_1} + \frac{\partial g_1}{\partial f_2} \frac{\partial f_2}{\partial x_1} \quad (2.61)$$

which is the equation for the total derivative of g_1 with respect to x_1 .

To propagate uncertainties for a more complex system, matrix \mathbf{J}_1 of equation (2.60) can be modified so that it contains rows for n input parameters (x_1, x_2, \dots, x_n) and columns for m intermediate parameters (f_1, f_2, \dots, f_m), where those parameters are expressed as functions of the input parameters. Matrix \mathbf{J}_2 must be adjusted as well to contain m rows for the intermediate parameters in \mathbf{J}_1 , with p columns for the next set of intermediate parameters g_1, g_2, \dots, g_p . Further Jacobian matrices $\mathbf{J}_3, \mathbf{J}_4, \dots$ can be added until the the final set of output parameters has been reached.

This technique is utilized in *U-Pb_Redux*. The partial derivatives of the data reduction equations in Section 2.2 and Appendix 2.8 are calculated during data reduction. These are arranged into approximately ten Jacobian matrices, depending on the tracer and common Pb correction scheme employed, that start with the input variables, step through the intermediate variables, and end with the output isotope ratios and dates. The product is the Jacobian matrix \mathbf{J} , a linearized model of the data reduction equations that contains the total derivatives of the isotopic dates and ratios in Sections 2.2.2 and 2.2.2 and Appendix 2.8 with respect to the user-input parameters in Tables 2.2 to 2.1.

2.4.3 Uncertainty Propagation Equation

Using the covariance and Jacobian matrices assembled above, the uncertainty propagation equation for $z = f(x, y)$ (equation 2.57), can be restated as a matrix product,

$$\sigma_z^2 = \begin{bmatrix} \frac{dz}{dx} & \frac{dz}{dy} \end{bmatrix} \begin{bmatrix} \sigma_x^2 & \sigma_{xy}^2 \\ \sigma_{xy}^2 & \sigma_y^2 \end{bmatrix} \begin{bmatrix} \frac{dz}{dx} \\ \frac{dz}{dy} \end{bmatrix} = \mathbf{J}^T \mathbf{\Sigma} \mathbf{J} \quad (2.62)$$

To calculate the uncertainty and covariance between multiple outputs, the outermost Jacobian matrix contains a column for each output. The matrix product then yields the covariance matrix of the output parameters. For example, if w is also a function of x and y , then by calculating the product

$$\begin{bmatrix} \sigma_z^2 & \sigma_{zw}^2 \\ \sigma_{zw}^2 & \sigma_w^2 \end{bmatrix} = \begin{bmatrix} \frac{dz}{dx} & \frac{dw}{dx} \\ \frac{dz}{dy} & \frac{dw}{dy} \end{bmatrix}^T \begin{bmatrix} \sigma_x^2 & \sigma_{xy}^2 \\ \sigma_{xy}^2 & \sigma_y^2 \end{bmatrix} \begin{bmatrix} \frac{dz}{dx} & \frac{dw}{dx} \\ \frac{dz}{dy} & \frac{dw}{dy} \end{bmatrix} \quad (2.63)$$

the uncertainty in w , σ_w^2 and the covariance between z and w , σ_{zw}^2 fall out.

The covariance matrix $\mathbf{\Sigma}$ can be expanded for any number of inputs, and the Jacobian matrix \mathbf{J} can represent the product of several intermediate Jacobian matrices $\mathbf{J}_1, \mathbf{J}_2, \dots$. In this way, uncertainty propagation for a complex system of inputs, intermediate parameters, and related outputs is represented by a single matrix equation. Because \mathbf{J} contains the total derivatives of the outputs with respect to the inputs, covariance terms do not need to be calculated in uncertainty propagation expressions for every intermediate parameter. The intermediate parameters can now be defined as parameters of interest instead of being formulated to facilitate covariance calculations. An illustration of the U-Pb uncertainty propagation algorithm with populated covariance and Jacobian matrices can be found in the Auxiliary Data for this article.

2.5 Weighted Means

The goal of calculating a weighted mean is to report a single date and uncertainty that best represents the knowledge accumulated by a set of measurements that are assumed to represent a single population with normally distributed uncertainties. Every weighted mean algorithm involves assigning weights, or multipliers which sum to unity, to the measurements, then summing the weighted data. The arithmetic mean gives each of n measurements an equal weight of $1/n$, but a weighted mean may assign a unique weight to each datum so that precise data is weighted more heavily.

2.5.1 Conventional Weighted Mean of Independent Data

For the weighted mean \bar{t} of n independent measurements t_1, \dots, t_n , the weights $\alpha_1, \dots, \alpha_n$ are inversely proportional to the variance of each date, $\sigma_1^2, \dots, \sigma_n^2$, so that

$$\alpha_i = \frac{1}{\sigma_i^2} / \sum_{i=1}^n \left(\frac{1}{\sigma_i^2} \right)$$

where the denominator is used to normalize the sum of the weights. Thus the weighted mean \bar{t} is

$$\bar{t} = \sum_{i=1}^n \alpha_i t_i = \sum_{i=1}^n \left(\frac{t_i}{\sigma_i^2} \right) / \sum_{i=1}^n \left(\frac{1}{\sigma_i^2} \right) \quad (2.64)$$

This choice of weights minimizes the sum of the squared difference between each date and the mean, divided by the date's variance,

$$S = \sum_{i=1}^n \frac{(t_i - \bar{t})^2}{\sigma_i^2} \quad (2.65)$$

The statistic S has a χ^2 distribution with $n - 1$ degrees of freedom. The quotient $S/(n - 1)$ is the 'mean square of weighted deviates' (MSWD) (e.g. Wendt and Carl (1991)), which characterizes the goodness of fit, or how well the weighted mean \bar{t} describes the data t_i . MSWD values close to one indicate that the scatter in the data t_i can be explained by their uncertainties σ_i . Values much lower or greater than one

may indicate that the uncertainties have been over- or under-estimated, respectively. Minimizing S , which also minimizes the MSWD and the uncertainty of \bar{t} , concurrently maximizes the probability that, given the measurements t_1, \dots, t_n , the mean is \bar{t} .

The uncertainty of \bar{t} can be derived using the conventional uncertainty propagation equation. The derivative of \bar{t} with respect to a date, t_i in equation (2.64) is

$$\frac{\partial \bar{t}}{\partial t_i} = \frac{1}{\sigma_i^2} \bigg/ \sum_{i=1}^n \left(\frac{1}{\sigma_i^2} \right) = \alpha_i$$

Assuming that the dates t_1, \dots, t_n have uncorrelated uncertainties, the variance of \bar{t} , according to the uncertainty propagation equation (2.57) is

$$\sigma_{\bar{t}}^2 = \sum_{i=1}^n \left[\left(\frac{\partial \bar{t}}{\partial t_i} \right)^2 \cdot \sigma_i^2 \right] = \sum_{i=1}^n \left[\left(\frac{1}{\sigma_i^2} \right)^2 \bigg/ \left(\sum_{i=1}^n \left(\frac{1}{\sigma_i^2} \right) \right)^2 \cdot \sigma_i^2 \right]$$

Combining numerator terms and factoring out a common denominator yields,

$$\sigma_{\bar{t}}^2 = \sum_{i=1}^n \left[\sigma_i^2 \left(\frac{1}{\sigma_i^2} \right)^2 \right] \bigg/ \left(\sum_{i=1}^n \left(\frac{1}{\sigma_i^2} \right) \right)^2$$

Finally, dividing out a σ_i^2 term in the numerator gives the form x/x^2 , which simplifies to

$$\sigma_{\bar{t}}^2 = 1 \bigg/ \sum_{i=1}^n \left(\frac{1}{\sigma_i^2} \right). \quad (2.66)$$

Equations (2.64) and (2.66) assume, however, that each of the measured dates t_i are independent: that none of their uncertainties share a common systematic contribution. Although these equations can be used to propagate random analytical uncertainties, they cannot assess the systematic contribution of tracer or decay constant uncertainties to a weighted mean date. In the past, systematic errors have been added in quadrature after equations (2.64) and (2.66) are evaluated with analytical uncertainties. However, this approach cannot accurately handle several important scenarios.

First, if a systematic variable affects each analysis differently, it is unclear which

magnitude to add in quadrature. One example is combining analyses with different ratios of tracer to sample. Because the magnitude of the tracer subtraction is different for each, the uncertainty contribution from the subtraction is also different. Also, because the estimated IC of the tracer differs from the true value (within uncertainty), tracer subtraction will introduce some scatter in the results. If the estimated tracer $^{206}\text{Pb}/^{205}\text{Pb}$ ratio is greater than, but within uncertainty of, the true $^{206}\text{Pb}/^{205}\text{Pb}$ ratio, then the moles of radiogenic ^{206}Pb in under-spiked analyses will be over-corrected for the ^{206}Pb in the tracer in equation (2.18), and over-spiked analyses will be over-corrected even further. This scatter, which is introduced by a systematic source, must be considered along with the scatter from random effects during calculation of weighted mean statistics, so that it is not interpreted as ‘geologic scatter.’

Second, it is unclear how to propagate uncertainty which has both a random component and a systematic component with equations (2.64) and (2.66). For instance, correction for Pb fractionation using a single-isotope Pb tracer is usually performed by repeatedly analyzing a certified reference material, e.g. NBS981. The random uncertainty propagated in the fractionation correction is often taken as the long-term reproducibility of this standard, but the uncertainty also contains a systematic component related to the uncertainty in the certified IC of NBS981. The latter cannot be reduced by repeated analyses, which would occur if this uncertainty were considered as analytical and included in σ_i in equation (2.66).

The solution to both of the scenarios above is to treat systematic uncertainties as uncertainty correlations between analyses, yielding a weighted mean, its uncertainty, and an MSWD that is not artificially deflated by misattributed uncertainties.

2.5.2 The Date Covariance Matrix

As Section 2.3.3 details, correlations arise between calculated values when they rely on common parameters. In the case of weighted mean U-Pb dates, two large uncertainty contributions from common parameters are the IC and U/Pb ratio of the tracer, and the decay constant uncertainties. The covariance matrix for a measured dataset of isotopic dates can be constructed with each date’s variance (1σ uncertainty, squared)

on its diagonal. The variance includes uncertainty contributions from both random and systematic effects. Off-diagonal elements characterize the correlation between pairs of dates. Along with the numerical dates themselves, the date covariance matrix, Σ , can then be used to calculate a generalized weighted mean (Lyons et al., 1988; Valassi, 2003) that accounts for both random and systematic uncertainties.

The date covariance matrix can be calculated using the linear algebraic methods presented in Section 2.4.3. The total derivative of each date with respect to each common variable is calculated when multiplying Jacobian matrices during the uncertainty propagation for each fraction (Section 2.4). For instance in equation (2.60), the total derivatives for the output variable g_1 with respect to the inputs x_1, x_2 are found in the first column and first two rows of matrix \mathbf{J} .

Analogously, each column of the product of the Jacobian matrices of the U-Pb uncertainty propagation equations contains the derivatives of the one of the outputs, for instance the $^{206}\text{Pb}/^{238}\text{U}$ date. Several rows in this column contain the derivatives with respect to variables shared with the other dates, such as the tracer parameters and the decay constants. The m rows corresponding to the systematically varying uncertainties in the column corresponding to the $^{206}\text{Pb}/^{238}\text{U}$ date can be extracted from the Jacobian matrix for each of the n fractions to be averaged. The resulting columns are appended to create a new m by n Jacobian matrix, \mathbf{J}_t . Each column of the new matrix corresponds to the $^{206}\text{Pb}/^{238}\text{U}$ date of the n fractions, and each row corresponds to one of the m systematically varying parameters.

Using \mathbf{J}_t and the input covariance matrix for the set of common variables, the systematic covariance matrix Σ_{ts} for the dates can be calculated using equation (2.62),

$$\Sigma_{ts} = \mathbf{J}_t^T \Sigma_s \mathbf{J}_t \quad (2.67)$$

where Σ_s is the m by m covariance matrix of the systematic uncertainties to be propagated and Σ_{ts} is the n by n covariance matrix describing the systematic uncertainty contributions to the n dates. Another n by n covariance matrix Σ_{tr} describes the random (analytical) uncertainties for each date, with the analytical variance for each

date on its diagonal. The covariance matrix Σ for the dates is then the sum of the random and systematic components of uncertainty,

$$\Sigma = \Sigma_{ts} + \Sigma_{tr} \quad (2.68)$$

2.5.3 Generalized Weighted Mean of Correlated Data

The derivation for a generalized weighted mean of correlated measurements is analogous to the derivation for the conventional weighted mean above. Following Lyons et al. (1988), the best linear unbiased estimate (BLUE) of the generalized weighted mean, \hat{t} , given the correlated measurements t_1, \dots, t_n is a weighted linear sum of the data that simultaneously minimizes the uncertainty of the estimate \hat{t} and the MSWD, maximizing the probability that \hat{t} is the mean of the data. The generalized weighted mean can be represented by a sum of scalar products as in equation (2.64), or equivalently as the dot product of two vectors, hereafter displayed in bold, containing the weights and the observed data

$$\hat{t} = \sum_{i=1}^n \alpha_i t_i = \boldsymbol{\alpha}^T \mathbf{t} \quad (2.69)$$

Unlike the conventional weighted mean, there is no simple formula for the generalized weighted mean weights. Instead, the vector of weights, $\boldsymbol{\alpha}$, is determined using the fact that it minimizes the uncertainty in \hat{t} . Analogous to the ‘conventional’ weighted mean derivation, the derivative of \hat{t} with respect to the vector of measured dates \mathbf{t} is

$$\partial \hat{t} / \partial \mathbf{t} = \boldsymbol{\alpha}$$

The resulting vector of derivatives is the Jacobian matrix of the function \hat{t} . Along with the covariance matrix for the measured dates derived in Section 2.5.2, the Jacobian matrix can be substituted into equation (2.62), the linear algebraic uncertainty propagation equation, to yield,

$$\sigma_{\hat{t}}^2 = \boldsymbol{\alpha}^T \Sigma \boldsymbol{\alpha} \quad (2.70)$$

where Σ is the covariance matrix of the dates. Minimizing σ_t^2 subject to the constraint that the sum of the weights in α is unity is most easily accomplished with a Lagrange multiplier.

A common strategy for solving constrained minimization problems, a Lagrange multiplier is introduced to find the extrema of the function $f(\alpha)$ subject to the constraint $g(\alpha) = c$. Here, $f(\alpha)$ is equation (2.70) and the constraint that the sum of the weights equal unity can be restated as a vector product, $\alpha^T \mathbf{1} = 1$, where $\mathbf{1}$ is a n -component column vector of ones. At an extremum of $f(\alpha)$, the gradients of $f(\alpha)$ and $g(\alpha)$ are parallel, although not necessarily the same magnitude. Thus,

$$\nabla f(\alpha) = -\lambda \nabla g(\alpha)$$

and λ is known as the Lagrange multiplier. Utilizing the linearity of the gradient operator, such that $\nabla f + \nabla g = \nabla(f + g)$, both terms can be moved to the left hand side of the equation and combined. Enforcing the constraint that $g(\alpha) = c$ gives

$$\nabla [f(\alpha) + \lambda \cdot (g(\alpha) - c)] = \mathbf{0}$$

where $\mathbf{0}$ is a matrix of zeros. Substituting the generalized weighted mean equation and constraints yields the gradient of a function F ,

$$\nabla F = \nabla [\alpha^T \Sigma \alpha + \lambda \cdot (\alpha^T \mathbf{1} - 1)] = \mathbf{0}$$

The gradient may be decomposed into the partial derivatives with respect to the two variables, α and λ , which both evaluate to zero. Because the covariance matrix Σ is symmetric, $\Sigma^T = \Sigma$, producing two equations,

$$\frac{\partial F}{\partial \alpha} = (\Sigma^T + \Sigma) \alpha + \lambda \mathbf{1} = 2\Sigma \alpha + \lambda \mathbf{1} = \mathbf{0} \quad (2.71)$$

$$\frac{\partial F}{\partial \lambda} = \alpha^T \mathbf{1} - 1 = 0 \quad (2.72)$$

with two unknowns, λ and α .

A solution to this system of equations is found by first solving equation (2.71) for α , then substituting this expression into equation (2.72) and evaluating the transpose,

$$\alpha = -\frac{1}{2}\lambda\Sigma^{-1}\mathbf{1}$$

$$-\left(\frac{1}{2}\lambda\Sigma^{-1}\mathbf{1}\right)^T \mathbf{1} = -\frac{1}{2}\lambda\mathbf{1}^T\Sigma^{-1}\mathbf{1} = 1$$

Where Σ^{-1} is the inverse of the date covariance matrix. Because $\mathbf{1}^T\Sigma^{-1}\mathbf{1}$ is a scalar quantity, it can be moved to the denominator. The resulting equation can be solved for λ and substituted back into equation (2.71), yielding

$$\lambda = -2 / (\mathbf{1}^T\Sigma^{-1}\mathbf{1})$$

$$2\Sigma\alpha + \left[-2 / (\mathbf{1}^T\Sigma^{-1}\mathbf{1})\right] \mathbf{1} = \mathbf{0}$$

Finally, solving for α gives

$$\alpha = \Sigma^{-1}\mathbf{1} / (\mathbf{1}^T\Sigma^{-1}\mathbf{1}) \quad (2.73)$$

To evaluate the generalized weighted mean, the expression for α in equation (2.73) can be substituted into equation (2.69), producing the equation for the generalized weighed mean,

$$\hat{t} = \mathbf{1}^T\Sigma^{-1}\mathbf{t} / (\mathbf{1}^T\Sigma^{-1}\mathbf{1}) \quad (2.74)$$

The expression for α in equation (2.73) can also be substituted into equation (2.70), yielding

$$\sigma_t^2 = (\Sigma^{-1}\mathbf{1})^T \Sigma (\Sigma^{-1}\mathbf{1}) / (\mathbf{1}^T\Sigma^{-1}\mathbf{1})^2$$

Evaluating the transpose and canceling terms in the numerator yields the form x/x^2 , which simplifies to

$$\sigma_t^2 = 1 / (\mathbf{1}^T\Sigma^{-1}\mathbf{1}) \quad (2.75)$$

The variance of the generalized weighed mean is thus equal to the reciprocal of the

sum of the terms in the inverse covariance matrix Σ^{-1} . For the special case when the uncertainties in all dates are independent, Σ and thus Σ^{-1} become diagonal matrices and equation (2.75) evaluates to equation (2.66).

Analogous to equation (2.65), the goodness of fit, or degree to which the weighted mean \bar{t} fits the observed data t_i , is described by the statistic

$$S = \mathbf{r}^T \Sigma^{-1} \mathbf{r} \quad (2.76)$$

where \mathbf{r} is the vector of residuals $r_i = t_i - \hat{t}$. S has a χ^2 distribution with $n - 1$ degrees of freedom, and dividing S by $n - 1$ yields the familiar MSWD.

2.5.4 Application to U-Pb Geochronology

For U-Pb geochronology by ID-TIMS, the largest systematic uncertainty contributions come from the tracer IC and enriched isotope concentrations and from the uncertainty in the decay constants. While analytical uncertainties alone are used to compare U-Pb analyses measured with the same tracer, it is necessary to propagate the tracer uncertainties in order to compare with U-Pb analyses measured with a different tracer. Comparison of U-Pb dates with other decay systems, such as ^{40}Ar - ^{39}Ar , requires propagating the U decay constant uncertainties as well. These three uncertainties are often represented in the form $\pm X/Y/Z$, where X is the analytical uncertainty, Y includes the analytical and tracer contributions, and Z includes the analytical, tracer and decay constant uncertainties (e.g., Schoene and Bowring, 2006).

The generalized weighted mean algorithm is used by *U-Pb_Redux* to calculate X , Y , and Z . The covariance matrix Σ_{tr} of random uncertainties is first assembled by placing the analytical uncertainties for each of n dates along the diagonal of an n by n matrix Σ_{tr} . Evaluating equations (2.73) to (2.76) with $\Sigma = \Sigma_{tr}$ is mathematically equivalent to using equations (2.64) to (2.66) for independent measurements, and gives the uncertainty X .

Following Section 2.5.2, covariance matrices for the dates which contain the tracer and decay constant uncertainties are assembled using equation (2.67). To calculate

Y , only the tracer parameter uncertainties are included in Σ_{ts} , and to calculate Z , both the tracer and decay constant uncertainties are present. The matrix Σ_{ts} for the tracer and decay constants also contains elements for any covariance between the two, which would be incurred if for instance the ^{235}U decay constant were re-calibrated to the ^{238}U decay constant using closed system zircon analyses spiked with the same tracer (Schoene et al., 2006; Mattinson, 2010).

The MSWD calculated using equation (2.76) for the generalized weighted mean is different for X , Y , and Z . We recommend using the MSWD calculated for Z because it accurately incorporates all sources of scatter.

2.6 Verification by Monte Carlo Method

The linear uncertainty propagation equations presented above are based upon several important assumptions. First, in order to interpret output covariance matrices in terms of confidence intervals, for example that $\pm 2\sigma$ approximates a 95% confidence interval (CI) about an isotopic date, the uncertainties of the inputs are all assumed to have normal (Gaussian) probability distributions. This assumption is typically justified using the central limit theorem, which states that the mean of many small random effects is approximately normally distributed, even if the probability distribution of the effects are not.

Most, if not all, uncertainties for ID-TIMS measurements are observed to be normally distributed. The isotope measurements in the numerator and denominator of isotope ratios are assumed to be controlled by Poisson processes, which yield asymmetric Poisson probability distributions for low count rates. However, at the count rates (generally >10 cps) and integration times (generally >100 s total) usually used for U-Pb geochronology by ID-TIMS, these distributions can be closely approximated as Gaussian. In addition, the uncertainties in isotope ratios also contain contributions from other sources, such as resistor noise and beam interpolation. Although a Student's t -distribution is appropriate for discrete data with finite degrees of freedom, U-Pb analyses typically contain >50 ratio measurements, at which point the

Student's t and the normal distributions are almost identical.

Other input uncertainties, such as isotopic fractionation or the blank isotopic composition, can often be measured with higher precision than their external variability. For instance, the variability in the Pb blank IC is most likely due to variable magnitude contributions from various Pb contamination sources, such as ion exchange chemistry and sample loading. The average effect of these small variations, as predicted by the central limit theorem, is an observed normal distribution. This reasoning is also extended to unobservable quantities, such as the Th/U ratio of the magma used for ^{230}Th -correction of $^{206}\text{Pb}/^{238}\text{U}$ dates (e.g. Crowley et al., 2007).

Another assumption made by linear uncertainty propagation, illustrated in Figure 2-3, is that the magnitude of the input uncertainties are small, so that the function $y = f(x)$ is locally linear at the scale of σ_x . This is equivalent to the assumption that the higher order terms in the Taylor series in equation (2.56) are insignificant. Because the data reduction equations are not linear – they involve division, exponentiation, and logarithms – this assumption depends upon the magnitude of the observed input uncertainties. To test whether linear uncertainty propagation algorithm implemented in *U-Pb-Redux* accurately models the uncertainty of isotopic dates with typical ID-TIMS input uncertainties, the Monte Carlo method (MCM) is used.

2.6.1 Monte Carlo Experimental Setup

Implementation of MCM begins by specifying a probability distribution for each input variable (BIPM et al., 2008a; Cox and Siebert, 2006). For this implementation, all input variables are assumed to have multivariate normal probability distributions, but MCM can also be implemented with other (e.g. uniform) input distributions. Next, a pseudorandom number generator is used to produce a random sample, known as a Monte Carlo trial, from the input probability distribution for each parameter. These values are used to calculate the output variables, e.g. isotopic dates, and then the process is repeated M times. The resulting distribution of the M values for an output approximates its probability distribution, and if several outputs are calculated from the same input trials, the result approximates their joint probability distribution,

which describes their correlation as well.

There are multiple ways to interpret the output of a Monte Carlo model. If the M calculated output variables are normally distributed, then two standard deviations about the mean is a good estimate of the 95% CI. When the results are not normally distributed, then multiple 95% CIs can be reported. The two most popular are the 95% CI that is symmetric about the mean of the distribution and the shortest 95% CI (BIPM et al., 2008a). For probability distributions close to normal, the form of the first is most familiar and is used here.

2.6.2 Results

The MCM has been utilized before for U-Pb data (Briqueu and de la Boisse, 1990), but never in the context of calculating radiogenic U-Pb dates from measured data or testing a U-Pb uncertainty propagation algorithm. Here we present data for three ID-TIMS zircon analyses with typical analytical uncertainties. The mathematical programming environment MATLAB was used to generate $M = 10^6$ multivariate normal Monte Carlo trials from the measured and estimated input parameters and uncertainties. The results of Monte Carlo method modeling are plotted as histograms and best-fit normal distributions and presented in Figure 2-4.

The first analysis modeled by MCM is an Eocene zircon with a Pb^*/Pbc , or ratio of total radiogenic to common Pb, of ~ 18 . The measured $^{206}\text{Pb}/^{205}\text{Pb}$ and $^{207}\text{Pb}/^{205}\text{Pb}$ uncertainties are 0.025% and 0.090%, respectively. *U-Pb_Redux* calculates a $^{206}\text{Pb}/^{238}\text{U}$ date of 47.860 ± 0.041 Ma (2σ). Visual inspection of the histogram in Figure 2-4a reveals that the Monte Carlo trials closely approximate a normal distribution. The mean and twice the standard deviation of the 10^6 trials yields 47.860 ± 0.041 Ma (2σ), agreeing to the numerical precision represented by two significant figures in the reported uncertainty. The $^{207}\text{Pb}/^{235}\text{U}$ date for this analysis was also modeled by MCM, although this date is not usually reported in this age range because it is generally less precise. The Monte Carlo trials plotted in Figure 2-4b are also normally distributed, and the date calculated by *U-Pb_Redux* and the Monte Carlo results both agree at 48.12 ± 0.33 Ma (2σ).

The second analysis modeled is an Archean zircon with a Pb^*/Pbc of ~ 85 and measured $^{206}Pb/^{205}Pb$ and $^{207}Pb/^{205}Pb$ uncertainties of 0.022% and 0.029%, respectively. A histogram showing Monte Carlo evaluations of the $^{207}Pb/^{206}Pb$ date is presented in Figure 2-4c, and approximates a normal distribution closely. The date and uncertainty of 2576.0 ± 1.5 (2σ) calculated by *U-Pb_Redux* again agree with the mean and two standard deviations of the 10^6 Monte Carlo realizations within numerical precision.

Finally, a < 1 Ma zircon from the Bishop Tuff with a Pb^*/Pbc of 4.6 and a measured $^{206}Pb/^{205}Pb$ uncertainty of 0.054% was modeled with MCM. For an analysis this young, the uncertainties in the ^{230}Th correction (Appendix 2.8) dominate the uncertainty budget. Here, the Th/U of the magma was assumed to have the same variability as Th/U ratios measured in melt inclusions in quartz phenocrysts, 2.81 ± 0.32 (2σ) (Crowley et al., 2007). Visual inspection of the histogram in Figure 2-4d reveals a distribution slightly skewed to the left. This results from a non-linearity in the ^{230}Th correction: Monte Carlo trials with lower magma Th/U values result in a range of Th-corrections, rather than trials with higher Th/U magma values where the near-maximum correction is made. The linear uncertainty propagation algorithm employed by *U-Pb_Redux*, calculates a ^{230}Th -corrected $^{206}Pb/^{238}U$ date of 768.6 ± 3.3 ka (2σ). This is approximated closely by the mean and symmetric 95% confidence interval calculated from the Monte Carlo realizations of 768.5 ± 3.3 ka, with a difference between the expected values of only 78 years.

2.7 Conclusions

We propose that the ID-TIMS community adopt a common U-Pb data reduction and uncertainty propagation algorithm for reporting, comparing, and archiving a rapidly growing amount of isotopic data. An ideal algorithm must provide a transparent model to calculate dates from input measurement, tracer, and laboratory parameters for a variety of tracers and for phases with and without initial common Pb, incorporating initial daughter product disequilibrium corrections. This model should also

propagate the uncertainties in each input parameter, as well as any possible correlations between them, to determine the uncertainties and correlations between the variety of output isotopic ratios and dates geochronologists plot and interpret. Finally, a mechanism is required for combining several analyses into a single maximum likelihood estimate of the date and uncertainty they represent, incorporating random and multiple systematic uncertainties.

A new set of data reduction and uncertainty estimation algorithms fulfill these criteria and are embedded in the open source software package *U-Pb_Redux*. Uncertainty propagation using the linear algebraic expression of covariance and Jacobian matrices is highly extensible, so that relationships between inputs, intermediate parameters, and outputs are easily codified and calculations are computationally inexpensive. This approach also determines the dependence of each measurement on often complexly related systematic uncertainties. If these systematic uncertainties are expressed as correlations between the dates being averaged, then the same linear algebraic linear uncertainty propagation techniques can be used to calculate the weighted mean dates and statistics.

Interpreting uncertainties propagated linearly as confidence intervals assumes the model is linear at the scale of the input uncertainties. This assumption is tested and verified with Monte Carlo simulations of three typical zircon analyses, which show that typical ID-TIMS uncertainties yield normal distributions that agree with linear uncertainty propagation calculations.

2.8 Appendix: Disequilibrium Corrections and Initial Common Pb Models

The U-Pb data reduction equations presented in Section 2.2 assume that one daughter atom of ^{206}Pb or ^{207}Pb is created from the decay of each parent atom of ^{238}U or ^{235}U , respectively. However, the path from U to Pb in each system proceeds through a series of alpha and beta decays that produce a chain of intermediate daughter nu-

clides before yielding a Pb atom. The U-series decay chain is at ‘secular equilibrium’ when all isotopes have the same activity (equal to its decay constant multiplied by its atomic abundance), so that each intermediate daughter is being created from the nuclide before it in the chain at the same rate as it is decaying to the next daughter nuclide. This results in a higher abundance of daughter nuclides with longer half lives. Chemical processes that fractionate the parent and intermediate daughter nuclides disturb the secular equilibrium abundance ratios, creating intermediate daughter product disequilibrium.

For instance, the elements U and Th are fractionated during crystallization of a dated phase if their distribution coefficients in that phase differ (i.e., $D_{Th} \neq D_U$). This affects the longest-lived intermediate daughter product in the ^{238}U decay chain, ^{230}Th ($t_{1/2} \approx 76$ kyr). Th is relatively incompatible compared to U during crystallization of zircon, for example, resulting in a ^{230}Th deficiency, and it is compatible in monazite, resulting in ^{230}Th excess (Mattinson, 1973; Schärer, 1984). In order for the ^{230}Th to return to secular equilibrium, it must accumulate at the expense of ^{206}Pb production in zircon or decay back to secular equilibrium levels in monazite, generating excess ^{206}Pb . The resulting age correction for zircon is bounded: if Th is completely excluded from the crystal, the maximum correction of $1/\lambda_{230} \approx 110$ kyr is made to the $^{206}\text{Pb}/^{238}\text{U}$ date. However, if the mineral incorporates excess ^{230}Th , then no upper bound exists on the theoretical magnitude of the age correction.

2.8.1 Th correction derivation

Initial ^{230}Th disequilibrium in the ^{238}U decay chain necessitates a correction to the molar quantity of ^{206}Pb in the conventional age equation, $D = P(e^{\lambda t} - 1)$:

$$\begin{aligned} \text{moles}(^{206}\text{Pb})_{rad} &= \text{moles}(^{238}\text{U})_{spl} \cdot \left(e^{\lambda_{238} t_{206/238}^{Th}} - 1 \right) \\ &\quad + \text{moles}(^{230}\text{Th})_{init} - \text{moles}(^{230}\text{Th})_{eqbm} \end{aligned} \quad (2.77)$$

where $t_{206/238}^{Th}$ is the $^{206}\text{Pb}/^{238}\text{U}$ date of the sample corrected for initial ^{230}Th disequilibrium. The difference between the moles of ^{230}Th at initial crystallization and the

moles of ^{230}Th at secular equilibrium is negative if Th has been excluded from the mineral, decreasing the moles of ^{206}Pb subsequently produced, or positive if Th has been preferentially included into the mineral, generating excess ^{206}Pb .

Molar quantities in equation (2.77) can be expressed as isotopic abundance ratios by dividing through by the moles of parent isotope, ^{238}U . Due to the long half life of ^{238}U (~ 4.5 Gyr), its atomic abundance is assumed to be the same at crystallization and after returning to secular equilibrium, which occurs after about six half lives of the longest lived intermediate daughter, or ~ 460 kyr, if all ^{230}Th is excluded.

$$\left(\frac{^{206}\text{Pb}}{^{238}\text{U}}\right)_{rad} = e^{\lambda_{238} \cdot t_{206/238}} - 1 + \left(\frac{^{230}\text{Th}}{^{238}\text{U}}\right)_{init} - \left(\frac{^{230}\text{Th}}{^{238}\text{U}}\right)_{eqbm} \quad (2.78)$$

The Th/U ratios on the right hand side of equation (2.78) can be expressed as activity ratios by multiplying the atomic abundance of each isotope by its decay constant. Equality is maintained by multiplying the resulting expression by the reciprocal of the decay constant ratio.

$$\begin{aligned} \left(\frac{^{230}\text{Th}}{^{238}\text{U}}\right)_{init} - \left(\frac{^{230}\text{Th}}{^{238}\text{U}}\right)_{eqbm} &= \frac{\lambda_{238}}{\lambda_{230}} \left(\frac{\lambda_{230}}{\lambda_{238}} \left(\frac{^{230}\text{Th}}{^{238}\text{U}}\right)_{init} - \frac{\lambda_{230}}{\lambda_{238}} \left(\frac{^{230}\text{Th}}{^{238}\text{U}}\right)_{eqbm} \right) \\ &= \frac{\lambda_{238}}{\lambda_{230}} \left(\left[\frac{^{230}\text{Th}}{^{238}\text{U}}\right]_{init} - \left[\frac{^{230}\text{Th}}{^{238}\text{U}}\right]_{eqbm} \right) \end{aligned} \quad (2.79)$$

where the square brackets enclose activity ratios.

Both activity ratios in expression (2.79) may be transformed into measurable parameters. The degree of initial isotopic disequilibrium depends on the ratio between the distribution coefficients D_{Th} and D_{U} . Each distribution coefficient describes the ratio of the molar abundance of Th and U in the sample to the molar abundance in the magma. This expression can be rearranged so that the the abundance ratio of sample isotopes is in the numerator and the corresponding magma abundance ratio is in the denominator.

$$\frac{D_{\text{Th}}}{D_{\text{U}}} = \frac{\text{Th}_{spl} / \text{Th}_{magma}}{\text{U}_{spl} / \text{U}_{magma}} = \frac{(\text{Th}/\text{U})_{spl}}{(\text{Th}/\text{U})_{magma}} \quad (2.80)$$

Fractionation of specific isotopes, such as ^{230}Th and ^{238}U , follow the same rule, yielding an equivalent expression in terms of the initial molar $^{230}\text{Th}/^{238}\text{U}$ ratio of the sample and the magma. The molar ratio can again be converted to an activity ratio by multiplying each isotope by its decay constant.

$$\frac{(\text{Th}/\text{U})_{spl}}{(\text{Th}/\text{U})_{magma}} = \frac{(^{230}\text{Th}/^{238}\text{U})_{init}}{(^{230}\text{Th}/^{238}\text{U})_{magma}} \cdot \frac{\lambda_{230}/\lambda_{238}}{\lambda_{230}/\lambda_{238}} \quad (2.81)$$

The numerator and denominator become activity ratios, denoted by square brackets. Assuming that the magma is at secular equilibrium at crystallization, its activity ratio $[^{230}\text{Th}/^{238}\text{U}]_{magma} = 1$.

$$\frac{(\text{Th}/\text{U})_{spl}}{(\text{Th}/\text{U})_{magma}} = \frac{[^{230}\text{Th}/^{238}\text{U}]_{init}}{[^{230}\text{Th}/^{238}\text{U}]_{magma}} = \left[\frac{^{230}\text{Th}}{^{238}\text{U}} \right]_{init} \quad (2.82)$$

Thus, the initial $[^{230}\text{Th}/^{238}\text{U}]$ activity ratio is equivalent to the ratio of distribution coefficients $D_{\text{Th}} / D_{\text{U}}$, and the Th/U of the sample divided by the Th/U of the magma. Instead of assuming the magma to be at secular equilibrium, both may be multiplied by the $[^{230}\text{Th}/^{238}\text{U}]$ activity ratio of the magma to yield the initial $[^{230}\text{Th}/^{238}\text{U}]$ activity ratio at crystallization if constraints exist on its value.

Finally, the $[^{230}\text{Th}/^{238}\text{U}]$ activity ratio of the sample after it has attained secular equilibrium is also equal to one,

$$\left[\frac{^{230}\text{Th}}{^{238}\text{U}} \right]_{eqbm} = 1 \quad (2.83)$$

Substituting the re-cast activity ratios in (2.82) and (2.83) into (2.79), then substituting this expression into (2.78) yields the conventional equation for the ^{230}Th -corrected $^{206}\text{Pb}/^{238}\text{U}$ date (e.g., Schärer, 1984),

$$\left(\frac{^{206}\text{Pb}}{^{238}\text{U}} \right)_{rad} = e^{\lambda_{238} t_{206/238}^{Th}} - 1 + \frac{\lambda_{238}}{\lambda_{230}} \cdot \left[\left(\frac{\text{Th}}{\text{U}} \right)_{spl} / \left(\frac{\text{Th}}{\text{U}} \right)_{magma} - 1 \right] \quad (2.84)$$

Alternately, if the ratio of distribution coefficients $D_{\text{Th}}/D_{\text{U}}$ is better constrained than the Th/U of the magma, the left side of equation (2.80) can be substituted into

equation (2.84),

$$\left(\frac{^{206}\text{Pb}}{^{238}\text{U}}\right)_{rad} = e^{\lambda_{238} \cdot t_{206/238}^{Th}} - 1 + \frac{\lambda_{238}}{\lambda_{230}} \cdot \left(\frac{D_{\text{Th}}}{D_{\text{U}}} - 1\right) \quad (2.85)$$

2.8.2 Th correction implementation

In order to calculate the ^{230}Th -corrected $^{206}\text{Pb}/^{238}\text{U}$ date in equation (2.84), an estimate of the Th/U of the magma is required; the Th/U of the sample may be calculated from available data. Because the Th/U of the magma is expressed as an atomic abundance ratio, the total atomic abundances of Th and U in the sample are required, which are each the sum of the abundances of the respective major isotopes. The atomic abundance of U in the sample, $moles(\text{U})_{spl}$, is the sum of the moles of ^{238}U and ^{235}U ,

$$moles(\text{U})_{spl} = moles(^{238}\text{U})_{spl} + moles(^{235}\text{U})_{spl} \quad (2.86)$$

The element Th has a single major isotope, ^{232}Th ; the second largest contribution, from the ^{230}Th in the ^{238}U decay chain, is negligible. Due to the long half-life of ^{232}Th (~ 14 Gyr), there is no significant difference between the abundance of Th at present and during crystallization. The atomic abundance of ^{232}Th in the sample can be back-calculated from the moles of radiogenic ^{208}Pb derived in equation (2.23) and the ^{230}Th -corrected date of the sample. The moles of ^{232}Th in the sample is given by a rearrangement of the isotopic decay equation, $D/P = e^{\lambda t} - 1$,

$$moles(^{232}\text{Th})_{spl} = \frac{moles(^{208}\text{Pb})_{rad}}{\exp\left(\lambda_{232} \cdot t_{206/238}^{Th}\right) - 1} \quad (2.87)$$

where $t_{206/238}^{Th}$ is the ^{230}Th -corrected $^{206}\text{Pb}/^{238}\text{U}$ date.

The expressions in (2.86) and (2.87) can be substituted into equation (2.84) to yield a new equation

$$\left(\frac{^{206}\text{Pb}}{^{238}\text{U}}\right)_{rad} = e^{\lambda_{238} \cdot t_{206/238}^{Th}} - 1 + \frac{\lambda_{238}}{\lambda_{230}} \cdot$$

$$\left[\frac{\text{moles}({}^{208}\text{Pb})_{rad} / \left(e^{\lambda_{232} \cdot t_{206/238}^{Th}} - 1 \right)}{\text{moles}(\text{U})_{spl}} \right] / \left[\left(\frac{\text{Th}}{\text{U}} \right)_{magma} - 1 \right]$$

This equation cannot be solved directly for $t_{206/238}^{Th}$, so *U-Pb-Redux* utilizes Newton's Method, an iterative numerical solution.

Alternately, equation (2.85) can be solved directly for $t_{206/238}^{Th}$ if the ratio of distribution coefficients is known,

$$t_{206/238}^{Th} = \frac{1}{\lambda_{238}} \log \left[\left(\frac{{}^{206}\text{Pb}}{{}^{238}\text{U}} \right)_{rad} + 1 - \frac{\lambda_{238}}{\lambda_{230}} \left(\frac{\text{D}_{\text{Th}}}{\text{D}_{\text{U}}} - 1 \right) \right] \quad (2.88)$$

Using the ${}^{230}\text{Th}$ -corrected ${}^{206}\text{Pb}/{}^{238}\text{U}$ date calculated in equation (2.88) or (2.88), it is possible to calculate the moles of ${}^{232}\text{Th}$ in the sample (equation 2.87), as well as the Th-corrected moles of ${}^{206}\text{Pb}$,

$$\text{moles}({}^{206}\text{Pb})_{rad}^{Th} = \text{moles}({}^{238}\text{U})_{spl} \left(e^{\lambda_{238} \cdot t_{206/238}^{Th}} - 1 \right) \quad (2.89)$$

and the Th-corrected ${}^{206}\text{Pb}/{}^{238}\text{U}$ ratio used in the conventional concordia plot,

$$\left(\frac{{}^{206}\text{Pb}}{{}^{238}\text{U}} \right)_{rad}^{Th} = \frac{\text{moles}({}^{206}\text{Pb})_{rad}^{Th}}{\text{moles}({}^{238}\text{U})_{spl}} \quad (2.90)$$

A ${}^{230}\text{Th}$ correction is most often applied to samples younger than ca. 500 Ma, whose uncertainties are comparable to the magnitude of the correction. The ${}^{207}\text{Pb}/{}^{206}\text{Pb}$ date is not often used for young (< ca. 2 Ga) samples because it is sensitive to the low abundance of ${}^{207}\text{Pb}$ in young samples. However, Amelin et al. (2010) show that evolving laboratory and mass spectrometry techniques applied to early solar system studies offer ever-finer resolving power at >4.5 Ga suggesting that Th correction may become necessary. The ${}^{230}\text{Th}$ -corrected radiogenic ${}^{207}\text{Pb}/{}^{206}\text{Pb}$ ratio is

$$\left(\frac{{}^{207}\text{Pb}}{{}^{206}\text{Pb}} \right)_{rad}^{Th} = \frac{\text{moles}({}^{207}\text{Pb})_{rad}}{\text{moles}({}^{206}\text{Pb})_{rad}^{Th}} \quad (2.91)$$

As with the un-corrected ${}^{207}\text{Pb}/{}^{206}\text{Pb}$ date, a solution for $t_{207/206}^{Th}$ cannot be reached

analytically for the equation

$$\left(\frac{^{207}\text{Pb}}{^{206}\text{Pb}}\right)_{rad}^{Th} = \left(\frac{^{238}\text{U}}{^{235}\text{U}}\right)_{spl}^{-1} \cdot \frac{\exp\left(\lambda_{235} \cdot t_{207/206}^{Th}\right) - 1}{\exp\left(\lambda_{238} \cdot t_{207/206}^{Th}\right) - 1} \quad (2.92)$$

Instead, Newton's Method is employed by *U-Pb_Redux*.

2.8.3 Pa correction

The longest-lived intermediate daughter product in the ^{235}U decay chain is ^{231}Pa , with a half life of ~ 33 kyr. Analogous to ^{230}Th in the ^{238}U decay chain, the $[\text{^{231}Pa}/\text{^{235}U}]$ activity ratio may be perturbed during crystallization from a magma at secular equilibrium. Unlike the ^{230}Th correction, however, there is no way to back-calculate the initial Pa/U ratio of the dated phase, as with the ^{208}Pb daughter of ^{232}Th in equation (2.88). Instead, correction requires the initial $[\text{^{231}Pa}/\text{^{235}U}]$ activity ratio at crystallization or $D_{\text{Pa}}/D_{\text{U}}$, the ratio of the Pa and U distribution coefficients in the dated phase. Derivation of the the ^{231}Pa correction equations parallels the ^{230}Th equations presented above.

The ^{231}Pa -corrected $^{207}\text{Pb}/^{235}\text{U}$ date, $t_{207/235}^{Pa}$, can be calculated in the same manner as equation (2.88).

$$t_{207/235}^{Pa} = \frac{1}{\lambda_{235}} \log \left[\left(\frac{^{207}\text{Pb}}{^{235}\text{U}}\right)_{rad} + 1 - \frac{\lambda_{235}}{\lambda_{231}} \left(\left[\frac{^{231}\text{Pa}}{^{235}\text{U}}\right]_{spl} - 1 \right) \right] \quad (2.93)$$

Likewise, ^{231}Pa -corrected moles of ^{207}Pb can be calculated using the corrected $^{207}\text{Pb}/^{235}\text{U}$ date,

$$\text{moles}(^{207}\text{Pb})_{rad}^{Pa} = \text{moles}(^{235}\text{U})_{spl} \left(e^{\lambda_{235} \cdot t_{207/235}^{Pa}} - 1 \right) \quad (2.94)$$

and then used to calculate the ^{231}Pa -corrected radiogenic $^{207}\text{Pb}/^{206}\text{Pb}$ ratio,

$$\left(\frac{^{207}\text{Pb}}{^{206}\text{Pb}}\right)_{rad}^{Pa} = \frac{\text{moles}(^{207}\text{Pb})_{rad}^{Pa}}{\text{moles}(^{206}\text{Pb})_{rad}} \quad (2.95)$$

and the ^{231}Pa -corrected radiogenic $^{207}\text{Pb}/^{235}\text{U}$ ratio,

$$\left(\frac{^{207}\text{Pb}}{^{235}\text{U}}\right)_{rad}^{Pa} = \frac{\text{moles}(^{207}\text{Pb})_{rad}^{Pa}}{\text{moles}(^{235}\text{U})_{spl}} \quad (2.96)$$

for Tera-Wasserburg and conventional concordia plots.

To calculate a ^{231}Pa -corrected $^{207}\text{Pb}/^{206}\text{Pb}$ date, it is not possible to solve

$$\left(\frac{^{207}\text{Pb}}{^{206}\text{Pb}}\right)_{rad}^{Pa} = \left(\frac{^{238}\text{U}}{^{235}\text{U}}\right)_{spl}^{-1} \cdot \frac{\exp(\lambda_{235} \cdot t_{207/206}^{Pa}) - 1}{\exp(\lambda_{238} \cdot t_{207/206}^{Pa}) - 1} \quad (2.97)$$

directly for $t_{207/206}^{Pa}$. Instead, an iterative numerical solution such as Newton's Method must be employed.

2.8.4 Simultaneous Th- and Pa-correction

Finally, the $^{207}\text{Pb}/^{206}\text{Pb}$ ratio and date may be corrected for both ^{230}Th and ^{231}Pa disequilibrium using equations (2.89) and (2.94).

$$\left(\frac{^{207}\text{Pb}}{^{206}\text{Pb}}\right)_{rad}^{ThPa} = \frac{\text{moles}(^{207}\text{Pb})_{rad}^{Pa}}{\text{moles}(^{206}\text{Pb})_{rad}^{Th}} \quad (2.98)$$

To calculate a ^{230}Th - and ^{231}Pa -corrected $^{207}\text{Pb}/^{206}\text{Pb}$ date, it is not possible to solve

$$\left(\frac{^{207}\text{Pb}}{^{206}\text{Pb}}\right)_{rad}^{ThPa} = \left(\frac{^{238}\text{U}}{^{235}\text{U}}\right)_{spl}^{-1} \cdot \frac{\exp(\lambda_{235} \cdot t_{207/206}^{ThPa}) - 1}{\exp(\lambda_{238} \cdot t_{207/206}^{ThPa}) - 1} \quad (2.99)$$

in terms of $t_{207/206}^{ThPa}$. Instead, an iterative numerical solution is used.

2.8.5 Initial Common Pb Correction

Following Stacey and Kramers (1975), for fractions with estimated dates between 4.57 and 3.7 Ga,

$$\left(\frac{^{206}\text{Pb}}{^{204}\text{Pb}}\right)_{com} = 7.19 \cdot \left[e^{(\lambda_{238} \cdot 4.57 \times 10^9)} - e^{(\lambda_{238} \cdot t_{\text{Pbc}})} \right] + 9.307 \quad (2.100)$$

$$\left(\frac{^{207}\text{Pb}}{^{204}\text{Pb}}\right)_{com} = \frac{7.19}{137.88} \cdot \left[e^{(\lambda_{235} \cdot 4.57 \times 10^9)} - e^{(\lambda_{235} \cdot t_{\text{Pbc}})} \right] + 10.294 \quad (2.101)$$

$$\left(\frac{^{208}\text{Pb}}{^{204}\text{Pb}}\right)_{com} = 33.21 \cdot \left[e^{(\lambda_{232} \cdot 4.57 \times 10^9)} - e^{(\lambda_{232} \cdot t_{\text{Pbc}})} \right] + 29.487 \quad (2.102)$$

and for fractions younger than 3.7 Ga,

$$\left(\frac{^{206}\text{Pb}}{^{204}\text{Pb}}\right)_{com} = 9.74 \cdot \left[e^{(\lambda_{238} \cdot 3.7 \times 10^9)} - e^{(\lambda_{238} \cdot t_{\text{Pbc}})} \right] + 11.152 \quad (2.103)$$

$$\left(\frac{^{207}\text{Pb}}{^{204}\text{Pb}}\right)_{com} = \frac{9.74}{137.88} \cdot \left[e^{(\lambda_{235} \cdot 3.7 \times 10^9)} - e^{(\lambda_{235} \cdot t_{\text{Pbc}})} \right] + 12.998 \quad (2.104)$$

$$\left(\frac{^{208}\text{Pb}}{^{204}\text{Pb}}\right)_{com} = 36.84 \cdot \left[e^{(\lambda_{232} \cdot 3.7 \times 10^9)} - e^{(\lambda_{232} \cdot t_{\text{Pbc}})} \right] + 31.23 \quad (2.105)$$

2.9 Figure captions

Figure 2-1: Diagrammatic representation of the data reduction algorithm. Data reduction begins with the input parameters in the boxes at left. Sections 2.2.2 and 2.2.2 describe how the blank and tracer parameters are combined to calculate their molar abundances. These are then used to correct the measured ratios in Sections 2.2.2 and 2.2.2 in order to determine the moles of parent Pb and radiogenic U, respectively. Finally, Sections 2.2.2 and 2.2.2 calculate radiogenic U/Pb ratios and and, using the isotopic decay constants, isotopic dates.

Figure 2-2: Cartoon illustrating the relative contributions of Pb and U sample components for typical U-Pb ID-TIMS analyses, broken down by isotope. Column heights are not shown to scale. (a) Relative abundance of Pb isotopes in a phase that incorporates initial common Pb (Pbc). Determination of the radiogenic ^{206}Pb , ^{207}Pb , and ^{208}Pb shown in red requires subtracting the tracer, blank, and initial Pbc contributions from the top of each column. The tracer contribution is estimated from the ^{205}Pb abundance and the tracer isotopic composition (IC) and the Pb blank contribution is estimated laboratory measurements. The remaining ^{204}Pb is assumed to be initial Pbc; its contributions to the radiogenic isotopes are subtracted using the initial Pbc IC, leaving only the radiogenic component. (b) For a phase with no initial Pbc, only tracer and blank contributions need to be subtracted to determine the radiogenic component. The ^{204}Pb contribution from the tracer is subtracted first using the ^{205}Pb abundance of the tracer, and the remaining ^{204}Pb is assumed to be laboratory Pb blank. Subtracting the blank contributions to ^{206}Pb , ^{207}Pb , and ^{208}Pb using the blank IC yields their radiogenic components. (c) Relative abundance of U isotopes. The isotopic tracer may contain any combination of ^{233}U , ^{235}U , and/or ^{236}U . The tracer, blank, and sample U contributions to each isotope are deconvolved by solving a system of equations that incorporates the IC of each.

Figure 2-3: Illustration of linear uncertainty propagation for a single input parameter. Uncertainty in the x direction (σ_x) of the point (x, y) results in an uncertainty σ_y in the function $y = f(x)$ that is proportional to the partial derivative of y

with respect to x . This estimate is accurate if the function $f(x)$ can be approximated by its derivative at the scale of σ_x .

Figure 2-4: Histograms illustrating the results of 10^6 Monte Carlo simulations for three representative ID-TIMS zircon analyses. Red curves are normal distributions corresponding to the date and uncertainty calculated by *U-Pb_Redux*. (a) Monte Carlo simulations of the $^{206}\text{Pb}/^{238}\text{U}$ date of an Eocene zircon, (b) the $^{207}\text{Pb}/^{235}\text{U}$ date of the same analysis, and (c) the $^{207}\text{Pb}/^{206}\text{Pb}$ date of an Archean zircon are normally distributed, with the same mean and uncertainty calculated by *U-Pb_Redux*. The distribution of Monte Carlo trials for a young Th-corrected Bishop Tuff grain (d) is slightly right-skewed but can be closely approximated by its linear uncertainty propagation result.

Table 2.1: Measured Isotope Ratios

Pb	U or Uoxide
$\left(\frac{^{204}\text{Pb}}{^{205}\text{Pb}}\right)_{meas}$	$\left(\frac{^{233}\text{U}}{^{235}\text{U}}\right)_{meas}$ or $\left(\frac{^{265}\text{UO}_2}{^{267}\text{UO}_2}\right)_{meas}$
$\left(\frac{^{206}\text{Pb}}{^{205}\text{Pb}}\right)_{meas}$	$\left(\frac{^{238}\text{U}}{^{235}\text{U}}\right)_{meas}$ or $\left(\frac{^{270}\text{UO}_2}{^{267}\text{UO}_2}\right)_{meas}$
$\left(\frac{^{207}\text{Pb}}{^{205}\text{Pb}}\right)_{meas}$	$\left(\frac{^{233}\text{U}}{^{236}\text{U}}\right)_{meas}$ or $\left(\frac{^{265}\text{UO}_2}{^{268}\text{UO}_2}\right)_{meas}$
$\left(\frac{^{208}\text{Pb}}{^{205}\text{Pb}}\right)_{meas}$	$\left(\frac{^{238}\text{U}}{^{236}\text{U}}\right)_{meas}$ or $\left(\frac{^{270}\text{UO}_2}{^{268}\text{UO}_2}\right)_{meas}$
$\left(\frac{^{202}\text{Pb}}{^{205}\text{Pb}}\right)_{meas}$	

Table 2.2: Isotopic Tracer Parameters

Pb IC	U IC	Tracer Calibration
$\left(\frac{^{204}\text{Pb}}{^{205}\text{Pb}}\right)_{tr}$	$\left(\frac{^{233}\text{U}}{^{235}\text{U}}\right)_{tr}$	$\left(\frac{^{205}\text{Pb}}{^{235}\text{U}}\right)_{tr}$
$\left(\frac{^{206}\text{Pb}}{^{205}\text{Pb}}\right)_{tr}$	$\left(\frac{^{238}\text{U}}{^{235}\text{U}}\right)_{tr}$	$conc(^{205}\text{Pb})_{tr}$
$\left(\frac{^{207}\text{Pb}}{^{205}\text{Pb}}\right)_{tr}$	$\left(\frac{^{233}\text{U}}{^{236}\text{U}}\right)_{tr}$	$conc(^{235}\text{U})_{tr}$
$\left(\frac{^{208}\text{Pb}}{^{205}\text{Pb}}\right)_{tr}$		$mass_{tr}$
$\left(\frac{^{202}\text{Pb}}{^{205}\text{Pb}}\right)_{tr}$		

Table 2.3: Laboratory and Sample Parameters

Pb Blank	Initial Pb_c	Uranium
$\left(\frac{^{206}\text{Pb}}{^{204}\text{Pb}}\right)_{bl}$	$\left(\frac{^{206}\text{Pb}}{^{204}\text{Pb}}\right)_{com}$	$\left(\frac{^{238}\text{U}}{^{235}\text{U}}\right)_{spl}$
$\left(\frac{^{207}\text{Pb}}{^{204}\text{Pb}}\right)_{bl}$	$\left(\frac{^{207}\text{Pb}}{^{204}\text{Pb}}\right)_{com}$	$\left(\frac{^{238}\text{U}}{^{235}\text{U}}\right)_{bl}$
$\left(\frac{^{208}\text{Pb}}{^{204}\text{Pb}}\right)_{bl}$	$\left(\frac{^{208}\text{Pb}}{^{204}\text{Pb}}\right)_{com}$	$\left(\frac{^{18}\text{O}}{^{16}\text{O}}\right)_{Uox}$
$mass(\text{Pb})_{bl}$	t_{Pbc}	$mass(\text{U})_{bl}$
Fractionation Correction	Disequilibrium Correction	Physical Constants
α_{Pb}	$\left(\frac{\text{Th}}{\text{U}}\right)_{\text{magma}}$	$\lambda_{238}, \lambda_{235}, \lambda_{232}$ $\lambda_{231}, \lambda_{230}$
α_{U}	$\left[\frac{^{231}\text{Pa}}{^{235}\text{U}}\right]_{spl}$	$\left[\frac{\text{grams}(^{204}\text{Pb})}{\text{mole}(^{204}\text{Pb})}\right]$

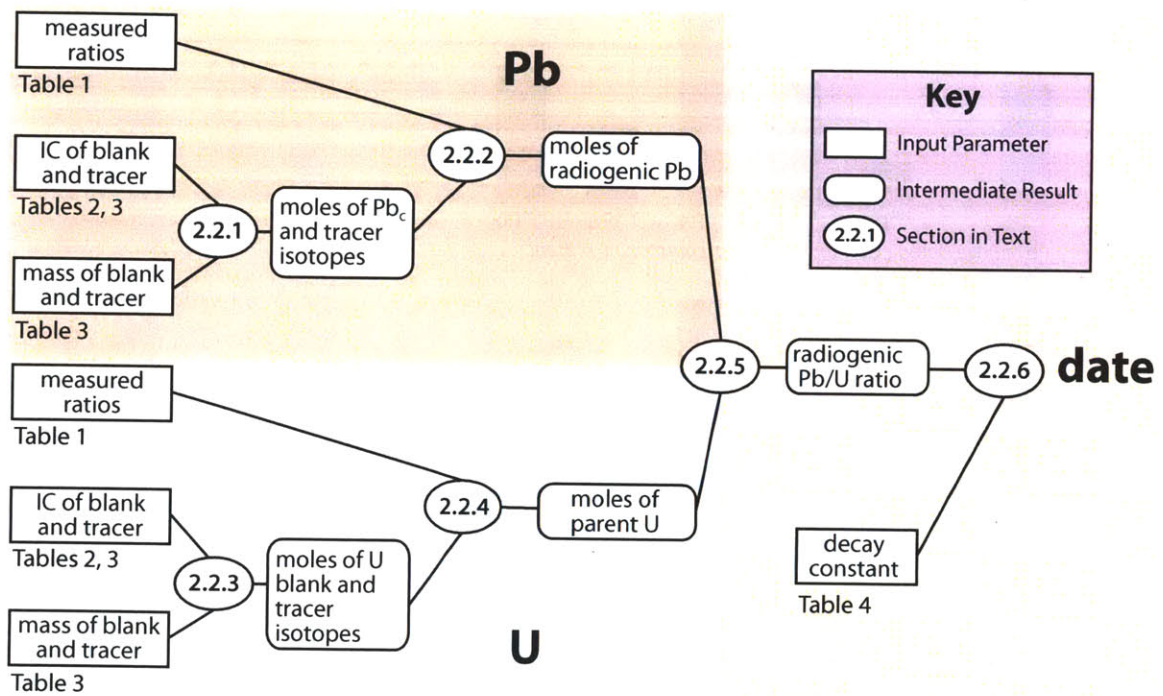


Figure 2-1: Flow chart for U-Pb data reduction

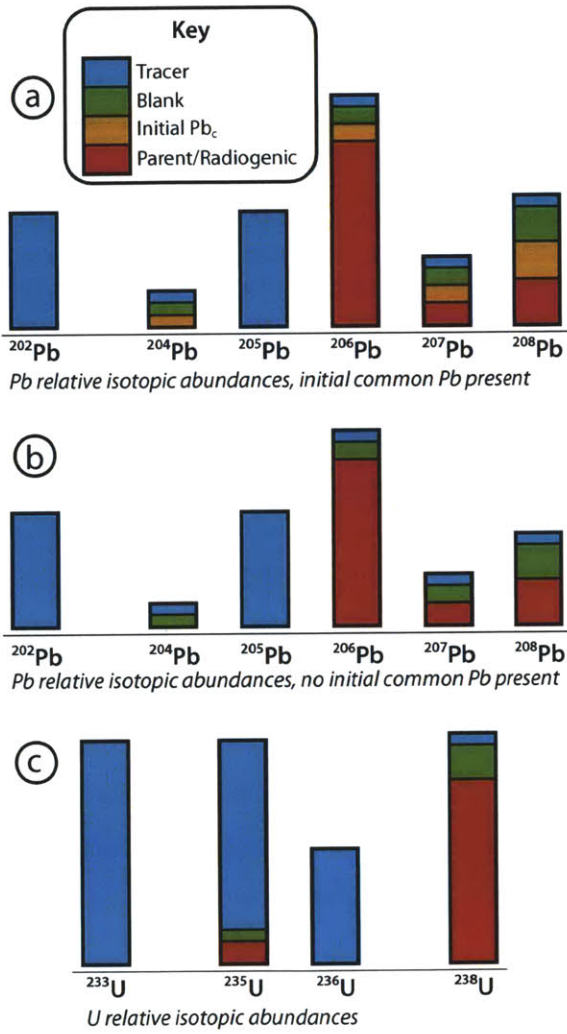


Figure 2-2: U-Pb sample components

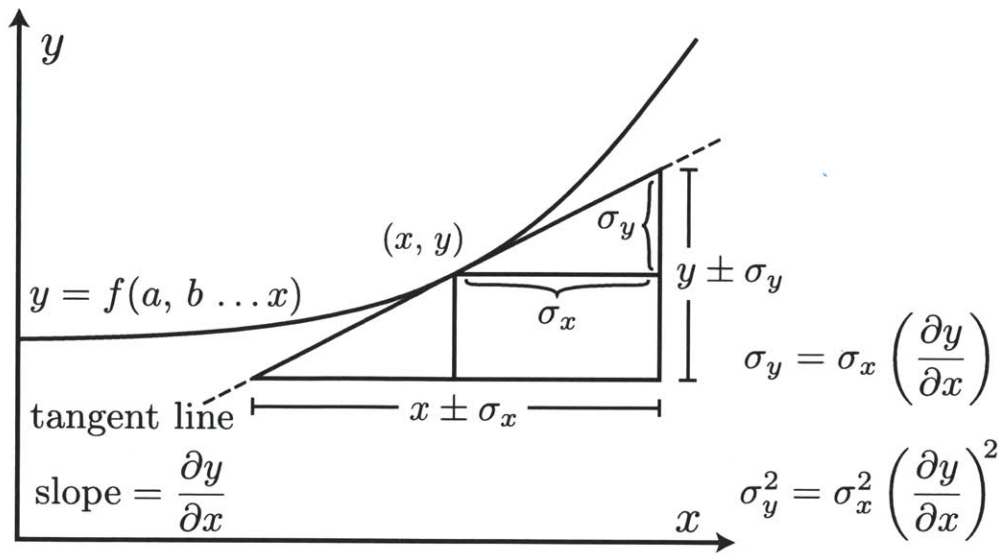


Figure 2-3: Uncertainty propagation in one dimension

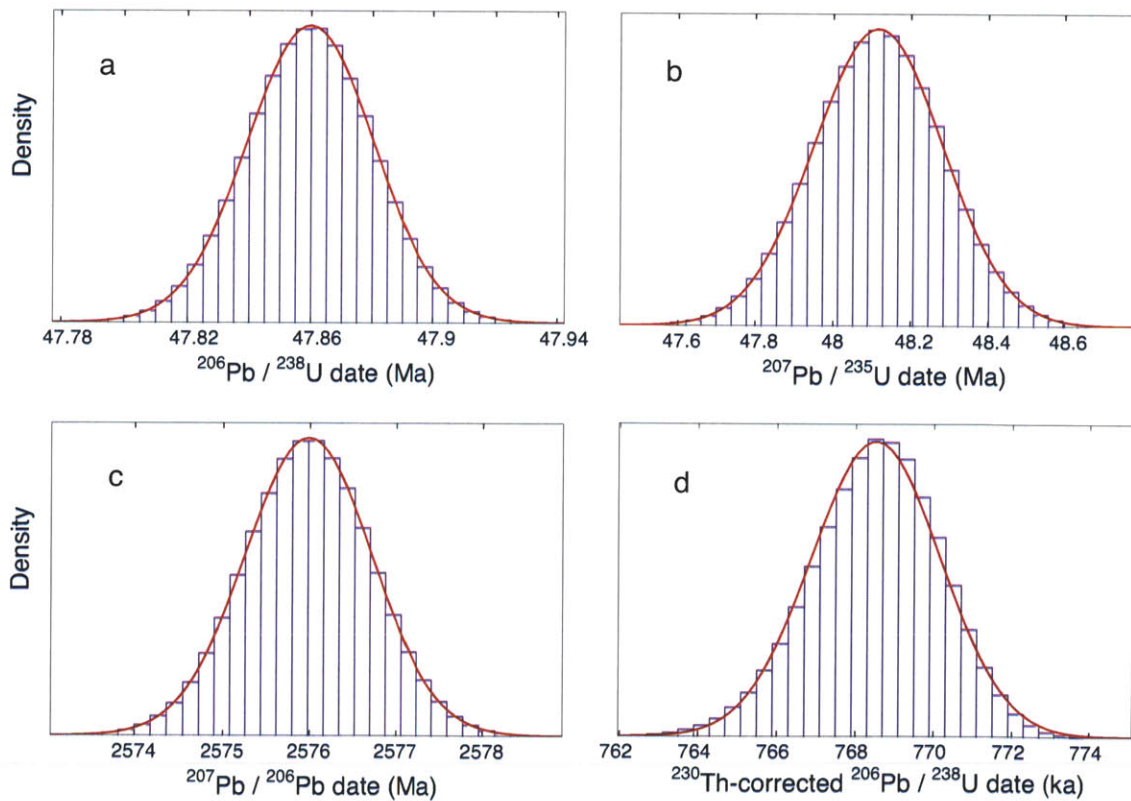


Figure 2-4: Monte Carlo simulation results

Chapter 3

Straight Line Regression through Data With Correlated Uncertainties in Two or More Dimensions

Abstract

Linear regression algorithms are used frequently for measured data that contain non-negligible uncertainties in each variable. For the general case of correlated measurement uncertainties between variables that differ from one analysis to the next, the popular algorithm of York (1968) calculates the maximum likelihood estimate for line parameters and their uncertainties. However, it considers only two-dimensional data and omits the uncertainty correlation between the slope and y-intercept, an important term for evaluating confidence intervals away from the origin. This contribution applies the maximum likelihood method to straight line regression through data in any number of dimensions to calculate a vector-valued slope and intercept as well as the covariance matrix that describes their uncertainties and uncertainty correlations. The algorithm is applied to Pb data measured by TIMS with a silica

gel activator that define a fractionation line in a three dimensional log-ratio space. While the log-ratios of even mass number Pb isotopes follow the slope predicted by mass-dependent fractionation with a Rayleigh or exponential law within calculated uncertainties, the log-ratio containing the odd mass number isotope ^{207}Pb diverges significantly, exhibiting mass-independent fractionation. The straight line regression algorithm is appropriate for fractionation lines that form linear trends in log-ratio space, but not for isochrons or mixing lines, which are predicted to be linear only when plotted as isotope or compositional ratios.

3.1 Introduction

It is not possible to measure a physical quantity with perfect accuracy and infinite precision. To estimate the degree to which the analysis corresponds to its true value, analysts assign uncertainties to the data, usually based on the variability of repeated measurements. Each repeated measurement often consists of multiple variables, like elemental or isotope ratios. The number of variables defines the dimension of the dataset, so that three variables can be plotted in a three-dimensional space, and so on. A series of repeated measurements of the same physical quantity, like the isotopic composition of a sample, can then be summarized by the mean of the repeated measurements and by their covariance matrix, which describes the uncertainty in each of the measured variables and the uncertainty correlations between them.

When multiple analyses fall on a line or plane in any number of dimensions, they can be described by a linear model $AX = B$, where A and B are predictor and response variables respectively, and elements of X are the model parameters, such as the slope and y-intercept. To calculate the best fit parameters, the definition of ‘best’ determines the regression technique used. The most familiar, ordinary least squares (OLS) in two dimensions, assumes that a noisy response variable, usually plotted on the y -axis, is a linear function of a predictor variable, usually plotted on the x -axis, which is not assigned uncertainty. The OLS algorithm can be extended to any number of dimensions, for instance determining the best fit plane to three

variables. OLS minimizes the squares of the (vertical) distances from the measured data points to the regression line or plane, where this distance is measured on the uncertain response variable only. Since it ignores any uncertainty in the predictor variable, OLS is not an appropriate regression algorithm for data with non-negligible measurement uncertainties in all measured variables.

Another least squares approach, termed total least squares (TLS, Golub, 1973; Van Huffel and Markovsky, 1991), and also known as orthogonal regression, Deming regression, or reduced major axis regression (Sokal and Rohlf, 1995), minimizes the perpendicular distance between each point and the regression line or plane. While this model incorporates uncertainty in all variables, its simplest formulation assumes the uncertainties, for instance in both the x - and y - directions, are the same magnitude. Additionally, conventional TLS assumes the data are homoscedastic, or that each analysis has the same covariance matrix. For most applications in geo- and cosmochemistry, these assumptions do not hold: the variables plotted on each axis have different uncertainties that are often correlated, such as when the same isotope appears in the denominator of each isotope ratio, or all variables plotted are subject to the same correction. Separate analyses are frequently independent of one another but have different uncertainties, depending for instance on ion beam intensity, and thus are heteroscedastic.

In order to fit heteroscedastic data with correlated uncertainties, more sophisticated algorithms weight the influence of each measurement according to its uncertainty. For instance, a weighted OLS algorithm divides each squared (vertical) distance by its variance, then minimizes the sum of the resulting ratios. Weighted or generalized TLS approaches, (e.g., Van Huffel and Vandewalle, 1989; Markovsky and Van Huffel, 2007), treat correlated uncertainties in both response variables and regressor variables, but not uncertainty correlations between them.

However, a variant termed elementwise-weighted total least squares (EW-TLS) solves the general regression case for multiple measurements of any linear system with heteroscedastic independent data points that have unique covariance matrices (Kukush and Van Huffel, 2004; Markovsky et al., 2006). When the uncertainties are

assumed to be normally distributed, EW-TLS yields the maximum likelihood estimate (MLE) of the model parameters (Markovsky et al., 2006), meaning that the best fit parameters maximize a likelihood function that considers all the measured data, their uncertainties, and the normally-distributed measurement model, explained in detail in Section 3.2. Likewise, the general MLE of Sohn and Menke (2002) to linear and non-linear regression models for correlated data additionally allow for uncertainty correlations between analyses. The highly cited York (1968) algorithm is a special case of EW-TLS, calculating the MLE of the slope and y-intercept for a line in two dimensions, as well as their uncertainties.

This contribution focuses on a more general scenario than that of York (1968): a straight line (one-dimensional) fit to heteroscedastic data with correlated, approximately normally distributed uncertainties for two or more variables. Recently published applications include, but are not limited to, kinetic isotope fractionation lines (Bizzarro et al., 2011; Zhang et al., 2011), trace element partitioning data (Balta et al., 2011), and multiple isotope system plots, e.g. ϵ_{Hf} vs. ϵ_{Nd} in Vervoort et al. (2011). Although many two-component mixing lines, such as common Pb in $^{206}\text{Pb}/^{204}\text{Pb}$ - $^{207}\text{Pb}/^{204}\text{Pb}$ - $^{208}\text{Pb}/^{204}\text{Pb}$ space and isochrons, for instance in $^{207}\text{Pb}/^{206}\text{Pb}$ - $^{204}\text{Pb}/^{206}\text{Pb}$ coordinates, create linear arrays of data, they are not suitable for linear regression because they contain ratios of major compositional components. This caveat is explored in Section 3.5.

Because the EW-TLS algorithm is a general case of the straight line model presented here, its previously derived statistical properties, such as convergence of the estimated fit parameters in probability to the true fit parameters as the number of measurements approaches infinity (Kukush and Van Huffel, 2004), apply here as well. However, by restricting the focus from multi-dimensional fit surfaces to a straight line, the resulting algorithm may be simplified and its solution optimized. For instance, terms involving the singular value or Cholesky decomposition of the inverse covariance matrix in (Markovsky et al., 2006) divide out in equation (3.12), precluding costly linear algebra.

The solution presented here, set in terms of the parametric equation for a line

$\mathbf{p} = \mathbf{a} + \mathbf{v}t$ instead of its linear algebra $AX \approx B$ equivalent, is also easier to pose in terms of the parameters of interest. This is demonstrated in the example application to kinetic isotope fractionation lines in Section 3.4. The parametric equation for a line is also directly analogous to established methods of compositional data analysis (Egozcue et al., 2003).

3.2 Estimation of Regression Parameters

The general case of straight line regression involves determining the best fit line through n measured data points \mathbf{p}_i , ($i = 1 \dots n$), in k dimensions, where each measured datum has a unique covariance matrix Σ_i . In this model, each \mathbf{p}_i is a $k \times 1$ column vector for a single measurement that contains the value of each variable measured. Σ_i is its $k \times k$ covariance matrix, with variance terms for each variable on the diagonal and covariance terms that describe the uncertainty correlations between the variables on the off diagonals. The best fit line through the data can be expressed in terms of a direction vector, \mathbf{v} , and an arbitrary point on the line, \mathbf{a} , which form the parametric expression for a line, $\mathbf{a} + \mathbf{v}t$. This algorithm solves for the maximum likelihood estimates of \mathbf{a} and \mathbf{v} , which are both $k \times 1$ column vectors, as well as their uncertainties and uncertainty correlations. Fig. 3-1 illustrates the straight line regression problem for $k = 3$ dimensions.

3.2.1 Vector from a Point to a Line

Every regression algorithm depends on determining the difference, known as a residual, between a measured data point and the best fit line. To calculate the residual, first translating both the line and all measured points by $-\mathbf{a}$ simplifies the expression for the regression line. The new location of measured data point i is $(\mathbf{p}_i - \mathbf{a})$, and points on the line can now be expressed simply as $\mathbf{v}t$. Next, the perpendicular projection $\hat{\mathbf{p}}_i$ of each translated point onto the line is

$$\hat{\mathbf{p}}_i = \frac{\mathbf{v} \mathbf{v}^T}{\mathbf{v}^T \mathbf{v}} (\mathbf{p}_i - \mathbf{a}) \quad (3.1)$$

where \top denotes the transpose. Note that $\hat{\mathbf{p}}_i$ is in the translated coordinate system, so that $\hat{\mathbf{p}}_i + \mathbf{a}$ is the point's projection in the original coordinate system. The residual vector \mathbf{r}_i , or the misfit between the measured data point and its projection $\hat{\mathbf{p}}_i$, is

$$\mathbf{r}_i = (\mathbf{p}_i - \mathbf{a}) - \hat{\mathbf{p}}_i = (\mathbf{p}_i - \mathbf{a}) - \frac{\mathbf{v} \mathbf{v}^\top}{\mathbf{v}^\top \mathbf{v}} (\mathbf{p}_i - \mathbf{a}) \quad (3.2)$$

Because it is a vector difference, equation (3.2) does not depend on the reference frame. The magnitude of \mathbf{r}_i represents the shortest Euclidean distance from the measured point to the best fit line. However, this distance does not consider the measured data uncertainties, embodied in the covariance matrices Σ_i , and so does not necessarily represent the best reconciliation of the model line and the data. Likewise, when the data in any of the k axes are expressed in different units (e.g. meters and seconds), then this distance contains terms from each unit, mixing apples and oranges. The solution presented below, known as statistical normalization, can be used to construct probability distribution and likelihood functions for the measured data and line fit parameters.

3.2.2 Maximum Likelihood and the Minimum Distance

The uncertainty in the measurement of the point \mathbf{p}_i is quantified with its covariance matrix Σ_i , which contains variances along its diagonal and covariances as off-diagonal elements. The shape of this uncertainty, the probability density function describes the relative probability that the true value of a measurement is in the vicinity of a point \mathbf{x} . Here, \mathbf{x} represents an arbitrary position, expressed as a $k \times 1$ column vector. If the data are normally distributed, the multivariate probability density function at any point \mathbf{x} in the vicinity of the measurement \mathbf{p}_i with covariance matrix Σ_i can be expressed as

$$f(\mathbf{x} \mid \mathbf{p}_i, \Sigma_i) = \frac{1}{(2\pi)^{k/2} |\Sigma_i|^{1/2}} \exp\left(-\frac{1}{2}(\mathbf{x} - \mathbf{p}_i)^\top \Sigma_i^{-1} (\mathbf{x} - \mathbf{p}_i)\right) \quad (3.3)$$

where $||$ is the matrix determinant and Σ^{-1} is the inverse of the covariance matrix. For a normally distributed univariate measurement ($k = 1$), the probability distribution function takes the shape of the well known ‘bell curve’.

In any number of dimensions, a surface of constant probability density around the point \mathbf{p}_i is the locus of all points \mathbf{x} that satisfy

$$(\mathbf{x} - \mathbf{p}_i)^\top \Sigma^{-1} (\mathbf{x} - \mathbf{p}_i) = c^2, \quad (3.4)$$

the exponential term in equation (3.3). The variable c in equation (3.4) is known as the Mahalanobis distance, and is analogous to the distance, in standard deviations, from \mathbf{p} to \mathbf{x} . In one dimension, the endpoints of a 1σ confidence interval have $c = 1$; in two dimensions, the ellipse with $c = 1$ is the 1σ uncertainty ellipse.

In Fig. 3-2a, the perpendicular projection from the measured point to the line $\mathbf{a} + \mathbf{v}t$ is not the best estimate of where the point actually falls on the line: in this case, the perpendicular vector intersects the line outside the 1σ uncertainty ellipse, but the line extends inside the ellipse elsewhere. The concept of orthogonal projection outlined above can be used only in the space where the Mahalanobis distance in equation (3.4) is the same as the Euclidean distance d , where

$$d^2 = (\mathbf{x} - \mathbf{p}_i)^\top (\mathbf{x} - \mathbf{p}_i). \quad (3.5)$$

In a space where the Euclidean and Mahalanobis distances agree, the covariance matrix and its inverse in equation (3.4) are both the identity matrix \mathbf{I} , whose uncertainty ellipse is the circle (Fig. 3-2b), or a sphere or its higher-dimensional analog. The linear transform that maps the inverse covariance matrix to the identity matrix is given by \mathbf{U} , the upper triangular matrix produced by Cholesky decomposition of the inverse covariance matrix:

$$\Sigma^{-1} = \mathbf{U}^\top \mathbf{U} \quad (3.6)$$

where \mathbf{U} has dimensions $k \times k$. Manipulating equation (3.6), it can be shown that the inverse covariance matrix becomes the identity matrix after a linear transformation

\mathbf{U} ,

$$\mathbf{U}\boldsymbol{\Sigma}\mathbf{U}^\top = \mathbf{I}. \quad (3.7)$$

For a given measurement vector \mathbf{p} and line parameters \mathbf{a} and \mathbf{v} , the linear transformation is applied by premultiplying each column vector by \mathbf{U} . The residual vector in equation (3.2) becomes

$$\mathbf{U}\mathbf{r} = \mathbf{U}(\mathbf{p} - \mathbf{a}) - \mathbf{U}\hat{\mathbf{p}} = \mathbf{U}(\mathbf{p} - \mathbf{a}) - \frac{\mathbf{U}\mathbf{v}(\mathbf{U}\mathbf{v})^\top}{(\mathbf{U}\mathbf{v})^\top\mathbf{U}\mathbf{v}} \mathbf{U}(\mathbf{p} - \mathbf{a}) \quad (3.8)$$

and the squared Mahalanobis distance is the inner product of the residual with itself:

$$\|\mathbf{U}\mathbf{r}\|^2 = \left[\mathbf{U}(\mathbf{p} - \mathbf{a}) - \frac{\mathbf{U}\mathbf{v}(\mathbf{U}\mathbf{v})^\top}{(\mathbf{U}\mathbf{v})^\top\mathbf{U}\mathbf{v}} \mathbf{U}(\mathbf{p} - \mathbf{a}) \right]^\top \left[\mathbf{U}(\mathbf{p} - \mathbf{a}) - \frac{\mathbf{U}\mathbf{v}(\mathbf{U}\mathbf{v})^\top}{(\mathbf{U}\mathbf{v})^\top\mathbf{U}\mathbf{v}} \mathbf{U}(\mathbf{p} - \mathbf{a}) \right] \quad (3.9)$$

Equations (3.10) through (3.13) simplify this cumbersome expression. Factoring out a \mathbf{U} from each term above and simplifying $(\mathbf{U}\mathbf{v})^\top$ to $\mathbf{v}^\top\mathbf{U}^\top$ yields

$$\|\mathbf{U}\mathbf{r}\|^2 = \left[\mathbf{U} \left((\mathbf{p} - \mathbf{a}) - \frac{\mathbf{v}\mathbf{v}^\top\mathbf{U}^\top}{\mathbf{v}^\top\mathbf{U}^\top\mathbf{U}\mathbf{v}} \mathbf{U}(\mathbf{p} - \mathbf{a}) \right) \right]^\top \left[\mathbf{U} \left((\mathbf{p} - \mathbf{a}) - \frac{\mathbf{v}\mathbf{v}^\top\mathbf{U}^\top}{\mathbf{v}^\top\mathbf{U}^\top\mathbf{U}\mathbf{v}} \mathbf{U}(\mathbf{p} - \mathbf{a}) \right) \right] \quad (3.10)$$

Transposing the two terms in brackets in the first term of equation (3.10) yields

$$\|\mathbf{U}\mathbf{r}\|^2 = \left((\mathbf{p} - \mathbf{a}) - \frac{\mathbf{v}\mathbf{v}^\top\mathbf{U}^\top}{\mathbf{v}^\top\mathbf{U}^\top\mathbf{U}\mathbf{v}} \mathbf{U}(\mathbf{p} - \mathbf{a}) \right)^\top \mathbf{U}^\top\mathbf{U} \left((\mathbf{p} - \mathbf{a}) - \frac{\mathbf{v}\mathbf{v}^\top\mathbf{U}^\top}{\mathbf{v}^\top\mathbf{U}^\top\mathbf{U}\mathbf{v}} \mathbf{U}(\mathbf{p} - \mathbf{a}) \right) \quad (3.11)$$

Substituting $\boldsymbol{\Sigma}^{-1} = \mathbf{U}^\top\mathbf{U}$ from the definition of the Cholesky decomposition in equation (3.6) yields

$$\|\mathbf{U}\mathbf{r}\|^2 = \left((\mathbf{p} - \mathbf{a}) - \frac{\mathbf{v}\mathbf{v}^\top\boldsymbol{\Sigma}^{-1}}{\mathbf{v}^\top\boldsymbol{\Sigma}^{-1}\mathbf{v}} (\mathbf{p} - \mathbf{a}) \right)^\top \boldsymbol{\Sigma}^{-1} \left((\mathbf{p} - \mathbf{a}) - \frac{\mathbf{v}\mathbf{v}^\top\boldsymbol{\Sigma}^{-1}}{\mathbf{v}^\top\boldsymbol{\Sigma}^{-1}\mathbf{v}} (\mathbf{p} - \mathbf{a}) \right) \quad (3.12)$$

In this way, the upper Cholesky decomposition matrices factor out, precluding the need to calculate them. Finally, multiplying out the terms in parentheses and factoring yields a simplified expression for the squared Mahalanobis distance from the

measured point to the best fit line

$$\|\mathbf{U}_r\|^2 = (\mathbf{p} - \mathbf{a})^\top \boldsymbol{\Sigma}^{-1} (\mathbf{p} - \mathbf{a}) - \frac{(\mathbf{v}^\top \boldsymbol{\Sigma}^{-1} (\mathbf{p} - \mathbf{a}))^2}{\mathbf{v}^\top \boldsymbol{\Sigma}^{-1} \mathbf{v}} \quad (3.13)$$

The sum of the expression for the squared Mahalanobis distance in equation (3.13) over all measured data points \mathbf{p}_i , ($i = 1 \dots n$) represents the ‘sum of squares’ to be minimized.

3.2.3 Probability Density and Likelihood Functions

To prove that minimizing the sum of the squares generates the maximum likelihood estimate for the line parameters, the expression in equation (3.13) can be used to build a probability density function for the each measurement, analogous to equation (3.3). The function

$$f(\mathbf{p}_i | \mathbf{a}, \mathbf{v}) = \frac{1}{(2\pi)^{k/2} |\boldsymbol{\Sigma}_i|^{1/2}} \exp\left(-\frac{1}{2} \left[(\mathbf{p}_i - \mathbf{a})^\top \boldsymbol{\Sigma}_i^{-1} (\mathbf{p}_i - \mathbf{a}) - \frac{(\mathbf{v}^\top \boldsymbol{\Sigma}_i^{-1} (\mathbf{p}_i - \mathbf{a}))^2}{\mathbf{v}^\top \boldsymbol{\Sigma}_i^{-1} \mathbf{v}} \right]\right) \quad (3.14)$$

describes the probability that a point in the vicinity of \mathbf{p}_i belongs to the line $\mathbf{a} + \mathbf{v}t$.

Given a dataset of n independent measurements $\mathbf{P} = (\mathbf{p}_1, \mathbf{p}_2, \dots, \mathbf{p}_n)$ of the linear array $\mathbf{a} + \mathbf{v}t$, the joint density function $f(\mathbf{p}_1, \mathbf{p}_2, \dots, \mathbf{p}_n | \mathbf{a}, \mathbf{v}) = f(\mathbf{p}_1 | \mathbf{a}, \mathbf{v}) \cdot f(\mathbf{p}_2 | \mathbf{a}, \mathbf{v}) \cdot \dots \cdot f(\mathbf{p}_n | \mathbf{a}, \mathbf{v})$ defines the probability function of the entire measured dataset \mathbf{P} given any line parameters \mathbf{a} and \mathbf{v} . Since the measured data is fixed, we are instead interested in the likelihood function of the regression parameters given the measured data $\mathcal{L}(\mathbf{a}, \mathbf{v} | \mathbf{P})$, which is equal to the joint probability density function above:

$$\mathcal{L}(\mathbf{a}, \mathbf{v} | \mathbf{P}) = f(\mathbf{P} | \mathbf{a}, \mathbf{v}) = \prod_{i=1}^n f(\mathbf{p}_i | \mathbf{a}, \mathbf{v}) \quad (3.15)$$

Although the large product is not easily manipulated or differentiated, taking the natural logarithm converts the product of exponentials to a sum:

$$\ln \mathcal{L}(\mathbf{a}, \mathbf{v} | \mathbf{P}) = \sum_{i=1}^n \ln f(\mathbf{p}_i | \mathbf{a}, \mathbf{v}) \quad (3.16)$$

To avoid confusion with the traditional covariance matrix notation Σ , all summation symbols will include their upper and lower limits explicitly, as above.

3.3 Solving for the Best Fit Line

The best fit line maximizes the likelihood function $\mathcal{L}(\mathbf{a}, \mathbf{v} | \mathbf{P})$ of the regression parameters \mathbf{a} and \mathbf{v} given the measured data points \mathbf{P} . Taking the natural logarithm of the likelihood function is a monotone transformation, so that maximizing the log-likelihood $\ln \mathcal{L}(\mathbf{a}, \mathbf{v} | \mathbf{P})$ simultaneously maximizes the likelihood function itself. Substituting the probability density function for a point \mathbf{p}_i on the line $\mathbf{a} + \mathbf{v}t$ in equation (3.14) into the likelihood function in equation (3.16) yields

$$\ln \mathcal{L}(\mathbf{a}, \mathbf{v} | \mathbf{P}) = -\frac{1}{2} \sum_{i=1}^n \left[(\mathbf{p}_i - \mathbf{a})^\top \Sigma_i^{-1} (\mathbf{p}_i - \mathbf{a}) - \frac{(\mathbf{v}^\top \Sigma_i^{-1} (\mathbf{p}_i - \mathbf{a}))^2}{\mathbf{v}^\top \Sigma_i^{-1} \mathbf{v}} \right] + \ln |\Sigma_i| + k \ln(2\pi) \quad (3.17)$$

where $|\Sigma_i|$ is the determinant of the measured covariance matrix.

The maximum likelihood estimate of the line parameters \mathbf{a} and \mathbf{v} for the line $\mathbf{a} + \mathbf{v}t$ maximizes the log-likelihood equation. This maximum occurs where the derivatives of equation (3.17) with respect to \mathbf{a} and \mathbf{v} are equal to zero. Differentiating yields a system of $2k$ equations, with the elements of \mathbf{a} and \mathbf{v} as $2k$ unknowns:

$$\frac{\partial \ln \mathcal{L}}{\partial \mathbf{a}} = \sum_{i=1}^n \frac{(\mathbf{p}_i - \mathbf{a})^\top (\Sigma_i^{-1} - \Sigma_i^{-1} \mathbf{v} \mathbf{v}^\top \Sigma_i^{-1})}{\mathbf{v}^\top \Sigma_i^{-1} \mathbf{v}} = \mathbf{0} \quad (3.18)$$

$$\frac{\partial \ln \mathcal{L}}{\partial \mathbf{v}} = \sum_{i=1}^n \frac{\mathbf{v}^\top \Sigma_i^{-1} \mathbf{v} \mathbf{v}^\top \Sigma_i^{-1} (\mathbf{p}_i - \mathbf{a}) \Sigma_i^{-1} (\mathbf{p}_i - \mathbf{a}) - (\mathbf{v}^\top \Sigma_i^{-1} (\mathbf{p}_i - \mathbf{a}))^2 \Sigma_i^{-1} \mathbf{v}}{(\mathbf{v}^\top \Sigma_i^{-1} \mathbf{v})^2} = \mathbf{0} \quad (3.19)$$

where $\mathbf{0}$ is a vector of zeros with length k .

Although the system of equations (3.18) and (3.19) contains $2k$ equations with $2k$ unknowns, the same line may be defined by any point \mathbf{a} on the line and a direction vector \mathbf{v} of any length. Thus the above system has an infinite number of solutions. A unique solution may be reached by setting the first component of \mathbf{a} to zero, the

multi-dimensional analogue of a y-intercept, and setting the first component of \mathbf{v} to one, the multi-dimensional analogue of the slope. With these substitutions, the above $2k$ equations in $2(k - 1)$ variables will have a unique solution at a best fit $\bar{\mathbf{a}}$ and $\bar{\mathbf{v}}$. The solution may be reached quickly with a non-linear equation solver included in common mathematical software packages such as MATLAB.

However, for datasets that are far from the origin, setting a component of \mathbf{a} to zero will result in a poorly conditioned covariance matrices for the line fit parameters, with highly correlated uncertainties between the components of \mathbf{a} and \mathbf{v} . Numerical stability is improved by instead setting any one \mathbf{a} component to its value in the multivariate weighed mean of the measured data \mathbf{P} . The weighted mean, presented in 3.8 is also an excellent initial estimate for \mathbf{a} in the numerical solution of equations (3.18) and (3.19).

3.3.1 Uncertainty in Fit Parameters

The uncertainty in the best fit line parameters $\bar{\mathbf{a}}$ and $\bar{\mathbf{v}}$ are estimated by calculating the Fisher Information Matrix, \mathcal{I} , the negative second derivative of the likelihood function with respect to the best fit parameters. \mathcal{I} takes the form

$$\mathcal{I} = - \begin{bmatrix} \frac{\partial^2 \ln \mathcal{L}}{\partial \bar{\mathbf{a}} \bar{\mathbf{a}}^T} & \frac{\partial^2 \ln \mathcal{L}}{\partial \bar{\mathbf{a}} \bar{\mathbf{v}}^T} \\ \frac{\partial^2 \ln \mathcal{L}}{\partial \bar{\mathbf{v}} \bar{\mathbf{a}}^T} & \frac{\partial^2 \ln \mathcal{L}}{\partial \bar{\mathbf{v}} \bar{\mathbf{v}}^T} \end{bmatrix} \quad (3.20)$$

Because the first components of vectors $\bar{\mathbf{a}}$ and $\bar{\mathbf{v}}$ have been specified explicitly, these components have zero uncertainty. For other the $k - 1$ components of each vector, as well as the covariances between them, the covariance matrix $\Sigma_{\mathbf{av}}$ is calculated by removing the rows and columns 1 and $k + 1$ corresponding to the specified components, generating a $2(k - 1) \times 2(k - 1)$ matrix, then calculating the matrix inverse of the shortened Fisher information matrix,

$$\Sigma_{\mathbf{av}} = \mathcal{I}_r^{-1} \quad (3.21)$$

where \mathcal{I}_r is \mathcal{I} with the appropriate rows and columns removed. The same result is reached by calculating the pseudoinverse of \mathcal{I} with the rows and columns corresponding to the specified components set to zero. The second derivatives in equation (3.20) are included in 3.7.

To determine whether the uncertainties in the fit parameters are valid, or if the straight line model is reasonable for the observed data, a statistical goodness of fit test is required. The reduced chi-square (χ_{red}^2), known in the geochronology community as the MSWD or mean squared weighted deviation (Wendt and Carl, 1991), relates the average ratio of the squared offset between the measurement and the model to its variance, or expected value:

$$\chi_{red}^2 = \frac{1}{df} \sum_{i=1}^n \frac{(meas. - model)^2}{\sigma_{meas.}^2} \quad (3.22)$$

The expression inside the summation of equation (3.22) is analogous to equation (3.13), the squared distance from the measured point to the line weighted by its inverse covariance matrix. A line fit in any number of dimensions has $df = (k - 1)(n - 2)$ degrees of freedom, where $k - 1$ represents the number of independent directions the measurement can deviate from the straight line and $n - 2$ is the number of vector-valued measurements minus the two line fit parameters \mathbf{a} and \mathbf{v} . Thus,

$$\chi_{red}^2 = \frac{1}{(k - 1)(n - 2)} \sum_{i=1}^n \left[(\mathbf{p}_i - \mathbf{a})^\top \boldsymbol{\Sigma}_i^{-1} (\mathbf{p}_i - \mathbf{a}) - \frac{(\mathbf{v}^\top \boldsymbol{\Sigma}_i^{-1} (\mathbf{p}_i - \mathbf{a}))^2}{\mathbf{v}^\top \boldsymbol{\Sigma}_i^{-1} \mathbf{v}} \right] \quad (3.23)$$

The expected value of χ_{red}^2 is 1, with a probability density function that approaches a normal distribution with increasing degrees of freedom that has a standard deviation of $(2/df)^{1/2}$ (Wendt and Carl, 1991).

3.3.2 Other Linear Regression Algorithms

The solutions to equations (3.18) and (3.19) and the covariance matrix calculated with equation (3.21) can be shown to reduce to the two special cases of uncertainty-weighted line fitting currently used by the geochemistry and geochronology commu-

nities. A detailed history of parametric regression algorithms in earth sciences can be found in Howarth (2001).

In a series of related papers, York (1966, 1968) and York et al. (2004) offer incrementally improved algorithms for straight-line fitting in two dimensions by iteratively solving simultaneously for the MLE line parameters and uncertainties. Crucially, the objective equation presented here in equation (3.13) with $k = 2$ and $\mathbf{a}_1 = 0$, $\mathbf{v}_1 = 1$ simplifies to Equation 2 of York (1968). The linear regression algorithm of Sohn and Menke (2002), which is generalizable to higher dimensions, is also equivalent to the MLE presented here.

Although the algorithm presented here and those in York (1968), York et al. (2004), and Sohn and Menke (2002) converge to the same solution for the line fit parameters, equations (3.18) and (3.19) above can be solved without determining the line parameter uncertainties at the same time, which are here given explicitly using these best fit line parameters in 3.7. Divorcing the uncertainty calculation proffers flexibility and faster convergence when using this fitting procedure as part of a larger, more computationally intensive algorithm or with very large data sets, such as the one presented in Section 3.4. Note that the York (1968) paper additionally omits the covariance term between the uncertainties in the slope and y-intercept, although this is corrected in (York et al., 2004). This term becomes important when constructing confidence intervals for the regression line when the measured data is far from the origin.

The maximum likelihood method used here is also employed by Titterton and Halliday (1979) for two-dimensional linear regression through data with correlated uncertainties. The equations for the first and second derivatives of the likelihood equations in the Titterton and Halliday (1979) appendix are special cases of equations (3.18), (3.19) and 3.7. York et al. (2004) show that the expressions for the uncertainties in the fit parameters for both the least-squares and MLE approach are equivalent.

The other multi-dimensional line fit commonly used in geochronology are for three-dimensional linear arrays, first described for $^{230}\text{Th}/\text{U}$ isochrons in Ludwig and Tit-

terington (1994) and utilized again for ‘Total Pb/U Isochrons’ in Ludwig (1998b). In the explicitly MLE-motivated former publication, the first (unnumbered) equation in the Appendix is equivalent to equation (3.17) for $k = 3$ and $\mathbf{a}_1 = 0$, $\mathbf{v}_1 = 1$, and the second partial derivatives given later are equivalent to the general case given here in 3.7. In the latter publication, Equation 33 is a special case of equation (3.13) above with the same constraints. Note the matrix form of the second partial derivatives given in 3.7 avoid the rapidly rising number of partial derivative terms required when computing the partial derivatives separately for each line parameter. For instance, 18 separate partial second derivatives are not needed for $k = 4$, 32 for $k = 5$, and so on.

3.4 Application to Kinetic Isotope Fractionation

Kinetic isotope fractionation between isotopologues, or isotopic molecules, occurs when a chemical reaction occurs irreversibly with different rate constants for each isotopologue (Young et al., 2002). The rate constants depend in large part on the effective masses of the isotopologues, and are often assumed proportional to the inverse square root of their effective mass (Bigeleisen, 1949; Young et al., 2002). In the case of evaporation of Pb from a hot filament in a thermal ionization mass spectrometer (TIMS), the reaction product Pb is instantaneously removed by ionization and acceleration by the mass spectrometer or by rapid pumping at high vacuum. Thus, in addition to an instantaneous fractionation due to the differing rate constants, there is a time-progressive depletion of the species with the faster rate constant (usually the lighter isotopologue), known as a reservoir effect. The two assumptions, that the ratio of the reaction constants depend on the inverse square root of the mass but not on time or temperature, and that Pb evaporated from the filament is instantaneously removed, generate a differential equation that relates the quantity of sample consumed to the isotopic composition of the instantaneous reaction products, which are analyzed by TIMS when ionized. The solution to this differential equation is known as the ‘Rayleigh law’ (Russell et al., 1978; Habfast, 1998).

3.4.1 Rayleigh and Exponential Fractionation Equations

The Rayleigh law for two isotopes a and b with masses M_a and M_b is

$$\left(\frac{a}{b}\right)_{meas} = \left(\frac{a}{b}\right)_{corr} \cdot \sqrt{\frac{M_b}{M_a}} \cdot \left(\frac{b}{b_0}\right)^{\sqrt{M_b/M_a} - 1} \quad (3.24)$$

where *corr* and *meas* denote true (fractionation-corrected) and measured isotope ratios, and (b/b_0) is the fraction of isotope b remaining on the filament.

Not all observations by TIMS of fractionating samples follow the predictions made by the Rayleigh law (e.g., Russell et al., 1978), and the progressive depletion model does not apply to a constantly refreshed reservoir, as for inductively-coupled plasma mass spectrometry (ICP-MS). A popular (e.g., Boyet and Carlson, 2006; Amelin et al., 2009) empirical law, which is also an approximate solution to the Rayleigh equation, is the exponential fractionation law (Russell et al., 1978; Habfast, 1998; Albarède et al., 2004). The exponential fractionation equation for the same scenario above is

$$\left(\frac{a}{b}\right)_{corr} = \left(\frac{a}{b}\right)_{meas} \cdot \left(\frac{M_b}{M_a}\right)^\beta \quad (3.25)$$

where β is the mass fractionation factor, which may change during the course of an analysis and vary between analyses.

For both fractionation laws, it is possible to derive a linear equation relating the fractionation-corrected log-ratio of isotopes to the measured log-ratio. For the Rayleigh law, taking the natural logarithm of both sides and rearranging terms yields

$$\ln\left(\frac{a}{b}\right)_{corr} = \ln\left(\frac{a}{b}\right)_{meas} - \frac{1}{2} \ln\frac{M_b}{M_a} - \left(\sqrt{\frac{M_b}{M_a}} - 1\right) \cdot \ln\left(\frac{b}{b_0}\right) \quad (3.26)$$

and for the exponential law,

$$\ln\left(\frac{a}{b}\right)_{corr} = \ln\left(\frac{a}{b}\right)_{meas} + \beta \ln\left(\frac{M_b}{M_a}\right) \quad (3.27)$$

Three-isotope systems whose fractionation is governed by either the Rayleigh or

exponential law (i.e. changing (b/b_0) or β) will generate linear arrays when plotted as $\ln(a/b)_{meas}$ vs. $\ln(c/b)_{meas}$. This relationship is often exploited to assess or correct the effects isotopic fractionation (Maréchal et al., 1999; Bizzarro et al., 2011). For the simpler exponential fractionation equation, the line can be expressed parametrically as passing through the log-ratio of the corrected isotopic composition (IC) $\langle \ln(c/b)_{corr}, \ln(a/b)_{corr} \rangle$ with a two-component direction vector $\langle \ln(M_b/M_c), \ln(M_b/M_a) \rangle$ and fractionation factor β , where $\langle \rangle$ denotes a transposed column vector. It follows that the log-ratio of the corrected IC is analogous to \mathbf{a} above, the direction vector, which depends on the ratios of the isotopic masses has its analog in \mathbf{v} , and β becomes the location parameter t .

For the Rayleigh law, a plot of $\ln(a/b)_{meas}$ vs. $\ln(c/b)_{meas}$ passes through the point $\langle \ln(c/b) + \frac{1}{2} \ln(M_b/M_c), \ln(a/b) + \frac{1}{2} \ln(M_b/M_a) \rangle$ with a direction vector $\langle \sqrt{M_b/M_c} - 1, \sqrt{M_b/M_a} - 1 \rangle$. Unlike the exponential law, the Rayleigh law does not predict that the observed fractionation line will go through the true IC of the sample, and the predicted slopes for the two are different. If the true IC is known to sufficient absolute precision, this property may be used to distinguish between the two laws. In the absence of a well-known standard IC, the difference in the predicted slopes provides a sensitive test for the applicability of each law.

The linear equations above may be scaled up to systems with any number of isotopes (e.g., Sr, Ti, Nd, Pb), producing straight lines in log-ratio space with dimension k equal to the number of isotopes present minus one. Isotopic fractionation behavior can be evaluated by calculating the means \mathbf{p}_i of log-ratios to a common isotope along with their covariance matrices $\mathbf{\Sigma}_i$, then fitting a straight line to the data. It is important to note that if \mathbf{p}_i and $\mathbf{\Sigma}_i$ are estimated from multiple measurements, then mean and covariance calculations must be performed *after* the log-ratios are evaluated. In other words, one must calculate the mean and covariance matrix of the log-ratios rather than the logarithm of the mean and covariance matrix of the measured ratios. Using a common compositional variable (e.g. an isotope abundance) as the denominator of log-ratios is the additive log-ratio transform (alr) of Aitchison (1986), a well-established analytical technique for compositional data discussed in

3.4.2 Application to Pb Measurements by TIMS

Precise isotope ratio measurements of Pb by TIMS are used for high precision geo- and cosmochemistry (Amelin et al., 2009; Davydov et al., 2010), geochemistry (Fekiacova et al., 2007; Abouchami et al., 2005), and isotope standard inter-calibration (Thirlwall, 2000; Doucelance and Manhès, 2001). To empirically evaluate isotopic fractionation of Pb during TIMS analysis, a large (~ 50 ng) sample of the standard NBS 982 (Catanzaro et al., 1968) was loaded with a silica gel activator (Gerstenberger and Haase, 1997) on a Re filament and run to exhaustion. The ion beams of ^{204}Pb , ^{205}Pb , ^{206}Pb , and ^{208}Pb were measured on a static Faraday array in 100-millisecond integrations, alternating between 40 seconds baseline measured at half-mass and 75 seconds on-peak. The entire run consists of 51000 on-peak and 27200 baseline integrations, provided in the electronic annex EA-1.

After correcting for baselines and propagating baseline uncertainties, the natural logarithms of the ^{204}Pb , ^{207}Pb , and ^{208}Pb intensity divided by the ^{206}Pb intensity were evaluated for each integration. The mean and covariance matrix of every 25 log-ratios were calculated for a total of $n = 2040$ \mathbf{p}_i and Σ_i , where each \mathbf{p} has the form $\langle \log(^{204}\text{Pb}/^{206}\text{Pb}), \log(^{207}\text{Pb}/^{206}\text{Pb}), \log(^{208}\text{Pb}/^{206}\text{Pb}) \rangle$. The short integration times and limited number of integrations per mean (2.5 seconds total per data point) attempts to separate the covariance due to random signal noise from the linear fractionation trend. The three-dimensional measured data, plotted as a pair of two-dimensional projections, is presented in Fig. 3-3.

The solution to the system of equations (3.18) and (3.19) was calculated with the commercial mathematical software MATLAB using the built-in ‘fsolve’ function, which employs the Levenberg-Marquardt algorithm (Levenberg, 1944; Marquardt, 1963). The MATLAB code is provided as electronic annex EA-2. For this calculation with $n = 2040$ means in $k = 3$ dimensions, the code takes ~ 20 seconds to compile on a 2.4 GHz laptop computer. The maximum likelihood estimate of the regression parameters \mathbf{a} and \mathbf{v} and their uncertainties are listed in Table 3.1 and the best fit line

is plotted in green in Fig. 3-3a, along with its 2σ uncertainty envelope in Fig. 3-3b.

For a straight line fit, one component of \mathbf{a} and \mathbf{v} must be explicitly specified, and the other components are calculated using these values. Here, the values of \mathbf{a}_3 and \mathbf{v}_3 were chosen to be 0.00016 and 1, respectively, so that \mathbf{a} corresponds to the point on the observed line with a $^{208}\text{Pb}/^{206}\text{Pb}$ of 1.00016 (Catanzaro et al., 1968) and the first two direction vector components are the slopes of the first two variables when plotted against the third. Thus the first and second components of \mathbf{a} and \mathbf{v} are conditional upon the explicitly specified value of the third component. Likewise, the covariance matrix $\Sigma_{\mathbf{a}\mathbf{v}}$ describes the conditional probability distribution of the unknown parameters, here \mathbf{a}_1 , \mathbf{a}_2 , \mathbf{v}_1 , and \mathbf{v}_2 , given $\mathbf{a}_3 = 0.00016$ and $\mathbf{v}_3 = 1$. Changing the specified values of \mathbf{a}_3 and \mathbf{v}_3 would change both the values and uncertainties of the new best fit line parameters, but not the location of the best fit line or its uncertainty envelope.

The reduced chi-square statistic (χ_{red}^2 , equation 3.23) for this linear fit is 1.197 for $(3 - 1)(2040 - 2) = 4076$ degrees of freedom. The predicted standard deviation of χ_{red}^2 is $(2/4076)^{1/2} \approx 0.022$, so that the observed χ_{red}^2 is significantly greater than its expected value of 1. Possible reasons for the elevated χ_{red}^2 include heavy-tailed non-Gaussian probability distributions for the measured data or non-linear evolution of the log-ratios, such as intermittent presence of isobaric interferences or subtly changing fractionation behavior with time. Although the latter possibilities are difficult to rule out, the former is altogether likely considering the dearth of detailed noise characterization of mass spectrometer measurements, especially at the 100 ms conversion rate of the analog-digital converter. In this case, the robust linear regression algorithm for $k = 2$ dimensions developed by Powell et al. (2002) could be adapted to a higher-dimensional straight line model, such as that given by Sohn and Menke (2002). Because the χ_{red}^2 is so close to unity, inflating the uncertainties by $\sqrt{1.197} = 1.094$ or using a robust regression technique will not change the conclusions that follow.

In the upper two plots of Fig. 3-3, which are projections of the data onto the $\log(^{204}\text{Pb}/^{206}\text{Pb})$ vs. $\log(^{208}\text{Pb}/^{206}\text{Pb})$ plane, the best fit line agrees with the predicted mass-dependent fractionation (MDF) line using both the exponential or Rayleigh laws (see also Table 3.1). However, the observed and mass-dependent fractionation lines

diverge significantly in the $\log(^{207}\text{Pb}/^{206}\text{Pb})$ vs. $\log(^{208}\text{Pb}/^{206}\text{Pb})$ projection.

The horizontal or vertical position of the mass-dependent fractionation line is uncertain for a NBS 982 Pb analysis: the absolute uncertainty of the IC is known to only to ca. 180 ppm (2σ) (Catanzaro et al., 1968), and the analysis itself necessarily includes a loading blank of uncertain mass and isotopic composition. Additionally, the sample was run as a static analysis, and no effort was made to cancel small differences in Faraday collector or amplifier efficiencies. None of these variables affect the predicted slope of the fractionation line, which depends on the masses of the isotopes alone (Albarede and Beard, 2004). Thus, the systematic difference in odd mass number ^{207}Pb behavior relative to the even masses can be reliably attributed to mass independent fraction (MIF) during the analysis.

MIF has been described in several heavy element isotopic systems, such as Cd, Hf, Hg, Tl, and U in laboratory and natural settings (see references in Epov et al., 2011), and may be the result of nuclear field shift (Bigeleisen, 1996) or nuclear spin (Buchachenko, 1995) effects. Both mechanisms predict systematic differences in the fractionation of odd isotopes over even ones, as observed here. The magnitude of the nuclear field shift effect is inversely proportional to the absolute temperature of the system, which is typically > 1400 K during TIMS analysis, implicating the nuclear spin effect. However, the reactions responsible for producing Pb^+ ions from a silica gel activator are complex (Kessinger et al., 2001), and no theoretical predictions yet exist for the magnitude of the nuclear field shift effect (e.g., Schauble, 2007).

For large (> 1 ng) Pb loads analyzed with a silica gel activator by TIMS, MIF or an ‘odd-even effect’ has been postulated by several authors, including Thirlwall (2000), Doucelance and Manhès (2001), and most recently by Amelin et al. (2005), who also incorporate a ^{202}Pb - ^{205}Pb tracer. In contrast to the data reported in these references, the magnitude of mass-independent fractionation observed here is constant during the course of the analysis, reflected by the linear fractionation trend. Thus the fractionation correction equations for log-ratios need not be abandoned, and may

be amended with an additional term of the form

$$\ln\left(\frac{a}{b}\right)_{corr} = \ln\left(\frac{a}{b}\right)_{meas} + \beta \left[\ln\left(\frac{M_b}{M_a}\right) + \ln\left(\frac{\gamma_b}{\gamma_a}\right) \right] \quad (3.28)$$

where γ describes the ratio between an isotope's apparent atomic mass on the fractionation line and its true mass. The observed NBS 982 Pb fractionation trend is fit by this modified exponential law with $\gamma_{204Pb} = \gamma_{206Pb} = \gamma_{208Pb} = 1$ and $\gamma_{207Pb} = 0.999828$.

Accurate fractionation correction for precise Pb measurements by TIMS requires both a mass-dependent and a mass-independent correction. This may be true especially for Pb measurements made with a ^{205}Pb tracer, an additional odd-mass isotope. If the values of γ_{205Pb} and γ_{207Pb} are observed to vary between analyses, this additional uncertainty should be considered when interpreting high-precision datasets.

3.5 Isochrons, Mixing Lines, and the Statistics of Compositional Data

The exponential and Rayleigh fractionation laws presented in Section 3.4 predict linear trends in log-ratio coordinates, but contain exponential terms in isotope ratio coordinates. In contrast, isotopic mixing lines and isochron relationships have linear trends only in the (non-logged) isotope ratio coordinates. Fitting a straight line to these models thus requires evaluating means and covariance matrices and minimizing weighted distances in isotope ratio space. There are a number of fundamental problems with all three calculations, which are outlined in full in Aitchison (1986), as well as (e.g., Aitchison, 1984, 1992; Pawlowsky-Glahn and Egozcue, 2006), but have been largely ignored by the isotope geochemistry community. The basic problem is that within a set of isotope ratios or compositional components is an implicit constraint: the sum of the (non-negative) fractional components, is equal to 1, or 100%. Recognizing the unit sum constraint has led to a rich literature on compositional data analysis, and ignoring this constraint manifests itself in several intuitively unpredictable ways, detailed in Aitchison (1986), with two symptoms outlined briefly

below. The non-linear regression algorithm required by isochron and convex mixing models is beyond the scope of this work.

3.5.1 Some Pitfalls of Conventional Multivariate Statistics for Isotope Ratios

Consider evaluating the arithmetic means \bar{r}_1 and \bar{r}_2 of n measurements of the isotope ratios $r_1 = (a/b)$ and $r_2 = (c/b)$. For the same n measurements, the arithmetic mean \bar{r}_3 of $r_3 = (a/c)$ is not \bar{r}_1/\bar{r}_2 . Therefore, any statistical inference made, for instance an age derived from an isochron, will depend on the arbitrary choice of numerator and denominator isotopes when the ratios are measured: expressing the system in terms of r_2 and r_3 instead of r_1 and r_2 or their reciprocals would yield different results. Note that the same problem applies to ratios expressed in ϵ or δ notation.

This problem does not extend to the log-ratios utilized in Section 3.4. For instance, the arithmetic means \bar{R}_1 and \bar{R}_2 of n measured log-ratios $R_1 = \log(a/b)$ and $R_2 = \log(c/b)$ can be subtracted to calculate the mean \bar{R}_3 of $R_3 = \log(a/c)$. Transforming back to (non-logged) isotope ratio space by evaluating $\hat{r}_1 = \exp(\bar{R}_1)$, $\hat{r}_2 = \exp(\bar{R}_2)$, and $\hat{r}_3 = \exp(\bar{R}_3)$ generates a self-consistent set of means, so that $\hat{r}_1/\hat{r}_2 = \hat{r}_3$. Because \bar{R} is the arithmetic mean of the measured log-ratios, \hat{r} is the geometric mean of the isotope ratios.

Using the covariance matrix of the measured isotope ratios to define a multivariate normal probability distribution function (e.g., Ludwig, 2003; McLean et al., 2011) has several related shortcomings. First, the multivariate normal distribution assigns a finite probability over all positive and negative real numbers, which is inappropriate for isotope ratios that are assumed to always be greater than or equal to zero. Although this effect is negligible for analyses with small uncertainties far from zero, it is more pronounced for measurements with larger uncertainties and low absolute values. For instance, the inverse Pb isochron in Fig. 2 of Amelin et al. (2009) features several highly radiogenic analyses with large leverage on the Pb-Pb date whose 2σ uncertainty ellipses overlap negative $^{204}\text{Pb}/^{206}\text{Pb}$ values.

In contrast, log-ratios are permitted to be negative, since the exponential function that transforms back to (non-logged) isotope ratios generates only positive values. The assumption of a normal distribution for the log-ratios is equivalent to assuming a log-normal distribution for the isotope ratios themselves. This difference becomes smaller for increasing precision and distance from a zero value, and the distinction for data near detection limits merits further investigation with empirical data. However, the fact that the log-normal distribution is defined only over positive values represents a step in the right direction.

Both internal inconsistencies outlined above become less severe as data

3.5.2 Application of Compositional Data Methods to Exponential Mass Fractionation

The exponential fractionation correction equations (3.25) and (3.27) in Section 3.4.1 are cumbersome, especially when the presence of three or more isotopes necessitate a system of pairwise equations. However, the same relationship for all isotopes can also be written succinctly as a linear function of compositional vectors, using the operators appropriate for compositional data:

$$\mathbf{x}_{corr} = \mathbf{x}_{meas} \oplus (\beta \otimes \mathbf{mass}) \quad (3.29)$$

In this equation, both \mathbf{x}_{meas} and \mathbf{mass} are compositional data vectors, which express the relative proportion of each component and sum to a constant, for instance 1 or 100%. Thus a typical measured Pb IC $\langle {}^{204}\text{Pb}/{}^{206}\text{Pb}, {}^{207}\text{Pb}/{}^{206}\text{Pb}, {}^{208}\text{Pb}/{}^{206}\text{Pb} \rangle$ of $\langle 0.0273, 0.4668, 0.9989 \rangle$ from Section 3.4 becomes $\mathbf{x}_{meas} \approx \langle 0.011, 0.4011, 0.1872, 0.4007 \rangle$, where the four components correspond to the fractional abundances of ${}^{204}\text{Pb}$, ${}^{206}\text{Pb}$, ${}^{207}\text{Pb}$, and ${}^{208}\text{Pb}$.

Normalization to a constant sum, in this case unity, performs the same function as evaluating ratios instead of utilizing absolute intensities or abundances. Only the ratios of the isotopic masses are used in equations (3.25) and (3.27) as well, and so they too form a compositional data vector and can be normalized to the same constant.

Note that the arbitrary fractionation factor β used in equation (3.29) has the opposite sign as that used in equations (3.25) and (3.27), so that the same corrected Pb IC would be calculated using for instance $\beta = 1.4$ in equation (3.25) and $\beta = -1.4$ in equation (3.29).

The two operations \oplus and \otimes in equation (3.29), known as perturbation and power transformation respectively, are the compositional analogues of addition and multiplication. As defined by Aitchison (1986) for D total compositional components, they are

$$\mathbf{x} \oplus \mathbf{y} = \mathcal{C}\langle x_1y_1, x_2y_2, \dots, x_Dy_D \rangle \quad (3.30)$$

$$\beta \otimes \mathbf{y} = \mathcal{C}\langle y_1^\beta, y_2^\beta, \dots, y_D^\beta \rangle \quad (3.31)$$

where the closure operator \mathcal{C} is simply normalizes the resulting vector components to a constant sum.

Transforming the compositional data vectors into log-ratios with a common denominator (e.g., ^{206}Pb in the example) is the additive log-ratio transform (alr) of Aitchison (1986), which is familiar to isotope geochemists as the natural sample space for plotting exponential fractionation trends as straight lines.

After performing the alr, the analogy of the perturbation and power transform to addition and multiplication become clear. For instance, the $[\log(M_b/M_a) + \log(\gamma_b/\gamma_a)]$ term in equation (3.28) can be rewritten as an expression for a modified ‘effective’ mass vector for isotopes undergoing mass independent fractionation,

$$\mathbf{mass}' = \mathbf{mass} \oplus \mathbf{gamma} \quad (3.32)$$

Multiplying \mathbf{mass}' by β in equation (3.28) becomes a power transform, so that a modified form of the exponential equation, including mass independent effects, is

$$\mathbf{x}_{corr} = \mathbf{x}_{meas} \oplus (\beta \otimes \mathbf{mass}') \quad (3.33)$$

Thus, the complicated system of equations needed to describe the behavior of multi-

ple isotopes exhibiting mass-independent fractionation takes an elegant linear form, analogous to the line $\mathbf{a} + \mathbf{v}t$. Here, the \mathbf{a} is the measured isotopic composition represented by the \mathbf{x}_{meas} , the slope vector \mathbf{v} is the effective masses \mathbf{mass}' , and the position parameter t is the fractionation parameter β .

3.6 Summary and Conclusions

Although a number of straight line regression algorithms are used by the geochemical community, none treat the general case of data with correlated uncertainties in two or more dimensions. The best fit line parameters are those that maximize their likelihood function, and are found by setting the derivative of the log-likelihood function to zero. Uncertainties in the regression parameters are then determined by using the second derivatives of the log-likelihood equation.

Isotopic fractionation is often modeled by linear functions in log-ratio space, such as the Rayleigh and exponential laws. An experiment testing their applicability to Pb analysis by TIMS shows that progressive fractionation during an analysis is well fit by a linear trend. Although the mass-dependent fractionation prediction made by the linear and Rayleigh laws hold for even mass number Pb isotopes, ^{207}Pb exhibits constant-magnitude mass-independent fractionation throughout the analysis, described by a modified exponential fractionation law.

For compositional data, the linear regression algorithm is valid only when the data are treated as log-ratios. Models that are not linear in this space, such as isochrons and mixing lines, cannot be fit by a line because self-consistent means, covariance matrices, and distances cannot be calculated in isotope ratio space. The established field of compositional data analysis can be used to extend the findings herein.

3.7 Appendix A: Second Derivatives of log-Likelihood Equation for Best Fit Line

$$\frac{\partial^2 \ln \mathcal{L}}{\partial \mathbf{a} \mathbf{a}^\top} = \sum_{i=1}^n \frac{\Sigma_i^{-1} \mathbf{v} \mathbf{v}^\top \Sigma_i^{-1}}{\mathbf{v}^\top \Sigma_i^{-1} \mathbf{v}} - \Sigma_i^{-1} \quad (3.34)$$

$$\frac{\partial^2 \ln \mathcal{L}}{\partial \mathbf{a} \mathbf{v}^\top} = \sum_{i=1}^n \frac{2(\mathbf{p}_i - \mathbf{a})^\top \Sigma_i^{-1} \mathbf{v} \Sigma_i^{-1} \mathbf{v} \mathbf{v}^\top \Sigma_i^{-1} - \mathbf{v}^\top \Sigma_i^{-1} \mathbf{v} (\Sigma_i^{-1} \mathbf{v} (\mathbf{p}_i - \mathbf{a})^\top \Sigma_i^{-1} + (\mathbf{p}_i - \mathbf{a})^\top \Sigma_i^{-1} \mathbf{v} \Sigma_i^{-1})}{(\mathbf{v}^\top \Sigma_i^{-1} \mathbf{v})^2} \quad (3.35)$$

$$\frac{\partial^2 \ln \mathcal{L}}{\partial \mathbf{v} \mathbf{a}^\top} = \left(\frac{\partial^2 \ln \mathcal{L}}{\partial \mathbf{a} \mathbf{v}^\top} \right)^\top \quad (3.36)$$

$$\begin{aligned} \frac{\partial^2 \ln \mathcal{L}}{\partial \mathbf{v} \mathbf{v}^\top} &= \sum_{i=1}^n \left[(\mathbf{v}^\top \Sigma_i^{-1} \mathbf{v})^2 \left(2\mathbf{v}^\top \Sigma_i^{-1} (\mathbf{p}_i - \mathbf{v}) \Sigma_i^{-1} (\mathbf{p}_i - \mathbf{a}) \mathbf{v}^\top \Sigma_i^{-1} \right. \right. \\ &\quad \left. \left. + \mathbf{v}^\top \Sigma_i^{-1} \mathbf{v} \Sigma_i^{-1} (\mathbf{p}_i - \mathbf{a}) (\mathbf{p}_i - \mathbf{a})^\top \Sigma_i^{-1} - (\mathbf{v}^\top \Sigma_i^{-1} (\mathbf{p}_i - \mathbf{a}))^2 \Sigma_i^{-1} \right. \right. \\ &\quad \left. \left. - 2\mathbf{v}^\top \Sigma_i^{-1} (\mathbf{p}_i - \mathbf{a}) \Sigma_i^{-1} \mathbf{v} (\mathbf{p}_i - \mathbf{a})^\top \Sigma_i^{-1} \right) \right. \\ &\quad \left. - 4\mathbf{v}^\top \Sigma_i^{-1} \mathbf{v} \left(\mathbf{v}^\top \Sigma_i^{-1} \mathbf{v} \mathbf{v}^\top \Sigma_i^{-1} (\mathbf{p}_i - \mathbf{a}) \Sigma_i^{-1} (\mathbf{p}_i - \mathbf{a}) \right. \right. \\ &\quad \left. \left. - (\mathbf{v}^\top \Sigma_i^{-1} (\mathbf{p}_i - \mathbf{a}))^2 \Sigma_i^{-1} \mathbf{v} \right) \mathbf{v}^\top \Sigma_i^{-1} \right] \\ &\quad / (\mathbf{v}^\top \Sigma_i^{-1} \mathbf{v})^4 \end{aligned} \quad (3.37)$$

3.8 Appendix B: Multivariate weighted mean

Equation (3.3) is the multivariate probability density function at any point \mathbf{x} in the vicinity of the measurement \mathbf{p}_i with covariance matrix Σ_i . For a dataset of n measurements $\mathbf{P} = (\mathbf{p}_1, \mathbf{p}_2, \dots, \mathbf{p}_n)$, the multivariate weighted mean $\hat{\mathbf{p}}$ can be derived using a maximum likelihood calculation similar to that of the best fit line. Using the probability distribution function in (3.3) to form a likelihood function for $\hat{\mathbf{p}}$ in analogy to equations (3.14) and (3.15),

$$\ln \mathcal{L}(\hat{\mathbf{p}} | \mathbf{P}, \Sigma) \propto \sum_{i=1}^n \ln f(\mathbf{p}_i, \Sigma_i | \hat{\mathbf{p}}) = -\frac{1}{2} \sum_{i=1}^n [(\mathbf{p}_i - \hat{\mathbf{p}})^\top \Sigma_i^{-1} (\mathbf{p}_i - \hat{\mathbf{p}})] \quad (3.38)$$

Setting the derivative of the log-likelihood function with respect to $\hat{\mathbf{p}}$ to zero and solving for the maximum likelihood estimate of $\hat{\mathbf{p}}$ yields

$$\frac{\partial \ln \mathcal{L}}{\partial \hat{\mathbf{p}}} = \sum_{i=1}^n \boldsymbol{\Sigma}_i^{-1} (\mathbf{p}_i - \hat{\mathbf{p}}) = 0 \quad (3.39)$$

$$\hat{\mathbf{p}} = \left[\sum_{i=1}^n (\boldsymbol{\Sigma}_i^{-1}) \right]^{-1} \left[\sum_{i=1}^n (\boldsymbol{\Sigma}_i^{-1} \mathbf{p}_i) \right] \quad (3.40)$$

This explicit estimate for the multivariate weighted mean is a special case of the implicitly defined weighted mean in the presence of overdispersion in Vermeesch (2010).

The covariance matrix for $\hat{\mathbf{p}}$ is the inverse of its Fisher Information Matrix \mathcal{I} ,

$$\mathcal{I} = -\frac{\partial^2 \ln \mathcal{L}}{\partial \hat{\mathbf{p}} \hat{\mathbf{p}}^T} \quad (3.41)$$

$$\boldsymbol{\Sigma}_{\hat{\mathbf{p}}} = \mathcal{I}^{-1} = \left[\sum_{i=1}^n (\boldsymbol{\Sigma}_i^{-1}) \right]^{-1} \quad (3.42)$$

This choice of $\hat{\mathbf{p}}$ minimizes

$$\chi_{red}^2 = \frac{1}{k(n-1)} \sum_{i=1}^n [(\mathbf{p}_i - \hat{\mathbf{p}})^T \boldsymbol{\Sigma}_i^{-1} (\mathbf{p}_i - \hat{\mathbf{p}})] \quad (3.43)$$

the expression for the reduced chi-square sum, also known as the MSWD.

3.9 Figure captions

Figure 3-1: Projection from a measured data point to the best fit line in three dimensions. The best fit line contains the point \mathbf{a} (light blue), and follows the direction vector \mathbf{v} (dark blue arrow). Any point on the line can be given by the expression $\mathbf{a} + \mathbf{v}t$. The closest point on the line to the measured data point \mathbf{p}_i (red) is its perpendicular projection to the line $\hat{\mathbf{p}}_i$, in green. The vector difference between \mathbf{p}_i and $\hat{\mathbf{p}}_i$ is known as the residual vector \mathbf{r}_i , shown as a green line segment.

Figure 3-2: a) The point \mathbf{p} with covariance matrix Σ depicted as a 1σ uncertainty ellipse (Mahalanobis distance = 1) is predicted to lie on the line $\mathbf{a} + \mathbf{v}t$. The perpendicular projection from the point to the line is not the best estimate of the point's location on the line.

b) The system in (a) with an applied linear transform defined by the matrix \mathbf{U} , here a stretching along the horizontal axis. In the transformed system, Euclidean distance is the same as Mahalanobis distance, and the best residual (solid line segment) is determined by the perpendicular projection algorithm of Section 3.2.1.

c) Although it is not part of the fitting algorithm, the inverse linear transform \mathbf{U}^{-1} may be applied to restore the original system. The restored maximum likelihood residual is not the perpendicular vector between the point and the line.

Figure 3-3: Observed isotopic fractionation for a single analysis of Pb standard NBS 982, measured by TIMS using a silica gel activator. Data is plotted in log-ratio space (black axes), with isotope ratio values given on the opposite axis in red.

a) Plots of all measured data, as log-ratios $\log(^{204}\text{Pb}/^{206}\text{Pb})$ and $\log(^{207}\text{Pb}/^{206}\text{Pb})$ vs. $\log(^{208}\text{Pb}/^{206}\text{Pb})$. Each blue measured value represents the mean of 25 consecutive 100-millisecond integrations. The dark green line is the best fit line to the three-dimensional data. For reference, the mass-dependent fractionation line predicted by the exponential equation is plotted in red. While the observed components of the direction vector in ^{204}Pb - ^{206}Pb - ^{208}Pb space, involving all even isotopes, is the same as the predicted MDF line, the $\log(^{207}\text{Pb}/^{206}\text{Pb})$ slope component diverges significantly. The black box marks the plot limits in (b).

b) A closeup of data in (a), plotted with the same conventions. A 2σ uncertainty ellipse is displayed for every twenty-fifth measured mean, with the others omitted for clarity. The 2σ uncertainty envelope for the best fit line is plotted with green dashed lines.

Table 3.1: Maximum likelihood estimates, uncertainties, and correlation coefficients for the best fit line parameters to the NBS 982 Pb fractionation data.

	value	$\pm 2\sigma$	exp. ^a	Ray. ^b
\mathbf{a}_1	-3.604198	0.000061		
\mathbf{a}_2	-0.7613001	0.0000041		
\mathbf{a}_3^c	<i>0.00016</i>	–		
\mathbf{v}_1	-0.993	0.040	-1.009	-1.014
\mathbf{v}_2	0.4836	0.0027	0.5014	0.5020
\mathbf{v}_3^c	<i>1</i>	–		

Matrix of correlation coefficients for uncertainties in fit parameters:

	\mathbf{a}_1	\mathbf{a}_2	\mathbf{v}_1	\mathbf{v}_2
\mathbf{a}_1	1			
\mathbf{a}_2	0.032	1		
\mathbf{v}_1	0.726	0.021	1	
\mathbf{v}_2	0.021	0.721	0.028	1

^a value predicted by exponential law

^b value predicted by Rayleigh law

^c value set explicitly

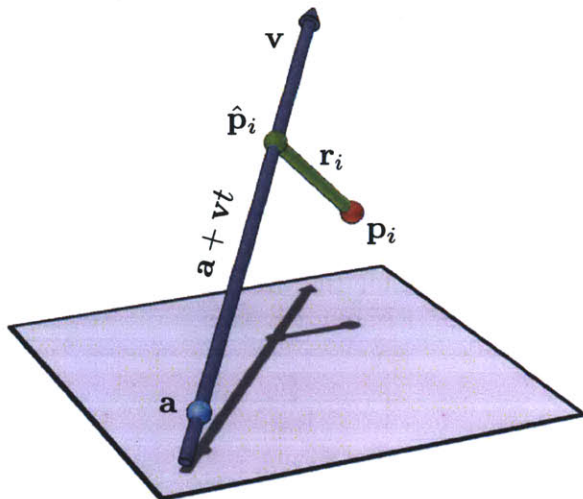


Figure 3-1: Linear regression parameters

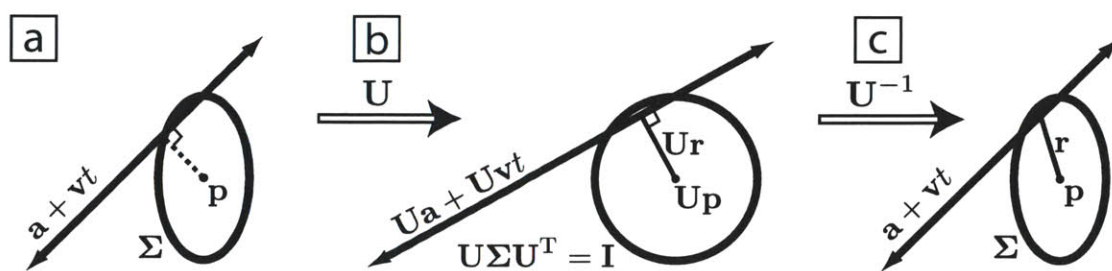


Figure 3-2: Maximum likelihood by Cholesky transformation

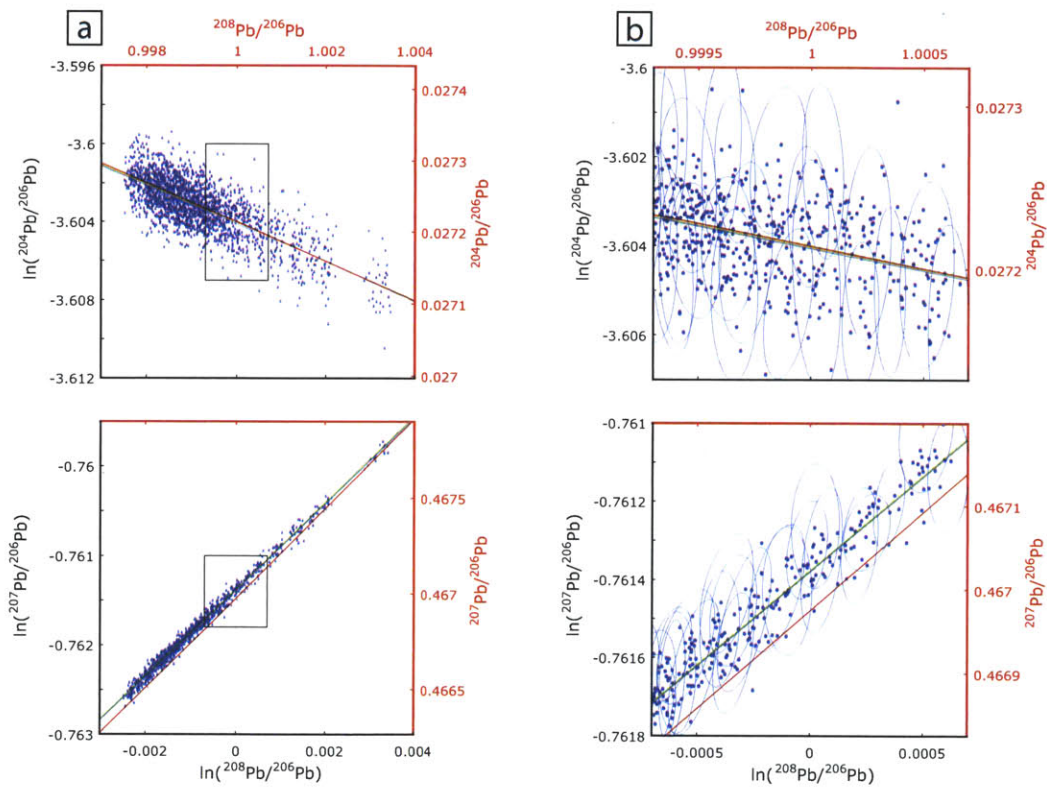


Figure 3-3: Observed isotopic fractionation for a single analysis of NBS 982

Chapter 4

Evaluating Analytical and Systematic Uncertainty in Mixed U-Pb Tracer Calibration

Abstract

U-Pb isotope dilution thermal ionization mass spectrometry (ID-TIMS) dates are among the most precise and accurate available, and as such they underpin much of the geologic timescale. U/Pb isotope ratio determinations by ID-TIMS can be made to very high precision, but they are affected by systematic uncertainties from several sources, including the isotopic standards used to calibrate instrumental mass fractionation, the isotopic composition (IC) and U/Pb ratio of gravimetric solutions used to calibrate the tracer solution, and the ICs of the tracer and blank that are subtracted from each analysis. When considered with decay constant uncertainties and corrections for intermediate daughter excess/deficiencies, these provide a fundamental limitation on the absolute uncertainties achievable by ID-TIMS. The EARTHTIME effort to calibrate mixed (^{202}Pb)- ^{205}Pb - ^{233}U - ^{235}U tracer for community use provides an opportunity to unravel the correlations between the tracer parameters and between the tracer and major components of systematic uncertainty. This contribution conditions

the tracer calibration parameters on first-principles measurements of mass and purity that are traceable to SI units. Because the calculated tracer isotope ratios all depend on a common set of measurements, their uncertainties are correlated. For U-Pb date determinations, accounting for the uncertainty correlations reveals that uncertainties in the $^{206}\text{Pb}/^{238}\text{U}$ ratio, and therefore the $^{206}\text{Pb}/^{238}\text{U}$ date, are expected to be roughly half of the total uncertainty in the $^{235}\text{U}/^{205}\text{Pb}$ ratio. Combined with new, more accurate purity measurements, the tracer uncertainty contribution to $^{206}\text{Pb}/^{238}\text{U}$ dates is found to be <300 ppm. Calibration of other existing tracer with this algorithm using the same a priori constraints will be relatable to the EARTHTIME tracer and to SI units, and may achieve similar precision.

4.1 Introduction

The elements Pb and U cannot be measured simultaneously on a thermal ionization mass spectrometer (TIMS). Instead, U/Pb ratios are measured relative to a tracer that contains a mixture of synthetically enriched U and Pb isotopes. Measuring one element at a time, the ratios of natural Pb and U isotopes to their counterparts in the tracer can be used, along with the U/Pb ratio of the tracer, to calculate the U/Pb ratios of the sample and therefore its U-Pb date. This procedure is known as isotope dilution (ID), and the known U/Pb ratio of the tracer that it exploits underlies the accuracy and precision of U-Pb geochronology.

In addition to the artificially enriched isotopes which comprise the majority of Pb and U in the tracer, there is inevitably some contamination by small amounts of naturally occurring, non-enriched isotopes. These derive from impurities in the enriched isotopes or from the acids and laboratory procedures used to create the tracer. Knowledge of the amount of these naturally occurring isotopes in the tracer relative to the enriched isotopes is required so that their contribution may be subtracted from the measured Pb and U to determine the amount of Pb and U in the sample.

Systematic uncertainties in the tracer isotopic composition (IC) control how results from different labs, and to some extent different isotopic decay systems, are com-

pared and confederated to calibrate the geologic timescale. As part of the EARTH-TIME initiative, two mixed U-Pb tracers were created at MIT in 2004-2005. The first, ‘ET535’, is a high-purity mixed ^{205}Pb - ^{233}U - ^{235}U tracer, and the second, ‘ET2535’, additionally contains ^{202}Pb . All four of these isotopes are rare to absent in natural systems, with ^{235}U the most abundant at ca. 0.7% of naturally occurring U. A companion paper (Condon et al., 2011) describes the mass spectrometry and metrology required to calibrate the solutions. This paper details the statistical models behind the calculation of the maximum likelihood estimates for the tracer isotopic composition.

4.1.1 First Principles

The U-Pb system is known as the ‘gold standard’ of geochronology, primarily because its two decay systems, ^{238}U to ^{206}Pb and ^{235}U to ^{207}Pb , under many circumstances provide an internal check on the presence of open-system behavior, and because the U decay constants are particularly well-determined (Jaffey et al., 1971). By counting the number of U decays for each isotope, then making several calculations involving the detector geometry and the purity of the isotopes present, known as a measurement model, Jaffey et al. (1971) relate the U decay constants to the fundamental SI unit of time, the second. Because the detector setup and U purity measurements are not known perfectly, the resulting uncertainties in the decay constant must be considered when relating U-Pb data to dates with that use different decay constants, such as Ar-Ar dates. Thus, it is the measurement, its uncertainties, and a model that relates the measurement to SI units

The decay constant is important, but it is not the only systematic variable required to relate a U-Pb date to SI units. Because the U/Pb ratio measurement is separated, with the use of the isotopic tracer, into separate sample/tracer ratio measurements for Pb and U, the U/Pb ratio of the sample depends on the U-Pb ratio of the tracer as well. This paper details the measurement model required to relate the tracer IC to SI units.

As with the decay constant determinations of Jaffey et al. (1971), the connec-

tion between the first principles determinations in SI units, principally measurements of mass, and the final results is made with a measurement model, a documented framework of equations and algorithms that transform measured data into useful parameters, here the tracer IC. The measured data in this framework may be refined in the future and then easily incorporated into the whole, producing new tracer values, but retaining the same uncertainty structure. It is important to clearly establish the assumptions and reference values used to calibrate the tracer, as well as their internal consistency. For instance, the EARTHTIME tracer solution is calibrated against the gravimetrically determined $^{208}\text{Pb}/^{206}\text{Pb}$ of NBS 981 for Pb and $^{233}\text{U}/^{236}\text{U}$ of CRM 3636 for U.

The wealth of data from the tracer calibration exercise provides the opportunity to evaluate the dependence of calculated U-Pb and Pb-Pb dates on systematic uncertainties, which at their most fundamental level are weighing and purity measurements. The primary goal is to establish tracer values and uncertainties in this absolute reference frame. This first enables rigorous inter-comparison between U-Pb data measured with different tracers that are both calibrated to the same reference materials—even if you're not using the ET tracer, you can still calibrate your own tracer to the same set of gravimetric solutions—and second provides an important datum for comparing between isotopic decay systems (e.g. U-Pb and Ar-Ar).

Outline of the Tracer Calibration Algorithm

1. Inter-calibrate Pb and U ICs of all isotopic standards used for tracer calibration.
2. Interpret total procedural blank measurements as tracer-blank mixing lines to estimate the IC of non-enriched tracer isotopes.
3. Use critical mixtures of the tracer and multiple U isotopic standards to estimate the U IC of the tracer.
4. Determine the U/Pb ratios of the gravimetric solutions using measurements of mass, purity, and the ICs of their constituent Pb and U standards.

5. Combine results from all previous calculations to estimate the $^{235}\text{U}/^{205}\text{Pb}$ and $^{202}\text{Pb}/^{205}\text{Pb}$ ratio of the tracer using mixtures of the tracer with three gravimetric solutions.

4.2 Application of Inverse Methods

4.2.1 Measurement Model

Relating the isotopic composition of the tracer to first principles measurements requires a large quantity of data: over 10^5 measured isotope ratios are used by the algorithms that follow. Each measured isotope ratio contains information about the mixture of components being analyzed, which include the small but unavoidable Pb and U contamination known as laboratory blank, along with the tracer, a gravimetric solution, or both. Unraveling the ICs and relative proportions of each component is made more difficult by isotopic fractionation, or the preferential evaporation, ionization and/or detection of lighter isotopes over heavier ones, which changes in magnitude during the course of long analyses. Thus, a measured ratio may be expressed as a ratio of its summed components, modified by a correction factor for isotopic fractionation. A system of equations composed of these nonlinear functions, one for each measured ratio, is known as the measurement model, and its formulation is the first step of tracer calibration.

The model parameters, such as the ICs and relative proportions of the tracer, isotopic standards, and blank, as well as the magnitude of isotopic fractionation, fall into several categories. The parameters measured by first principles, which underpin the tracer calibration, have values that are known a priori, with systematic uncertainties, and their value and uncertainty remain unchanged with the addition of new information. Other parameters, such as the relative quantity of the blank in an analysis, can be estimated from prior experience, but if they can be further constrained by the isotope ratio measurements and the measurement model, then their value is allowed to change within the a priori limits. Finally, there are free model parameters,

such as the IC of the tracer, that have essentially no a priori information and which are constrained by both the assumed systematic variables and the measured isotope ratios through the measurement model.

If there are more measured isotope ratios than parameters to solve for, then the measurement model is overdetermined. When formulated as an inverse problem (e.g. Tarantola and Valette, 1982a,b; Tarantola, 2005), the measurement model may be expressed as $\mathbf{d} = \mathbf{G}(\mathbf{m})$, where \mathbf{d} is a vector of data, in this case isotope ratio measurements, and $\mathbf{G}(\mathbf{m})$ is the (nonlinear) function of the the model parameters \mathbf{m} that explains the measured data.

4.2.2 Solving the Inverse Problem

The best choice of the parameter values $\hat{\mathbf{m}}$ minimizes the misfit between the observed values of the isotope ratios on the left hand side of the equations with the values predicted by the right-hand side. The misfit applies both to the difference between the data and the model predictions, $\mathbf{d} - \mathbf{G}(\mathbf{m})$, which should agree within the uncertainties of the measured data, and the difference between any prior constraints on the model parameters and the best fit values, $\mathbf{m}_{\text{prior}} - \hat{\mathbf{m}}$. These differences are weighted by the measured uncertainties for the data and the a priori uncertainties in the model parameters. The free model parameters considered unknowns are given diffuse priors, or large initial uncertainties, which are then resolved by considering the constraints supplied by the measured data and other better-constrained model parameters.

The misfit or objective function whose minimum is the solution to the inverse problem is (Tarantola, 2005)

$$S = (\mathbf{d} - \mathbf{G}(\hat{\mathbf{m}}))^T \mathbf{C}_D^{-1} (\mathbf{d} - \mathbf{G}(\hat{\mathbf{m}})) + (\mathbf{m}_{\text{prior}} - \hat{\mathbf{m}})^T \mathbf{C}_M^{-1} (\mathbf{m}_{\text{prior}} - \hat{\mathbf{m}}) \quad (4.1)$$

where \mathbf{C}_D and \mathbf{C}_M are the covariance matrices of the measured data and the prior model parameter estimates, respectively. To minimize S , a stable preconditioned steepest descent method is employed (Tarantola, 2005). The algorithm calculates the gradient, or multi-dimensional direction in which the value of S is most rapidly

decreasing, then uses an estimate of the curvature of the S to estimate a trial minimum value. At the trial minimum, a new gradient and curvature are estimated, and the procedure may be iterated until convergence. The resulting estimate $\hat{\mathbf{m}}$ is the maximum likelihood estimate of the model parameter values.

To evaluate the measurement uncertainties, or the joint conditional density function of the model parameters treated as unknowns given the estimates of systematic variables, near-zero uncertainties were assigned to the systematic variables, and the overdetermined non-linear system was solved using these values. The measurement uncertainties are calculated by approximating the function $G(\hat{\mathbf{m}})$ with its Jacobian matrix evaluated at the solution, denoted G . The matrix G has a row for each measured isotope ratio and a column for each model parameter, and contains the derivative of each of the predicted measured isotope ratio with respect to the model parameters. The measured uncertainties are estimated using

$$\tilde{C}_M^{meas} = C_M - C_M G^T (G C_M G^T + C_D)^{-1} G C_M \quad (4.2)$$

which can be derived from equation (4.1), the objective function (Tarantola, 2005).

In order to evaluate the component of uncertainty arising from systematic effects, the entire nonlinear inverse problem can be solved for M Monte Carlo realizations of the systematic parameters, created with a pseudorandom number generator to have the desired probability density function, usually a multivariate Gaussian. The value of M here ranges from 10^4 to 10^7 , depending on the computational difficulty of the calculation. The systematic parameters, such as the assumed $^{208}\text{Pb}/^{206}\text{Pb}$ ratio of NBS 981, can either be given infinitesimally small prior uncertainties to ensure that the model converges to the input value, or can be omitted from \mathbf{m} entirely.

For the model parameters treated as unknowns, the distribution of the M resulting solutions defines the probability distribution of the model parameters resulting from the input systematic uncertainties. Because the model $G(\mathbf{m})$ is nonlinear, even if the uncertainties in the measured data and systematic variables all have Gaussian distributions, the calculated uncertainties in the other output model parameters, such

as the $^{235}\text{U}/^{205}\text{Pb}$ of the tracer, may be significantly non-Gaussian. The departure from the normal distribution depends on both the degree of non-linearity of the system at the value of the solution and the size of the input uncertainties. Solving the least squares system for many Monte Carlo realizations of the systematic variables provides a way to evaluate the probability distribution of the output model parameters without assuming that the model is locally linear. The normality of the Monte Carlo-modeled solutions can be checked by plotting the data as a histogram or a Q-Q plot, or with a Kolmogorov-Smirnov (K-S) test, which compares the observed Monte-Carlo distribution with the theoretically predicted normal distribution with the same mean and standard deviation.

If the systematic uncertainties in the model parameters are confirmed to be normally distributed, they can be estimated by evaluating the mean and covariance matrix of the M estimates of $\hat{\mathbf{m}}$, denoted \tilde{C}_M^{sys} . The total systematic and measurement uncertainty can then be expressed as the sum of the measured and systematic covariance matrices:

$$\tilde{C}_M^{tot} = \tilde{C}_M^{meas} + \tilde{C}_M^{sys} \quad (4.3)$$

4.3 Inter-calibration of Pb and U standards

In order to determine the U-Pb ratio of the ET(2)535 tracers, each was mixed with three gravimetric solutions that have known U and Pb concentrations. The solutions are composed of three different Pb standards, NBS 981 and 982 from the National Bureau of Standards and ‘Puratronic Pb’ from Alfa Aesar, along with two different U standards, CRM 112a and CRM 115. An additional U standard, U500, was used to separately evaluate the U IC of the tracers. The tracer U IC is then used in the fractionation correction equations for the gravimetric-tracer mixture data reduction.

Because all six isotopic standards are used to determine the tracer U/Pb ratio, their uncertainties all contribute to the final uncertainty budget of the tracer IC, and any correlation between the uncertainties in their ICs must be considered when averaging the results from the three gravimetric solutions. This uncertainty correla-

tion results from relating the ICs of the standards to SI units, accomplished for both U and Pb by measuring the isotope ratios of the standards against an independent gravimetrically calibrated isotope ratio, a process known as inter-calibration.

4.3.1 U Standard Inter-calibration

To relate the isotopic compositions of the U standards to one another, we measured each against IRMM 3636(a), which was fabricated by weighing highly isotopically pure ^{233}U and ^{236}U and mixing them in a 1:1 ratio (Verbruggen et al., 2008). Because the artificial isotopes that comprise IRMM 3636(a) have been weighed against an in-house kilogram reference, its precisely determined $^{233}\text{U}/^{236}\text{U}$ is traceable to the SI system, and ICs that have been measured against it are relatable to the SI through their measurement uncertainties and to one another by tracing each measurement back to SI units.

In this way, the $^{238}\text{U}/^{235}\text{U}$ ratios and uncertainties for the standards SRM U500 and CRM 112a can be related using the supplementary data from Condon et al. (2010), which reports the derivative or linear dependence of each measured IC with respect to IRMM 3636. New CRM115 data is provided in the supplementary data of this publication, and is reduced using the same algorithms as Condon et al. (2010).

No correlations between the isotope ratio uncertainties are reported on the IRMM 3636 certificate of analysis, so they are assumed to be uncorrelated. The uncertainty in the IC of IRMM 3636a is treated here as a systematic uncertainty among the standard analyses. CRM 115 and CRM U500 are both synthetic standards and thus contain ^{236}U , a common fission byproduct. The $^{236}\text{U}/^{235}\text{U}$ values for each were measured for un-spiked aliquots, then this source of ^{236}U was subtracted before using the $^{236}\text{U}/^{233}\text{U}$ of IRMM 3636(a) to determine the magnitude of isotopic fractionation.

4.3.2 Pb Standard Inter-calibration

Unlike the well-calibrated IRMM-3636(a) solution for U, there is no gravimetrically calibrated mixture of synthetically produced isotopes against which Pb isotopic stan-

dards can be measured. However, the NBS 981, 982, and 983 standards have been calibrated by sample-standard bracketing with mixtures of high-purity ^{208}Pb and ^{206}Pb that were gravimetrically mixed to mimic the $^{208}\text{Pb}/^{206}\text{Pb}$ of the standards (Catanzao et al., 1968). As such, these determinations may be considered traceable to SI units.

However, modern mass spectrometric measurements are significantly more precise, and modern laboratory protocols have significantly lower contamination levels, or laboratory blanks, which may bias the measurements. Because the original high-purity ^{208}Pb and ^{206}Pb used by Catanzao et al. are no longer available, the absolute uncertainties with respect to SI units cannot be improved with new measurements, but the relative uncertainties between the Pb standards may be significantly refined. For this purpose, we assume the gravimetrically traceable $^{208}\text{Pb}/^{206}\text{Pb}$ of Catanzao et al. (1968) of 2.1681 ± 0.0008 (2σ), and use a series of measurements of each gravimetric solution against a common ^{202}Pb - ^{205}Pb tracer to relate the ICs of the Pb standards to one another. Because the 2σ uncertainty in the $^{208}\text{Pb}/^{206}\text{Pb}$ of NBS 981 in Catanzao et al. (1968) is derived from a 95% confidence interval calculated with linear, rather than quadratic addition, it is likely to be a conservative estimate of the true precision of the original measurement.

Model

To inter-calibrate the Pb isotopic standards against a ^{202}Pb - ^{205}Pb tracer, while monitoring the effect of a BaPO_2 isobaric interference, six masses must be measured. The contributions to each measured mass may be broken down as follows,

$$\begin{aligned}
 201_{tot} &= {}^{201}\text{BaPO}_2 \\
 202_{tot} &= {}^{202}\text{Pb}_{tr} + {}^{202}\text{BaPO}_2 \\
 204_{tot} &= {}^{204}\text{Pb}_{gr} + {}^{204}\text{Pb}_{bl} + {}^{204}\text{Pb}_{tr} + {}^{204}\text{BaPO}_2 \\
 205_{tot} &= {}^{205}\text{Pb}_{tr} + {}^{205}\text{BaPO}_2
 \end{aligned} \tag{4.4}$$

$$206_{tot} = {}^{206}\text{Pb}_{gr} + {}^{206}\text{Pb}_{bl} + {}^{206}\text{Pb}_{tr}$$

$$207_{tot} = {}^{207}\text{Pb}_{gr} + {}^{207}\text{Pb}_{bl} + {}^{207}\text{Pb}_{tr}$$

$$208_{tot} = {}^{208}\text{Pb}_{gr} + {}^{208}\text{Pb}_{bl} + {}^{208}\text{Pb}_{tr}$$

where *gr* denotes a contribution from the Pb standard used in the gravimetric U-Pb solution, *tr* from the tracer, and *bl* from the laboratory blank.

The moles of each isotope of Pb can be normalized to ${}^{202}\text{Pb}$, which occurs only in the tracer. Likewise, the BaPO_2 can be normalized to the polyatomic ion with molecular weight 205.

$$201_{tot}/{}^{202}\text{Pb}_{tr} = {}^{201}\text{BaPO}_2/{}^{205}\text{BaPO}_2$$

$$202_{tot}/{}^{202}\text{Pb}_{tr} = 1 + {}^{202}\text{BaPO}_2/{}^{205}\text{BaPO}_2$$

$$204_{tot}/{}^{202}\text{Pb}_{tr} = {}^{204}\text{Pb}_{gr}/{}^{202}\text{Pb}_{tr} + {}^{204}\text{Pb}_{bl}/{}^{202}\text{Pb}_{tr} + {}^{204}\text{Pb}_{tr}/{}^{202}\text{Pb}_{tr} + {}^{204}\text{BaPO}_2/{}^{205}\text{BaPO}_2$$

$$205_{tot}/{}^{202}\text{Pb}_{tr} = {}^{205}\text{Pb}_{tr}/{}^{202}\text{Pb}_{tr} + 1 \tag{4.5}$$

$$206_{tot}/{}^{202}\text{Pb}_{tr} = {}^{206}\text{Pb}_{gr}/{}^{202}\text{Pb}_{tr} + {}^{206}\text{Pb}_{bl}/{}^{202}\text{Pb}_{tr} + {}^{206}\text{Pb}_{tr}/{}^{202}\text{Pb}_{tr}$$

$$207_{tot}/{}^{202}\text{Pb}_{tr} = {}^{207}\text{Pb}_{gr}/{}^{202}\text{Pb}_{tr} + {}^{207}\text{Pb}_{bl}/{}^{202}\text{Pb}_{tr} + {}^{207}\text{Pb}_{tr}/{}^{202}\text{Pb}_{tr}$$

$$208_{tot}/{}^{202}\text{Pb}_{tr} = {}^{208}\text{Pb}_{gr}/{}^{202}\text{Pb}_{tr} + {}^{208}\text{Pb}_{bl}/{}^{202}\text{Pb}_{tr} + {}^{208}\text{Pb}_{tr}/{}^{202}\text{Pb}_{tr}$$

The molar Pb ratios may be recast in terms of the ratio of gravimetric solution and laboratory blank Pb to that in the tracer and the ICs of the three components. Likewise, the BaPO_2 contribution to each measured mass may be recast in terms of the ratio of BaPO_2 to tracer and the BaPO_2 IC. This is accomplished by defining *r62gt* and *r62bt* as the ratio of the ${}^{206}\text{Pb}$ contribution from the gravimetric solution and the laboratory blank to the ${}^{202}\text{Pb}$ contribution from the tracer, respectively, and *r52BaPb* as the ratio of the ${}^{205}\text{BaPO}_2$ to the ${}^{202}\text{Pb}$ contribution from the tracer. The tracer IC is then expressed as the isotope ratios *r25t*, *r42t*, *r62t*, and *r72t*, representing $({}^{202}\text{Pb}/{}^{205}\text{Pb})_{tr}$, $({}^{204}\text{Pb}/{}^{202}\text{Pb})_{tr}$, and so on, and likewise for *r46b*, *r76b*,

$r86b$ for the blank IC; $r46g$, $r76g$, $r86g$ for the gravimetric Pb standard IC; and $r15Ba$, $r25Ba$, and $r45Ba$ for the ratios of BaPO₂ components. The measured signal at each mass can then be written as

$$\begin{aligned}
201_{tot}/^{202}\text{Pb}_{tr} &= r15Ba \cdot r52BaPb \\
202_{tot}/^{202}\text{Pb}_{tr} &= 1 + r25Ba \cdot r52BaPb \\
204_{tot}/^{202}\text{Pb}_{tr} &= r42t + r46g \cdot r62gt + r46b \cdot r62bt + r45Ba \cdot r52BaPb \\
205_{tot}/^{202}\text{Pb}_{tr} &= 1/r25t + r52BaPb \\
206_{tot}/^{202}\text{Pb}_{tr} &= r62t + r62gt + r62bt \\
207_{tot}/^{202}\text{Pb}_{tr} &= r62t + r76g \cdot r62gt + r76b \cdot r62bt \\
208_{tot}/^{202}\text{Pb}_{tr} &= r82t + r86g \cdot r62gt + r86b \cdot r62bt
\end{aligned} \tag{4.6}$$

Finally, the left hand side of equations (4.6) can be expressed as measured isotope ratios with 206_{tot} in the denominator. The right hand side of each equation must then be divided through by $r62t + r62gt + r62bt$. To equate the measured isotope ratios to the true IC of the sample, isotopic fractionation, or the preferential evaporation, ionization, and/or detection of light isotopes over heavier ones, must be considered as well. We use the a modified exponential fractionation law (Russell et al., 1978), which has been shown empirically to closely model measured Pb isotopic data analyzed with a silica gel emitter (McLean, 2011).

Pb has also been observed to exhibit mass-independent fractionation (MIF), with odd-numbered isotopes preferentially evaporating and/or ionizing relative to the mass-dependent trend predicted by exponential fractionation (Doucelance and Manhès, 2001; Amelin et al., 2005; McLean, 2011). For large loads effectively free of isobaric interferences, this effect has been observed to remain constant throughout the analysis of a sample loaded on a single filament, and can be parameterized a factor γ that is unique to each isotope and is expected to be 1 for even-mass number isotopes. The modified exponential equation for two isotopes a and b thus takes the form (McLean,

2011)

$$\left(\frac{a}{b}\right)_m = \left(\frac{a}{b}\right)_{true} \cdot \left(\frac{M_a \cdot \gamma_a}{M_b \cdot \gamma_b}\right)^\beta \quad (4.7)$$

where M_a and M_b are the atomic masses of isotopes a and b , and $(a/b)_m$ and $(a/b)_{true}$ are the measured and true (fractionation-corrected) isotope ratios, respectively. For clarity, the β in equation (4.7) has the opposite sign but same absolute value as the conventional exponential fractionation equation.

Assuming $\gamma_{202} = \gamma_{204} = \gamma_{206} = \gamma_{208} = 1$, then dividing through by $206_{tot}/^{202}\text{Pb}_{tr}$ and adding the modified exponential fractionation term to the resulting Pb isotope ratios produces the system of equations

$$\begin{aligned} r_{16}m_j^i &= \frac{r_{15}Ba \cdot r_{52}BaPb_j^i}{r_{62}t + r_{62}gt^i + r_{62}bt^i} \\ r_{26}m_j^i &= \frac{1}{r_{62}t + r_{62}gt^i + r_{62}bt^i} \left(\frac{M_{202}}{M_{206}}\right)^{\beta_j^i} + \frac{r_{25}Ba \cdot r_{52}BaPb_j^i}{r_{62}t + r_{62}gt^i + r_{62}bt^i} \\ r_{46}m_j^i &= \frac{r_{42}t + r_{46}g \cdot r_{62}gt^i + r_{46}b \cdot r_{62}bt^i}{r_{62}t + r_{62}gt^i + r_{62}bt^i} \left(\frac{M_{204}}{M_{206}}\right)^{\beta_j^i} + \frac{r_{45}Ba \cdot r_{52}BaPb_j^i}{r_{62}t + r_{62}gt^i + r_{62}bt^i} \\ r_{56}m_j^i &= \frac{1/r_{25}t}{r_{62}t + r_{62}gt^i + r_{62}bt^i} \left(\frac{M_{205} \cdot \gamma_{205}^i}{M_{206}}\right)^{\beta_j^i} + \frac{r_{52}BaPb_j^i}{r_{62}t + r_{62}gt^i + r_{62}bt^i} \quad (4.8) \\ r_{76}m_j^i &= \frac{r_{72}t + r_{76}g \cdot r_{62}gt^i + r_{76}b \cdot r_{62}bt^i}{r_{62}t + r_{62}gt^i + r_{62}bt^i} \left(\frac{M_{207} \cdot \gamma_{207}^i}{M_{206}}\right)^{\beta_j^i} \\ r_{86}m_j^i &= \frac{r_{82}t + r_{86}g \cdot r_{62}gt^i + r_{86}b \cdot r_{62}bt^i}{r_{62}t + r_{62}gt^i + r_{62}bt^i} \left(\frac{M_{208}}{M_{206}}\right)^{\beta_j^i} \end{aligned}$$

where the superscripted index i refers to an analysis and the subscripted index j refers to an individual measured value. Thus each measurement must be corrected by a unique $r_{52}BaPb$, or magnitude of BaPO_2 isobaric interference, and β , or magnitude of isotopic fractionation, which both change during the course of the analysis. Each analysis, which consists of multiple measurements, has a unique value for $r_{62}gt$ and $r_{62}bt$, which express the relative quantities of tracer, blank, and gravimetric solution, as well as γ_{205} and γ_{207} , which quantify the degree of MIF for the odd-mass number Pb isotopes. Variables without indices, such as the tracer, Pb standard, blank, and

BaPO₂ ICs, are assumed to be constant for all analyses of the same gravimetric Pb standard.

Algorithm

The six equations in the system (4.8) describe the anticipated outcome of measuring a mixture of Pb isotopic standard with laboratory blank and a ²⁰²Pb-²⁰⁵Pb tracer that is undergoing mass-independent fractionation in the presence of a BaPO₂ isobaric interference. Several of the variables on the right hand side of equations (4.8), along with their uncertainties, can be constrained a priori. For instance, the IC of the non-enriched tracer components, along with an average loading blank mass and their uncertainties, can be estimated with the algorithm in Section 4.4. The approximate BaPO₂ IC is calculated from the approximate natural abundances of its component elements (Böhlke et al., 2005), which is assumed to fractionate by 0.1% per u during analysis, and is assigned a 2% prior uncertainty. The relative uncertainties in the isotopic masses of the Pb isotopes are at the ppb level (Audi et al., 2003), and their uncertainties are not propagated here. Finally, a single gravimetric Pb standard isotope ratio is required to calibrate r_{25t} , the ²⁰²Pb/²⁰⁵Pb ratio of the tracer, which can then be used to fractionation-correct the remaining two gravimetric standard Pb ICs.

Parameters treated as unknowns include r_{25t} , the ²⁰²Pb/²⁰⁵Pb ratio of the tracer, and the Pb ICs of the gravimetric solutions, excluding the single assumed ratio. Although the gravimetric solution and tracer masses were weighed prior to mixing, a far more precise estimate of their ratio, represented by r_{62gt} , can be calculated using the mass spectrometry measurements, and so this parameter is treated as an unknown. Finally, the three parameters that describe an instantaneous state of mass-independent fractionation, γ_{205} , γ_{207} , and β , are treated as unknowns.

Thus several measurements of several Pb standards mixed with the same ²⁰²Pb-²⁰⁵ tracer define a system of equations, and the model in (4.8) relates the measured values to the parameters of interest.

Results

To inter-calibrate the Pb isotopic standards used to create the gravimetric solutions, we employed the measurements reported in Amelin and Davis (2006). The Amelin and Davis data is used instead of separate measurements utilizing ET2535 in order to avoid a large expenditure of relatively scarce ^{202}Pb . Thus smaller loads of the gravimetric solutions with ET(2)535, which cannot be used to resolve mass-independent fractionation with high precision, can be used to calibrate the U/Pb ratio of the tracer using accurate Pb standard ICs derived from published data.

Only the highest-precision data reported were used for each standard: ten NBS 981, nine NBS 982, and four Puratronic Pb analyses. Each is reported as several block means and standard errors, with isotope ratios relative to ^{206}Pb , as in equations (4.8), and the measured ratio uncertainties are assumed to be uncorrelated. To avoid uncorrected isobaric interferences, which usually occur at the beginning or end of an analysis and significantly displace the block mean from the trend defined by the majority of the data, all block data for each analysis were plotted in $^{202}\text{Pb}/^{206}\text{Pb}$ - $^{204}\text{Pb}/^{206}\text{Pb}$ - $^{207}\text{Pb}/^{206}\text{Pb}$ - $^{208}\text{Pb}/^{206}\text{Pb}$ coordinates, and any outliers were rejected from further consideration. Plots of the included and excluded block data are shown in the electronic supplement.

After outlier rejection, there are 160 blocks each of NBS 981 and NBS 982, and 36 blocks of Puratronic Pb, each consisting of six measured ratios and uncertainties, for a total of 2136 isotope ratio measurements. This is the length of the vector \mathbf{d} in the model described above. These data can be used to constrain the 824 model parameters in the vector \mathbf{m} needed to describe them: three Pb ratios for each gravimetric Pb standard, five Pb ratios for the IC of the tracer used, three BaPO_2 isotope ratios, three Pb blank ratios, a separate value of r_{62bt} , r_{62gt} , γ_{207} , and γ_{205} for each of the 23 analyses and a separate β and r_{52BaPb} for each of the 356 included blocks. This defines an over-determined system that can be solved by conventional non-linear least squares techniques. We employed an iterative method known as preconditioned gradient descent (Tarantola, 2005) to minimize the misfit function in equation (4.1),

which was executed in MATLAB. Initial values for the model parameters were calculated using a linearized form of equations (4.8), and the derivatives required were calculated analytically for each iteration. The MATLAB code is provided in the electronic supplement.

In this model, the assumed $^{208}\text{Pb}/^{206}\text{Pb}$ ratio of NBS 981, as well as the blank, and BaPO_2 ICs and the ratios of ^{204}Pb , ^{206}Pb , ^{207}Pb , and ^{208}Pb , to ^{202}Pb in the tracer act as systematic uncertainties, whose values and uncertainties are known a priori. The measurement uncertainties are calculated by approximating the function $G(\hat{\mathbf{m}})$ with its Jacobian matrix evaluated at the solution, denoted G . The matrix G has 2136 rows and 824 columns that contain the derivative of each of the 2136 predicted values with respect to the 824 model parameters. The measured uncertainties are estimated using equation (4.2).

The data plotted in Fig. 4-2 for the $^{208}\text{Pb}/^{206}\text{Pb}$ of NBS 982 confirms that the modeled output data is well-approximated by a Gaussian distribution, and the same holds for the other isotope ratios of the gravimetric Pb standards. The results of all Monte Carlo trials are included in the electronic supplement.

The systematic uncertainties in the model parameters may therefore be estimated by evaluating the mean and covariance matrix of the 5000 estimates of $\hat{\mathbf{m}}$, denoted \tilde{C}_M^{sys} . The total systematic and measurement uncertainties, estimated with equations (4.2) and (4.3) are given in Table 4.3, and the correlation coefficients between them, derived from \tilde{C}_M^{tot} , are provided in Table 4.4.

4.4 Determining the Pb IC of the Tracer and Blank

It is not possible to accurately measure the isotopic composition of the tracer and the loading blank independently. Loading any quantity of tracer involves admixture with a silica gel activator, which has a finite Pb blank, and possibly introducing more blank by pipetting the combined solution onto the filament and later exposing it to atmosphere. The IC of the Pb blank is problematic to analyze alone because small (e.g. < 0.3 pg) blanks produce weak ion beams (less than ca. 20 cps ^{204}Pb and

800 cps ^{208}Pb) that are difficult to peak center and focus for accurate measurement. In addition to the average IC of the Pb blank, its variability from load to load is an important uncertainty contribution to both the tracer calibration exercise and analyses of geologic materials (McLean et al., 2011). The practice of combining several Pb blanks into a single analysis averages out and therefore underestimates the blank IC variability, analogous to multi-grain TIMS analyses of heterogeneous age populations.

However, if the loading blank and tracer are measured together, a linear regression algorithm can be used to estimate each. Loading and analyzing several different masses of tracer using the same amount of silica gel establishes a two-component mixing line between the blank IC and the tracer IC. When plotted in $^{204}\text{Pb}/^{205}\text{Pb}$ - $^{206}\text{Pb}/^{205}\text{Pb}$ - $^{207}\text{Pb}/^{205}\text{Pb}$ - $^{208}\text{Pb}/^{205}\text{Pb}$ coordinates, the tracer IC occupies a unique point on this line and the blank IC is defined by its slope. The correct tracer and blank IC together are important for accurately interpreting U-Pb data, especially data with lower Pb^*/Pbc ratios.

4.4.1 Determining the mixing line parameters

The algorithm presented in McLean (2011) calculates the best fit line through data with correlated uncertainties in two or more dimensions, and is well-suited to a four-dimensional mixing model. In this model, a measured mixture of tracer and blank

falls on a mixing line that follows the equation

$$\begin{bmatrix} \left(\frac{^{204}\text{Pb}}{^{205}\text{Pb}}\right)_{mix} \\ \left(\frac{^{206}\text{Pb}}{^{205}\text{Pb}}\right)_{mix} \\ \left(\frac{^{207}\text{Pb}}{^{205}\text{Pb}}\right)_{mix} \\ \left(\frac{^{208}\text{Pb}}{^{205}\text{Pb}}\right)_{mix} \end{bmatrix} = \begin{bmatrix} \left(\frac{^{204}\text{Pb}}{^{205}\text{Pb}}\right)_{tr} \\ \left(\frac{^{206}\text{Pb}}{^{205}\text{Pb}}\right)_{tr} \\ \left(\frac{^{207}\text{Pb}}{^{205}\text{Pb}}\right)_{tr} \\ \left(\frac{^{208}\text{Pb}}{^{205}\text{Pb}}\right)_{tr} \end{bmatrix} + \begin{bmatrix} 1 \\ \left(\frac{^{206}\text{Pb}}{^{204}\text{Pb}}\right)_{bl} \\ \left(\frac{^{207}\text{Pb}}{^{204}\text{Pb}}\right)_{bl} \\ \left(\frac{^{208}\text{Pb}}{^{204}\text{Pb}}\right)_{bl} \end{bmatrix} \cdot \beta_{Pb} \quad (4.9)$$

where *mix*, *tr*, and *bl*, correspond to the mixture, tracer, and blank components, respectively, and β_{Pb} is the ratio of the moles of ^{204}Pb contributed from the blank to the moles of ^{205}Pb from the tracer, which varies from analysis to analysis. This is a parametric equation for a line of the form $\mathbf{p}_i = \mathbf{a} + \mathbf{v} t_i$, where \mathbf{a} is a point on the line corresponding to the tracer IC, as above, and vector \mathbf{v} describes the direction in which the tracer composition is perturbed by the addition of loading blank. Each measured mixture IC \mathbf{p}_i is assigned an uncertainty in the form of a covariance matrix that incorporates measurement and fractionation-correction effects.

Using the measurement uncertainties to weight the line fit assumes that the deviation of each measurement from the best fit line is due only to the assigned measurement uncertainty and that the blank has a single, constant IC. In a dataset of measured tracer-blank mixes, the IC of the blank is expected to vary because it is a mixture of Pb contributions from several sources. For this experiment, the Pb blank combines Pb in the silica gel emitter, Pb obtained from the phosphoric and hydrochloric acid used to dry down the tracer, Pb on the surface of the beaker used for drying and the inner surface of the pipette used for loading, as well as any particulate matter from the inside of the laminar flow bench on which the sample was dried down. Although these often sum to <0.3 pg of total Pb blank (e.g., Rioux et al., 2010), the ICs of the sources are likely variable, as are their relative contributions,

resulting in a Pb blank with variable IC. This would create scatter from the mixing line between the tracer IC (assumed constant) and the mean blank IC beyond that expected from measurement uncertainties alone.

A dataset comprising 18 measurements of loading blank-tracer mixtures exhibit overdispersion, with an MSWD of 39. To correctly account for the blank IC variability as an additional source of scatter, an uncertainty term must be added to each point that is proportional in magnitude to the amount of blank present. Thus, a point on the mixing line close to the IC of the tracer would be perturbed minimally, while a point farther away would be more sensitive to variation in the blank IC. The overdispersion will affect the measured $^{206}\text{Pb}/^{205}\text{Pb}$, $^{207}\text{Pb}/^{205}\text{Pb}$, and $^{208}\text{Pb}/^{205}\text{Pb}$ relative to the measured $^{204}\text{Pb}/^{205}\text{Pb}$, and these effects will be correlated: the blank IC is expected to be variable, but to generally trend between more and less radiogenic Pb ICs.

To calculate the variability in the blank IC from the measured data, a trial tracer IC was first determined by fitting a line to the measurement data using the measurement uncertainties only. This trial tracer IC was subtracted from each measured mixture, and the measurement and fractionation correction uncertainties were propagated to calculate $^{206}\text{Pb}/^{204}\text{Pb}$, $^{207}\text{Pb}/^{204}\text{Pb}$, and $^{208}\text{Pb}/^{204}\text{Pb}$ ratios and covariance matrices for each measurement. The scatter in the resulting estimated blank ICs cannot be explained by measurement uncertainties alone (Fig. 4-3).

Neglecting the measurement uncertainties and calculating the 2σ covariance ellipse for the discrete ratio data will overestimate the true variability of the tracer, since it does not consider the extra scatter caused by measurement uncertainties. Alternatively, the scatter in the Pb blank ICs may result from the sum of two different multivariate normal distributions: the individual measurement uncertainty unique to each data point and a blank IC variability that affects all data points. The maximum likelihood estimate of the covariance matrix for this ‘extra scatter’ (Vermeesch, 2010) is shown in green in Figure 4-3. It is smaller than the discrete data covariance ellipse, and the lower correlation coefficients demonstrate that part of the high correlation of the measured data is due to the high correlation of the measured uncertainties.

In order to account for the excess scatter from the variable Pb blank IC, the

overdispersion covariance matrix must be added to the uncertainty in each measured data point, multiplied by a factor proportional to the distance from the point to the tracer IC. This factor increases linearly with distance along the line from the tracer IC, where it is zero. A new line was fit to the data with these increased uncertainties, a tracer IC chosen, and the overdispersion calculated; iterating these steps quickly converges on the tracer IC, and the uncertainties in the line parameters now reflect all sources of scatter.

4.4.2 Results

Estimates for the tracer and blank ICs are given in Table 4.5. Although the tracer IC is constrained to be on the mixing line, there are only two physical constraints on its location. First, the isotope ratios that comprise it must not be negative. Second, the proposed IC must have less of the common Pb components than the analysis with the highest ratio of tracer to blank. These two endpoints define a line segment along which the tracer IC must lie, and it will be shown that the location chosen does not influence the value or uncertainty budget of an analysis that has been corrected for both tracer and blank. The tracer IC in Table 4.5 has been arbitrarily chosen to have a composition halfway between the two possible endpoints of this line segment, and its 2σ uncertainty is set to the half-length of the segment.

The line fit algorithm of McLean (2011) outputs uncertainties for a point on the line (the tracer IC) and the slope of the line (the blank IC), given in Table 4.5. The uncertainties in the tracer IC ratios are strongly correlated, as are the blank IC ratios, with correlation coefficients given in Table 4.6. The magnitude of the uncertainties in the tracer IC and their correlation define an uncertainty envelope around the tracer IC that is parallel to the tracer-blank mixing line. One way to see this is that the ratios of the tracer IC uncertainties approximate the blank IC ratios: for instance, the ratio of the $^{208}\text{Pb}/^{205}\text{Pb}$ uncertainty to the $^{206}\text{Pb}/^{205}\text{Pb}$ uncertainty is approximately equal to the $^{206}\text{Pb}/^{204}\text{Pb}$ of the blank.

4.4.3 Application to TIMS Pb measurements

Although the blank and tracer ICs may be expressed separately, both components must be subtracted from routine analyses. Therefore it is their sum, which is constrained to fall along the mixing line, that is of interest. There are two approaches to blank subtraction currently employed for TIMS analyses, used when analyses contain ^{204}Pb masses consistent with total procedural blank measurements (e.g., chemically abraded zircon) or contain initial common Pb (e.g. titanite, apatite) (McLean et al., 2011).

In the first, all ^{205}Pb comes from the tracer and all ^{204}Pb from either the tracer or the blank. The measured and fractionation-corrected $^{204}\text{Pb}/^{205}\text{Pb}$ defines a unique location on the tracer-blank mixing line. The corresponding $^{206}\text{Pb}/^{205}\text{Pb}$, $^{207}\text{Pb}/^{205}\text{Pb}$, and $^{208}\text{Pb}/^{205}\text{Pb}$ on the line are those of the tracer-blank mixture, which are subtracted from the measured, fractionation-corrected ratio and used for isotope dilution (McLean et al., 2011). Both the uncertainties in the mixing line parameters and the measured $^{204}\text{Pb}/^{205}\text{Pb}$ are propagated into the tracer- and blank-corrected ratios.

In the second, the mass of the Pb blank is assumed, generally the average of several spiked total procedural blank analyses, and the estimated masses of tracer and blank are subtracted together from the fractionation-corrected measured IC of the sample. The rest of the common Pb (including ^{204}Pb) is considered part of the sample, so the measured $^{204}\text{Pb}/^{205}\text{Pb}$ is no longer restricted to tracer and blank components. To find determine the moles of a given isotope in the sample, for instance ^{206}Pb , first the moles of total procedural blank is determined (equation 15 of McLean et al., 2011),

$$\text{moles}(^{206}\text{Pb})_{tpb} = \text{moles}(^{205}\text{Pb})_{tpb} \cdot \left[\left(\frac{^{206}\text{Pb}}{^{205}\text{Pb}} \right)_{tpb} - \left(\frac{^{206}\text{Pb}}{^{205}\text{Pb}} \right)_{tr} \right] \quad (4.10)$$

and the total procedural blank is subtracted from a subsequent analysis

$$\text{moles}(^{206}\text{Pb})_{spl} = \text{moles}(^{205}\text{Pb})_{spl} \cdot \left[\left(\frac{^{206}\text{Pb}}{^{205}\text{Pb}} \right)_{spl} - \left(\frac{^{206}\text{Pb}}{^{205}\text{Pb}} \right)_{tr} \right] - \text{moles}(^{206}\text{Pb})_{tpb} \quad (4.11)$$

However, if the tracer IC was on the measured tracer-blank mixing line, but its

location was chosen incorrectly, then its (incorrect) IC could be expressed as

$$\left(\frac{{}^{206}\text{Pb}}{{}^{205}\text{Pb}}\right)'_{tr} = \left(\frac{{}^{206}\text{Pb}}{{}^{205}\text{Pb}}\right)_{tr} + \left(\frac{{}^{206}\text{Pb}}{{}^{204}\text{Pb}}\right)_{bl} \cdot (\Delta\beta) \quad (4.12)$$

where $(\Delta\beta)$ is proportional to the incorrect displacement along the tracer-blank mixing line. Calculating equations (4.10) and (4.11) with $({}^{204}\text{Pb}/{}^{205}\text{Pb})'_{tr}$, the resulting difference between the calculated values of $moles({}^{206}\text{Pb})_{spl}$ is

$$\Delta moles({}^{206}\text{Pb})_{spl} = [moles({}^{205}\text{Pb})_{tpb} - moles({}^{205}\text{Pb})_{tpb}] \cdot (\Delta\beta) \cdot \left(\frac{{}^{206}\text{Pb}}{{}^{204}\text{Pb}}\right)_{bl} \quad (4.13)$$

According to equation (4.13), an incorrect choice of the location for the tracer IC on the tracer-blank mixing line incurs an error that is proportional to the difference in the moles of ${}^{205}\text{Pb}$ added to the sample and to the total procedural blank, or for several total procedural blanks, their mean. Because this parameter is under operator control, any systematic errors from an incorrect tracer IC specification can be reduced or eliminated with careful spiking.

4.5 Determining the U IC of the Tracer with Critical Mixtures

The biggest barrier to making accurate measurements of the IC of an unknown solution, such as the tracer, is the unknown and variable magnitude of isotopic fractionation. Since the tracer contains both ${}^{233}\text{U}$ and ${}^{235}\text{U}$, it cannot be internally corrected for fractionation after mixing with a well-characterized ${}^{233}\text{U}/{}^{236}\text{U}$ or ${}^{238}\text{U}/{}^{235}\text{U}$ solution.

Measurement of a critical mixture (Krogh, 1964; Hofmann, 1971) circumvents this difficulty by utilizing a mixture of an isotopic standard and the tracer at the IC where mixing lines and fractionation lines are parallel. Mixtures of the U isotopic standards SRM U500 and CRM 112a, whose ${}^{238}\text{U}/{}^{235}\text{U}$ were determined against the certified ${}^{233}\text{U}/{}^{236}\text{U}$ of IRMM 3636 in Condon et al. (2010), with the mixed with the same ${}^{233}\text{U}$ - ${}^{235}\text{U}$ solution used to make ET(2)535. Measurements of the pure solution

also provide an additional constraint: they must lie on a fractionation line that goes through the true tracer U IC.

Although the critical mixture idea was formulated using a linear fractionation law, it applies to an exponential fractionation law as well. The trend predicted by variable-magnitude exponential fractionation, which deviates from its linear approximation less than 10ppm over observed isotopic fractionation values, is very close to parallel to the mixing line in the vicinity of the critical mixture. Although the magnitude of isotopic fractionation and the proportions of the mixed

In the same way that data from several constraints on the IC of Pb standards were confederated to calculate the best estimate of several model parameters simultaneously in Section 4.3.2, many measurements of the tracer, measured both on its own and mixed in critical mixture proportions can be combined to constrain the U IC of the tracer. The solution and minimization take a similar form.

4.5.1 Model

The isotopic composition of all critical mixtures and tracer ICs were measured as UO_2 . The most abundant oxygen isotope is ^{16}O , followed by ^{18}O , and their ratio varies during the course of each analysis as ^{16}O becomes more depleted. Therefore ^{233}U , ^{235}U , and ^{238}U were measured at masses 265, 267, and 270, corresponding to UO_2 polyatomic ions with two ^{16}O atoms. The isobaric interference of $^{233}\text{U}^{16}\text{O}^{18}\text{O}$ on $^{233}\text{U}^{16}\text{O}^{16}\text{O}$ depends on the $^{18}\text{O}/^{16}\text{O}$ ratio of the sample, which was monitored by measuring the $^{238}\text{U}^{16}\text{O}^{18}\text{O}$ at mass 272 or, for measurements of pure tracer with little ^{238}U , $^{235}\text{U}^{16}\text{O}^{18}\text{O}$ at mass 269 (McLean et al., 2011). Isobaric interference corrections were made on each cycle, and the mean and standard error of the resulting U ratios represent the best estimate of the fractionated IC of the sample.

Expressing the components that make up a mixture of the ET(2)535 tracer with a standard, such as SRM U500 or CRM 112a,

$$^{233}\text{U}_{tot} = ^{233}\text{U}_{tr}$$

$$235_{tot} = 235_{st} + 235_{bl} + 235_{tr} \quad (4.14)$$

$$238_{tot} = 238_{st} + 238_{bl} + 238_{tr}$$

where *st* denotes the contribution from an isotopic standard, *tr* from the tracer, and *bl* from the blank.

Normalizing all the components to the moles of ^{235}U in the tracer results in

$$233_{tot}/235_{tr} = (233_{tr}/235_{tr})$$

$$235_{tot}/235_{tr} = (235_{st}/235_{tr}) + (235_{bl}/235_{tr}) + (235_{tr}/235_{tr}) \quad (4.15)$$

$$238_{tot}/235_{tr} = (238_{st}/235_{tr}) + (238_{bl}/235_{tr}) + (238_{tr}/235_{tr})$$

Recasting the mixed component ratios ($235_{bl}/235_{tr}$) as $(238_{bl}/235_{tr}) / (238_{bl}/235_{bl})$ and $(235_{st}/235_{tr})$ as $(238_{st}/235_{tr}) / (238_{st}/235_{st})$ yields

$$233_{tot}/235_{tr} = r35t$$

$$235_{tot}/235_{tr} = r85st/r85s + r85bt/r85b + 1 \quad (4.16)$$

$$238_{tot}/235_{tr} = r85st + r85bt + r85t$$

where $r35t$ and $r85t$ are the tracer parameters that are being determined, $r85b$ and $r85s$ are the $^{238}\text{U}/^{235}\text{U}$ of the blank and the isotopic standard, respectively, and $r85st$ and $r85bt$ are the moles of ^{238}U in the standard and blank, respectively, relative to the moles of ^{235}U in the tracer.

Dividing through by $235_{tot}/235_{tr}$ yields the U ratios as commonly measured. In order to equate the true and measured ratios, an exponential fractionation term is added as well.

$$r35m^i = \frac{r35t}{1 + r85bt^i/r85b + r85st^i/r85s} \left(\frac{M_{233}}{M_{235}} \right)^{\beta^i} \quad (4.17)$$

$$r85m^i = \frac{r85bt^i + r85st^i + r85t}{1 + r85bt^i/r85b + r85st^i/r85s} \left(\frac{M_{238}}{M_{235}} \right)^{\beta^i}$$

where M_x denotes the isotopic mass of x and the superscript i denotes variables that change from one analysis to the next. These two equations apply to each measurement of a critical mixture made, regardless of the isotopic standard used. For measurements of the tracer only, which also include a loading blank, the $r85s$ and $r85st$ terms may be dropped.

4.5.2 Algorithm and Results

To solve for the U IC of ET(2)535, we use multiple critical mixture IC measurements with both SRM U500 and CRM 112a as isotopic standards, as well as several measurements of pure tracer alone. All U loads were estimated to be 500 ng, and U blanks 0.1 pg, resulting in a value of 4×10^{-7} for $r85bt$, which is assigned a 100% prior relative uncertainty to account for loading blank mass variability. The $^{238}\text{U}/^{235}\text{U}$ of the blank is estimated to be 137.82, an average of terrestrial sources relative to IRMM 3636 (Hiess et al., in review), with no uncertainty assigned because the magnitude of the blank subtraction is nearly negligible.

As with the Pb standard inter-calibration, a least squares inverse solution to the large system of overdetermined equations in (4.17) created by several measurements is reached by a preconditioned gradient descent method. The unknown variables, in this case $r35t$ and $r85t$, the U IC of the tracer, as well as the sample/spike ratio of each measurement $r85st^i$ and the magnitude of isotopic fractionation β^i are assigned large prior relative uncertainties. This analysis utilizes 14 measurements of SRM U500, 12 of CRM 112a, and 7 of pure tracer made at MIT and NIGL.

The uncertainties in $r85s$ terms, the ICs of the U standards used in the critical mixtures, are treated as a systematic uncertainties. To determine their contribution to the total uncertainty in the tracer U IC, a Monte Carlo algorithm is employed, which is used to test the assumption of that the system is locally linear at its least-squares solution. Monte Carlo realizations of the the $^{238}\text{U}/^{235}\text{U}$ of SRM U500 and CRM 112a are generated by a pseudorandom number generator with the distribution given in Tables 4.1 and 4.2, and the uncertainty of each realization is assumed to be infinitesimally small. The least squares solution is then calculated for 10^4 Monte Carlo

realizations of the U standard ICs, and their variability represents the systematic uncertainty contribution from the U standard ICs. This estimate is combined with the measurement uncertainties derived by solving the system at the maximum likelihood estimate of the U standard ICs to calculate the total uncertainty in the U IC of the tracer (equation 4.3).

The results of the critical mixtures measurement are presented in Table 4.8. The null hypothesis that the Monte Carlo realizations used to calculate the systematic uncertainty contribution are normally distributed is accepted by a K-S test with a p-value of 0.9 for both the $^{233}\text{U}/^{235}\text{U}$ and $^{238}\text{U}/^{235}\text{U}$ of the tracer. This result permits addition of the measurement and systematic uncertainty covariance matrices, the multivariate analog of quadratic uncertainty addition.

4.5.3 Correlation with Sample $^{238}\text{U}/^{235}\text{U}$

In an important development for high-precision U-Pb geo- and cosmochemistry, the $^{238}\text{U}/^{235}\text{U}$ of accessory minerals has been found to vary beyond measurement precision (Hiess et al., in review). In order to determine the $^{238}\text{U}/^{235}\text{U}$ of each accessory mineral, its IC can be measured against IRMM 3636. Thus, in the same way that the U IC of the tracer can be traced to the IC of IRMM 3636, so can a precisely determined $^{238}\text{U}/^{235}\text{U}$ value, and the uncertainties of both are therefore correlated. Since uncertainties in both the tracer and sample U IC are used to determine the total uncertainty budget for a U-Pb date, this correlation must be calculated and included in the uncertainty propagation.

To assess their degree of correlation, the derivative of the mean $^{238}\text{U}/^{235}\text{U}$ for the sample and the tracer IC must be evaluated relative to the IC of IRMM 3636. For the specific accessory phases measured in Hiess et al. (in review), as well as the reported average zircon $^{238}\text{U}/^{235}\text{U}$ of 137.817 ± 0.040 , these derivatives are found in the Supporting Online Materials. For the tracer U ratios, the derivatives are reported in Table 4.7, along with the derivatives of the tracer $^{235}\text{U}/^{205}\text{Pb}$ derived in Section 4.7. The covariance between the tracer and sample ICs can be calculated with a Jacobian

matrix, or matrix of partial derivatives, and a covariance, using the equation

$$\Sigma_{ts} = J^T \Sigma_{3636} J \quad (4.18)$$

where J is a Jacobian matrix that contains the derivatives of the tracer and sample IC with respect to the IC of IRMM 3636, like that presented in Table 4.7, and Σ_{3636} is the covariance matrix for the IRMM 3636 IC. The resulting tracer-sample covariance matrix Σ_{ts} contains, as its off-diagonal components, covariance terms that relate the tracer and sample IC, which can be used in a U-Pb uncertainty propagation algorithm such as McLean et al. (2011).

4.5.4 Sample Fractionation Correction with a ^{233}U - ^{235}U Tracer

The true IC of the mixture is known to lie on a mixing line between the ICs of the tracer and sample, both of which are required for this calculation. For a finite fractionation factor, β , the measured IC lies off of the mixing line, along a fractionation line from the true IC on the mixing line to the measured IC of the sample. Geometrically, fractionation correction entails finding the point on the mixing line whose fractionation line goes through the measured datum. However, at the critical mixture IC used above, the fractionation line is parallel to the mixing line. Any error in the measurement or IC of the sample or tracer (even within arbitrarily small uncertainties) will result in a discrepancy between the mixing line and the measured data that cannot be corrected back to the mixing line along the parallel fractionation line. For ICs close to the critical mixture IC, fractionation lines are subparallel to the mixing line, and small errors (for instance, within assumed uncertainties), can result in large, erroneous extrapolation distances back to the mixing line. For this reason, ^{233}U - ^{235}U tracers are not optimized for ICs near the critical mixture, and the $^{233}\text{U}/^{235}\text{U}$ of the tracer should be manipulated to avoid these sample-tracer ratios. For ET(2)535, U ICs near the critical mixture occur for very young under-spiked samples. For instance, a 3 Ma sample with a $^{206}\text{Pb}/^{205}\text{Pb}$ near 4.25 yields measured $^{238}\text{U}/^{235}\text{U}$ values near 55, magnifying small errors in the measurement or estimate of the

sample $^{238}\text{U}/^{235}\text{U}$. The simplest practical solution is to disregard the double-spike fractionation determination and instead use an average U fractionation value based on past determinations with smaller $^{238}\text{U}/^{235}\text{U}$ values.

4.6 U/Pb Ratios of the Gravimetric Standards

In order to determine the U/Pb ratio of each gravimetric solution, three aliquots of high-purity Pb and U standards were weighed then dissolved in acid in three independent labs, creating solutions whose U/Pb ratios are gravimetrically calibrated. The uncertainty in the U/Pb ratio of each gravimetric solution is a function of the uncertainties in the masses of the standards and their purities. The procedures by which the three gravimetric solutions were mixed in independent labs is included in Condon et al. (2011).

The $^{235}\text{U}/^{205}\text{Pb}$ and $^{202}\text{Pb}/^{205}\text{Pb}$ ratio of the tracer were determined against three separate gravimetric solutions for several reasons. First, the uncertainties due to the mass measurements of the Pb and U metal used to make the solutions, as well as their purities, are major contributions to the uncertainty in the U/Pb ratio of the gravimetric solutions, and therefore the U/Pb ratio of the tracer. Evaluating the mean U/Pb tracer ratio over multiple independently mixed solutions averages out some of this uncertainty. Also, the different $^{206}\text{Pb}/^{238}\text{U}$ ratios of the solutions, ranging from 0.094 for the RP solution to 0.017 for the ET solution, allow for varied sample/tracer ratios for each element when mixed with a tracer with a constant $^{235}\text{U}/^{205}\text{Pb}$. Using multiple sample/tracer ratios and Pb and U ratios for internal fractionation correction allows an additional check for internal consistency between results.

4.6.1 Uncertainty in Mass Determinations

The masses of the Pb and U standards were determined before the metals were dissolved to create the gravimetric solutions. Although care was taken to remove oxidation and surface contamination before weighing on precise balances, each mass measurement has finite uncertainty. Because the ultimate parameter of interest is

the U/Pb ratio of the solutions, any scale bias that is linearly proportional to the measured mass will divide out. Thus we propagate only the uncertainty determined from the reproducibility of successive measurements of calibration weights and the Pb and U metals.

Each measured mass is adjusted for the mass of air that is above the scale during taring and then displaced by the metal when it is weighed. Since the displaced air mass is present during the taring but not during metal measurement, the true mass of the metal is somewhat greater than the measured mass, and may be corrected with the equation

$$mass_{corr} = mass_{meas} \cdot \left(1 + \frac{\rho_{air}}{\rho_{metal}} \right) \quad (4.19)$$

where ρ_{air} and ρ_{metal} are the densities of air and metal being weighed. The density of air ranged between 1.195 and 1.205 kg/m³, calculated using an ideal gas law and the ambient barometric pressure, humidity, and lab temperature on the days the metals were weighed. The densities of metallic U and Pb were calculated using their measured isotopic compositions and standard unit cell parameters. After buoyancy correction, each mass of Pb is heavier by 106 ppm and each U by 63 ppm, increasing the calculated U/Pb ratio of the solution by 43 ± 1 ppm (2σ).

4.6.2 Uncertainty in Purity of Pb Isotopic Standards

Although the purity, or the assay, of both NBS standards and the Puratronic Pb are certified, these measurements are often dated, contain no supporting information, and are quoted with conservative uncertainties (e.g. >99.995%). A purity quotation in this form is unhelpful because there is no expected value or probability density function (pdf) from which to construct confidence intervals or perform uncertainty analysis. In order to better quantify the purity of the Pb isotopic standards used here, the purities of NBS 981, 982, 983, and Puratronic Pb were measured by glow discharge mass spectrometry at the GD-MS facility of the National Research Council (NRC) of Canada. The raw data appears in the electronic supplement.

Analysis by GD-MS entails sputtering a solid sample that forms the cathode of a

steady-state electrical discharge in a enclosure filled with Ar gas, where the sputtered atoms are ionized by an argon plasma. Ionized elements from Li to U are accelerated into a magnetic sector mass spectrometer, where they are separated and their relative abundances are measured, with a detection limit well below 1 ppb (King et al., 1995). Traceability to SI units within stated uncertainties was established at the NRC by analysis of international reference standards (ref?).

Elemental concentrations from GD-MS are reported in two formats. If a significant isobaric interference exists at the same mass to charge ratios as the element of interest, observed as an elevated baseline in the mass scan, then its concentration is reported as '<X ppb'. This result may reasonably be interpreted as a uniform probability distribution function with limits at zero and X ppb. If no significant isobaric interference is detected, then the concentration is reported without the less than symbol, and repeated standard analyses indicate the concentration of each element may be represented as with a triangular pdf, illustrated in Fig. 4-4. The triangular distribution has a mean and mode at the stated concentration, and upper and lower limits at $\pm 50\%$ of the measured value.

The purity of each Pb standard is defined as the difference between unity and the sum of all the impurities. Since the pdfs for the impurities are not Gaussian, uncertainty propagation by quadratic summation is not applicable. Instead, we employ a Monte Carlo approach, where a randomly generated realization from the pdf of each element's concentration is summed to produce a model value for the total impurity concentration. This process was iterated 10^7 times for each standard, and the resulting distribution of purities, normalized to unity, is an accurate estimate of the pdf for the purities. The pdf is closely approximated by a histogram of the Monte Carlo realizations with small bin sizes, illustrated in Fig. 4-4. Because the pdfs of each elemental concentration are symmetric, the pdf of the total impurities is also symmetric, and the maximum likelihood estimate and 95% confidence interval for each standard may be expressed as a symmetric range about the mean, listed in Table 4.9.

4.6.3 Purity of U Isotopic Standards

The purities of the U standards used to make the gravimetric solutions, CRM 112a and CRM 115, have been recently certified to significantly higher precision than the older Pb standards. In a Sept. 2010 revision of the CRM 112a certificate of analysis by the New Brunswick Laboratory, the total impurity concentration is reported as 223 $\mu\text{g/g}$ U, which equates to a purity of 0.999777 g U/g metal, and the total uncertainty in the assay is reported as 0.00006 g U/g metal, expressed as an approximate 95% confidence interval calculated with a $k = 2$ coverage factor. The coverage factor and confidence interval width together imply that the modeled distribution is Gaussian, with a standard deviation of 0.00003 g U/g metal. Likewise, the CRM 115 purity is reported as 0.999770 ± 0.000046 , with the same coverage factor and stated confidence interval, translating to a standard deviation of 0.000023.

4.6.4 Gravimetric U/Pb ratio

The U/Pb ratio of the gravimetric solution is most conveniently expressed as its $^{206}\text{Pb}/^{238}\text{U}$ ratio, which can be determined from the total moles of each isotope present. The moles of ^{206}Pb in the gravimetric solution is

$$\text{moles}(^{206}\text{Pb}) = \frac{\text{mass}(\text{Pb}_{\text{grav}}) \cdot \text{purity}(\text{Pb}_{\text{grav}})}{M_{204} \cdot \left(\frac{^{204}\text{Pb}}{^{206}\text{Pb}}\right)_{\text{gr}} + M_{206} + M_{207} \cdot \left(\frac{^{207}\text{Pb}}{^{206}\text{Pb}}\right)_{\text{gr}} + M_{208} \cdot \left(\frac{^{208}\text{Pb}}{^{206}\text{Pb}}\right)_{\text{gr}}} \quad (4.20)$$

and likewise the moles of ^{238}U in the solution is

$$\text{moles}(^{238}\text{U}) = \frac{\text{mass}(\text{U}_{\text{grav}}) \cdot \text{purity}(\text{U}_{\text{grav}})}{M_{234} \cdot \left(\frac{^{234}\text{U}}{^{238}\text{U}}\right)_{\text{gr}} + M_{235} / \left(\frac{^{238}\text{U}}{^{235}\text{U}}\right)_{\text{gr}} + M_{238}} \quad (4.21)$$

and the $^{206}\text{Pb}/^{238}\text{U}$ ratio of the gravimetric solution is simply the quotient of equations (4.20) and (4.21).

4.7 Gravimetric-Tracer Mixtures

In order to determine the U/Pb ratio of the tracer, expressed as the ratio of two of its enriched isotopes, $^{235}\text{U}/^{205}\text{Pb}$, as well as its $^{202}\text{Pb}/^{205}\text{Pb}$, the tracer was mixed with the series of three gravimetric solutions described in Section 4.6. Measuring the U/Pb ratio of the tracer against the known U/Pb ratio of a gravimetric solution is the inverse of measuring a sample U/Pb ratio with the tracer: the known ICs of the gravimetric solution Pb and U components can be used to fractionation-correct the measured Pb and U tracer/sample ratios, then the known U/Pb ratio of the gravimetric solution is used to determine the U/Pb ratio of the tracer. The small contributions of laboratory blank and non-enriched tracer isotopes complicate the calculation, but as with the Pb standard inter-calibration and U critical mixtures, the resulting mixture can be represented by a system of non-linear equations, and the best estimate of the tracer parameters reached with a non-linear least squares approach.

4.7.1 Equations

Unlike the data used in the Pb isotopic standard inter-calibration in Section 4.3, the gravimetric-tracer Pb measurements, made at both NIGL and MIT, do not monitor the BaPO_2 interference. Because the Pb and U were loaded and run on the same filament, Pb at lower temperature, then U as UO_2 at higher temperature, the Pb was not run to the high temperatures at which BaPO_2 becomes a significant isobaric interference. Additionally, because the ^{204}Pb abundance is always less than an order of magnitude smaller than the other Pb isotopes, it does not contribute meaningfully to tracer calibration calculations, and has been ignored here. These omissions result in a simpler isotopic contribution budget than that used for the Pb standard inter-calibration.

$$^{202}_{tot} = ^{202}\text{Pb}_{tr}$$

$$^{205}_{tot} = ^{205}\text{Pb}_{tr}$$

$$^{206}\text{Pb}_{tot} = ^{206}\text{Pb}_{gr} + ^{206}\text{Pb}_{bl} + ^{206}\text{Pb}_{tr} \quad (4.22)$$

$$^{207}\text{Pb}_{tot} = ^{207}\text{Pb}_{gr} + ^{207}\text{Pb}_{bl} + ^{207}\text{Pb}_{tr}$$

$$^{208}\text{Pb}_{tot} = ^{208}\text{Pb}_{gr} + ^{208}\text{Pb}_{bl} + ^{208}\text{Pb}_{tr}$$

where *tr*, *gr*, and *bl* correspond to the tracer, gravimetric, and blank components, respectively, which sum to the total abundance of each isotope, denoted *tot*.

Normalizing equations (4.22) to ^{205}Pb , which is present in both ET535 and ET2535 tracers but not in the gravimetric solutions, yields

$$\begin{aligned} \frac{^{202}\text{Pb}_{tot}}{^{205}\text{Pb}_{tr}} &= \left(\frac{^{202}\text{Pb}_{tr}}{^{205}\text{Pb}_{tr}} \right) \\ \frac{^{206}\text{Pb}_{tot}}{^{205}\text{Pb}_{tr}} &= \left(\frac{^{206}\text{Pb}_{gr}}{^{205}\text{Pb}_{tr}} \right) + \left(\frac{^{206}\text{Pb}_{bl}}{^{205}\text{Pb}_{tr}} \right) + \left(\frac{^{206}\text{Pb}_{tr}}{^{205}\text{Pb}_{tr}} \right) \\ \frac{^{207}\text{Pb}_{tot}}{^{205}\text{Pb}_{tr}} &= \left(\frac{^{207}\text{Pb}_{gr}}{^{205}\text{Pb}_{tr}} \right) + \left(\frac{^{207}\text{Pb}_{bl}}{^{205}\text{Pb}_{tr}} \right) + \left(\frac{^{207}\text{Pb}_{tr}}{^{205}\text{Pb}_{tr}} \right) \\ \frac{^{208}\text{Pb}_{tot}}{^{205}\text{Pb}_{tr}} &= \left(\frac{^{208}\text{Pb}_{gr}}{^{205}\text{Pb}_{tr}} \right) + \left(\frac{^{208}\text{Pb}_{bl}}{^{205}\text{Pb}_{tr}} \right) + \left(\frac{^{208}\text{Pb}_{tr}}{^{205}\text{Pb}_{tr}} \right) \end{aligned} \quad (4.23)$$

The isotope ratios on the right hand side of equations (4.23) can be re-cast in terms of the isotope ratios of the gravimetric, tracer, and blank components. For instance, the ratio of ^{207}Pb in the blank to ^{205}Pb in the tracer can be expressed as the $^{207}\text{Pb}/^{206}\text{Pb}$ of the blank, derived in Section 4.4, multiplied by the ratio of the moles of ^{206}Pb in the blank to the moles of ^{205}Pb in the tracer. Additionally, the isotope ratios on the left hand side of equations (4.23) can be expressed as measured isotope ratios when the ‘true’ isotope ratios on the right hand side are modified by fractionation correction factor (equation 4.7). With these two substitutions, equations (4.23) become

$$\begin{aligned} \left(\frac{^{202}\text{Pb}}{^{205}\text{Pb}} \right)_m^i &= \left(\frac{^{202}\text{Pb}}{^{205}\text{Pb}} \right)_{tr} \left(\frac{M_{202}}{M_{205} \cdot \gamma_{205}^i} \right)^{\beta_j^i} \\ \left(\frac{^{206}\text{Pb}}{^{205}\text{Pb}} \right)_m^i &= \left[\left(\frac{^{206}\text{Pb}_{gr}}{^{205}\text{Pb}_{tr}} \right)^i + \left(\frac{^{206}\text{Pb}_{bl}}{^{205}\text{Pb}_{tr}} \right)^i + \left(\frac{^{206}\text{Pb}}{^{205}\text{Pb}} \right)_{tr} \right] \left(\frac{M_{206}}{M_{205} \cdot \gamma_{205}^i} \right)^{\beta_j^i} \end{aligned} \quad (4.24)$$

$$\begin{aligned} \left(\frac{{}^{207}\text{Pb}}{{}^{205}\text{Pb}}\right)_m^j &= \left[\left(\frac{{}^{207}\text{Pb}}{{}^{206}\text{Pb}}\right)_{gr} \left(\frac{{}^{206}\text{Pb}_{gr}}{{}^{205}\text{Pb}_{tr}}\right)^i + \left(\frac{{}^{207}\text{Pb}}{{}^{206}\text{Pb}}\right)_{bl} \left(\frac{{}^{206}\text{Pb}_{bl}}{{}^{205}\text{Pb}_{tr}}\right)^i + \left(\frac{{}^{207}\text{Pb}}{{}^{205}\text{Pb}}\right)_{tr}\right] \left(\frac{M_{207} \cdot \gamma_{207}^i}{M_{205} \cdot \gamma_{205}^i}\right)^{\beta_j^i} \\ \left(\frac{{}^{208}\text{Pb}}{{}^{205}\text{Pb}}\right)_m^j &= \left[\left(\frac{{}^{208}\text{Pb}}{{}^{206}\text{Pb}}\right)_{gr} \left(\frac{{}^{206}\text{Pb}_{gr}}{{}^{205}\text{Pb}_{tr}}\right)^i + \left(\frac{{}^{208}\text{Pb}}{{}^{206}\text{Pb}}\right)_{bl} \left(\frac{{}^{206}\text{Pb}_{bl}}{{}^{205}\text{Pb}_{tr}}\right)^i + \left(\frac{{}^{208}\text{Pb}}{{}^{205}\text{Pb}}\right)_{tr}\right] \left(\frac{M_{208}}{M_{205} \cdot \gamma_{205}^i}\right)^{\beta_j^i} \end{aligned}$$

where i denotes a variable that changes from load to load and j denotes a variable that additionally changes from block to block. In this system, the variables corresponding to the blank, tracer, and gravimetric solution Pb ICs are all treated as known variables, with maximum likelihood estimates and uncertainties reported above. The ratio of the blank to the tracer, embodied in the variable $({}^{206}\text{Pb}_{bl}/{}^{205}\text{Pb}_{tr})$, can be estimated from tracer mass used and total procedural blank measurements. Following McLean (2011), the mass-independent fractionation parameterized with the γ terms is assumed to remain constant for each load but vary between loads, and the absolute magnitude of fractionation, β , changes during the course of each analysis. For gravimetric solution mixtures with ET535, the first equation that includes ${}^{202}\text{Pb}$ is ignored.

For the corresponding U measurement, the same system used for the critical mixtures in equations (4.17) applies. Because the magnitude of isotopic fractionation changes dramatically during the long gravimetric-tracer mixture analyses, the parameter β is allowed to change from block to block. The paired Pb and U measurements combine to form a large overdetermined system of equations, with each block of data contributing five or six measured ratios, depending on whether ${}^{202}\text{Pb}$ is present.

Using the gravimetric solution ${}^{206}\text{Pb}/{}^{238}\text{U}$ calculated from equations (4.20) and (4.21), and the $({}^{238}\text{U}_{gr}/{}^{235}\text{U}_{tr})$ from equations (4.17), the term $({}^{206}\text{Pb}_{gr}/{}^{205}\text{Pb}_{tr})$ can be recast as

$$\left(\frac{{}^{206}\text{Pb}_{gr}}{{}^{205}\text{Pb}_{tr}}\right)^i = \left(\frac{{}^{235}\text{U}}{{}^{205}\text{Pb}}\right)_{tr} \cdot \left(\frac{{}^{206}\text{Pb}}{{}^{238}\text{U}}\right)_{gr} \cdot \left(\frac{{}^{238}\text{U}_{gr}}{{}^{235}\text{U}_{tr}}\right)^i \quad (4.25)$$

Substituting the right-hand side expression (4.25) into equations (4.24), along with equations (4.17) for U measurements, creates a system of five equations for ET535 measurements, or six equations for ET2535 measurements that relate measured Pb and U isotope ratios to the gravimetric and tracer solution ICs and their U/Pb ratios.

4.7.2 Algorithm and Results

A total of 46 paired Pb and U measurements were analyzed at NIGL and MIT: 19 with the RP solution, 14 with ET, and 13 with JMM. Of these mixtures, 15 used ET2535 and 31 used ET535. The Pb and U for each mix were loaded together on Re filaments, with the Pb run as a metal and U as UO_2^+ polyatomic ion, described in Condon et al. (2011). Between 100 and 600 independent isotope ratios were measured for each Pb and U solution, provided in the electronic supplement. The mean of each block, defined as 20 consecutive ratio measurements, was evaluated along with the multivariate analog of its squared standard error, the covariance matrix for all isotope ratios divided by $n - 1 = 19$ degrees of freedom. A total of 212 blocks of Pb were measured with ET2535, 579 with ET535, and 644 blocks of U, for a total of $212 \times 4 + 579 \times 3 + 644 \times 2 = 3873$ ratio means.

The most important model parameters in the system described above are the $^{235}\text{U}/^{205}\text{Pb}$ and the $^{202}\text{Pb}/^{205}\text{Pb}$ of the tracer. In order to solve for these, the following variables must be determined for each analysis: the mass-independent fractionation parameters γ_{205} and γ_{207} , and the ratio of gravimetric solution to tracer, parameterized by $(^{238}\text{U}_{gr}/^{235}\text{U}_{tr})$. These variables are assigned initial values based on a linearized solution to the model and assigned diffuse priors. Additionally, the $^{207}\text{Pb}/^{206}\text{Pb}$ and $^{208}\text{Pb}/^{206}\text{Pb}$ of the laboratory blank are known to vary between loads, along with the mass of the Pb and U blanks themselves. The blank IC for for each bead is assigned the prior uncertainty derived in Section 4.4, and the Pb and U blank mass initial values are 0.3 and 0.1 pg, respectively, and given a 100% relative uncertainty, which lets the least-squares algorithm determine the blank mass for each load that best fits the data. Finally, an initial value for the magnitude of isotopic fractionation for each block, β_j^i , was estimated for each Pb and U block using a simple linearized model and assigned a diffuse prior. In total, there are 1759 unknowns constrained by 3873 isotope ratio measurements, so the system itself is overdetermined.

For the gravimetric mixtures, the uncertainties in the gravimetric solution Pb and U ICs, the tracer minor isotope IC, and the U/Pb ratios of the gravimetric

solutions are all treated as systematic uncertainties. To model their effects, Monte Carlo simulations of each were created using the probability distribution functions for the Pb and U ICs of the standards, as well as their purities and mass determinations. Monte Carlo realizations of the gravimetric solution $^{206}\text{Pb}/^{238}\text{U}$ values include the non-Gaussian probability distribution functions for the Pb purities derived from the GD-MS measurements, and thus themselves are not normally distributed. The non-linear least squares model with the data and model parameters described above was solved for 2000 Monte Carlo realizations of the systematic effects.

Testing the distribution of the Monte Carlo realizations of the $^{235}\text{U}/^{205}\text{Pb}$ and the $^{202}\text{Pb}/^{205}\text{Pb}$ of the tracer, the null hypothesis that the distributions are Gaussian is accepted with a p-value of 0.89 and 0.97, respectively. Although the distribution of the Pb standard purities, which are included in this calculation, are not Gaussian, they are overwhelmed by other uncertainties, notably the $^{208}\text{Pb}/^{206}\text{Pb}$ of NBS 981 and the $^{233}\text{U}/^{236}\text{U}$ of IRMM 3636, both of which are assumed to be normally distributed. Therefore, the systematic uncertainties may be combined using equation (4.2) with the measurement uncertainties for the $^{235}\text{U}/^{205}\text{Pb}$ and the $^{202}\text{Pb}/^{205}\text{Pb}$ using equation (4.3). The results are given in Table 4.10.

4.8 Discussion

The highest precision dates produced by U-Pb geochronology, used to calibrate the geologic timescale from the Paleozoic through the Cenozoic, are $^{206}\text{Pb}/^{238}\text{U}$ dates. For samples younger than about 500 Ma, both ^{238}U and ^{206}Pb are more abundant than their ^{235}U and ^{207}Pb counterparts, and the uncertainty in the $^{207}\text{Pb}/^{206}\text{Pb}$ date is still dominated by the blank correction to the small amount of ingrown ^{207}Pb , whose parent isotope ^{235}U is significantly less abundant than ^{238}U . Analysis of the total contribution of the tracer calibration uncertainties to the uncertainty in a $^{206}\text{Pb}/^{238}\text{U}$ date is performed with a simplified data reduction scheme. The only isotopes considered are ^{202}Pb , ^{205}Pb , and ^{206}Pb along with ^{233}U , ^{235}U , and ^{238}U . Using the tracer parameters calculated above along with reasonable sample/tracer ratios and a range

of frequently observed fractionation factors, hypothetical measured ratios corresponding to a range of dates were calculated. For instance, a 100 Ma sample with a sample $^{238}\text{U}/^{235}\text{U}$ ratio of 137.814 and a sample/tracer ($^{238}\text{U}_{spl}/^{235}\text{U}_{tr}$) ratio of 1 will have a measured $^{206}\text{Pb}/^{205}\text{Pb}$ ratio of about 1.56 and $^{238}\text{U}/^{235}\text{U}$ ratio of 0.988, assuming typical magnitudes of isotopic fractionation of 0.2% per u for Pb and 0.1% per u for U.

Using the measured values calculated in this way, a $^{206}\text{Pb}/^{238}\text{U}$ ratio can be calculated by fractionation-correcting the measured $^{206}\text{Pb}/^{205}\text{Pb}$ and $^{238}\text{U}/^{235}\text{U}$ ratios using the $^{202}\text{Pb}/^{205}\text{Pb}$ and $^{233}\text{U}/^{235}\text{U}$ ratios, then utilizing the isotope dilution formula

$$\left(\frac{^{206}\text{Pb}}{^{238}\text{U}}\right)_{spl} = \left(\frac{^{206}\text{Pb}}{^{205}\text{Pb}}\right)_{fc} / \left[\left(\frac{^{238}\text{U}}{^{235}\text{U}}\right)_{fc} \cdot \left(\frac{^{235}\text{U}}{^{205}\text{Pb}}\right)_{tr} \right] \quad (4.26)$$

where *fc* denotes a measured, fractionation-corrected ratio. The $^{206}\text{Pb}/^{238}\text{U}$ can then be used to calculate a date.

There are three pertinent tracer parameters whose uncertainty must be considered: the $^{202}\text{Pb}/^{205}\text{Pb}$, $^{233}\text{U}/^{235}\text{U}$, and $^{235}\text{U}/^{205}\text{Pb}$ ratios. Because both the $^{235}\text{U}/^{205}\text{Pb}$ and the $^{202}\text{Pb}/^{205}\text{Pb}$ derive much of their uncertainty from the a priori uncertainty of the $^{208}\text{Pb}/^{206}\text{Pb}$ of NBS 981, their uncertainties are highly correlated. The result is a relatively large, negative correlation coefficient, which indicates that a positive error in the $^{202}\text{Pb}/^{205}\text{Pb}$ is likely correlated with a negative error in the $^{235}\text{U}/^{205}\text{Pb}$, and vice versa. The two effects partially cancel one another: a higher $^{202}\text{Pb}/^{205}\text{Pb}$ results in a smaller fractionation correction and therefore less apparent ^{206}Pb , but the lower $^{235}\text{U}/^{205}\text{Pb}$ increases the apparent $^{206}\text{Pb}/^{238}\text{U}$ (equation 4.26). Likewise, the $^{235}\text{U}/^{205}\text{Pb}$ and $^{233}\text{U}/^{235}\text{U}$ both depend on the $^{233}\text{U}/^{236}\text{U}$ of IRMM 3636, and therefore their uncertainties are also correlated. In this case, the correlation is positive, and an increase in the tracer $^{233}\text{U}/^{235}\text{U}$ results in a smaller fractionation correction and less apparent ^{238}U , which is partially offset by the larger likely $^{235}\text{U}/^{205}\text{Pb}$.

In this way, the uncertainty correlations between the $^{235}\text{U}/^{205}\text{Pb}$ and both the $^{202}\text{Pb}/^{205}\text{Pb}$ and $^{233}\text{U}/^{235}\text{U}$ act to decrease the overall uncertainty in the $^{206}\text{Pb}/^{238}\text{U}$ date. As Figure 4-5 shows, ignoring the all covariances between the tracer ratios

results in an overestimation of the tracer uncertainty contribution by a factor of almost two. The only published U-Pb uncertainty propagation algorithm to include the required covariance terms is McLean et al. (2011), which permits uncertainty correlations between all tracer parameters. Current version of the ICs and uncertainties of both ET535 and ET2535 are available for download into the associated U-Pb_Redux software package through the EARTHTIME initiative.

4.9 Conclusions

Correct tracer uncertainty propagation is essential to accurate, precise U-Pb isotope dilution geochronology. This contribution presents a measurement model that links first-principles mass and purity measurements to a complete description of the EARTHTIME (^{202}Pb)- ^{205}Pb - ^{233}U - ^{235}U tracer isotopic composition, using a series mixtures between the tracer and gravimetric solutions with known U/Pb ratios and isotopic compositions. The foundation of the tracer calibration depends upon two sets of measurements: the gravimetrically determined $^{208}\text{Pb}/^{206}\text{Pb}$ of NBS 981 and the $^{233}\text{U}/^{236}\text{U}$ of IRMM 3636, and the weights and purities of the the three Pb standards and two U standards used to make three independently calibrated gravimetric solutions. Because the tracer ratios with the strongest influence on U-Pb dates, the $^{202}\text{Pb}/^{205}\text{Pb}$, $^{233}\text{U}/^{235}\text{U}$, and $^{235}\text{U}/^{205}\text{Pb}$ ratios, are mutually dependent on the first-principles measurements, their uncertainties are significantly correlated. This correlation acts to decrease the overall uncertainty contribution to U-Pb dates due to tracer calibration.

The improvement presented here over the commonly assumed tracer calibration uncertainty of ca. 0.1% to <300 ppm represents a significant contribution to the resolution of inter-laboratory comparisons. Other labs using the same algorithms and should be able to collaboratively combine U-Pb data at the sub per-mil level, which approaches modern measurement uncertainties. The converse is also true: a precise tracer calibration is capable of revealing sub-per-mil variation between collaborating laboratories that may be due to previously unrecognized instrument calibration or

laboratory blank biases. Finally, by establishing U-Pb dates in an absolute reference frame, this tracer calibration legitimizes further efforts at inter-calibrating the U decay constants (e.g., Schoene et al., 2006; Mattinson, 2010), as well as the U-Pb and ^{40}Ar - ^{39}Ar systems (e.g., Renne et al., 2010).

4.10 Figure captions

Figure 4-1: Measurements of MIF for the mixtures of Pb isotopic standards and a ^{202}Pb - ^{205}Pb tracer. Data is from Amelin and Davis (2006) along with newer measurements. The red data is from mixtures of NBS 981, green NBS 982, and blue Puratronic Pb. The black cross on the gray 1:1 line is the predicted behavior using a mass-dependent exponential fractionation law. Ellipses are 2σ or $\sim 86\%$ confidence intervals with all sources of uncertainty propagated.

Figure 4-2: Five thousand Monte Carlo simulations of the effect of systematic uncertainties on the best-fit value of $^{208}\text{Pb}/^{206}\text{Pb}$ of NBS 982.

a) Probability plot of all Monte Carlo solutions. An ideal Gaussian distribution with the mean and standard deviation of the Monte Carlo solutions should plot on the diagonal red line.

b) Histogram of Monte Carlo solutions with overlaid Gaussian distribution (red) with the observed mean and standard deviation. Both plots demonstrate that the Monte Carlo solutions are well-approximated by a Gaussian distribution, confirmed by a one-sided K-S test.

Figure 4-3: Measurements of the blank isotopic composition after subtracting the final tracer IC, then propagating measurement and systematic uncertainties. All ellipses are 2σ , or $\sim 86\%$ confidence intervals. The measurement and fractionation uncertainties for each datum are plotted with blue. The covariance ellipse for the discrete dataset is represented by the large red dashed ellipse, which does not account for the scatter in the blank ICs due to measurement uncertainty. The green ellipse is termed the overdispersion, which separates the positively correlated variability in the blank IC from the even more correlated measurement uncertainties.

Figure 4-4: Probability distribution functions for the purity of four commonly used Pb standards, derived by summing elemental abundances measured by GD-MS. The inset shows the probability distribution functions assumed for the individual elements measured. In the presence of isobaric interferences, the true concentration is assumed to be between the measured value and zero, with equal relative probability

along this interval. For a measurement free of isobaric interference, the true concentration is assumed to be within $\pm 50\%$ of the measured value, with the measured value being the most probable.

Figure 4-5: Relative uncertainty contribution (2σ , ppm) to the $^{206}\text{Pb}/^{238}\text{U}$ date from uncertainty in the tracer IC. a) The black line indicates the correct relative uncertainty contribution as a function of $^{206}\text{Pb}/^{238}\text{U}$ date. The red, green, and blue lines show the calculated uncertainty contribution if the covariance terms that belong to the tracer $^{233}\text{U}/^{235}\text{U}$, $^{202}\text{Pb}/^{205}\text{Pb}$, or all tracer variables, respectively, are neglected. b) The tracer contribution to the $^{206}\text{Pb}/^{238}\text{U}$ date uncertainty varies with the magnitude of isotopic fractionation. The shaded region encloses commonly observed values: Pb from 0.1 to 0.3% per u , and U from 0 to 0.2% per u .

Table 4.1: Weighted mean $^{238}\text{U}/^{235}\text{U}$ values and their random, and combined random and systematic uncertainties for the U isotopic standards CRM 112a, CRM 115, and CRM U500 used for tracer calibration. Reported ratios are all fractionation-corrected using IRMM 3636(a) (Verbruggen et al., 2008) for fractionation correction.

	$^{238}\text{U}/^{235}\text{U}$	$\pm 2\sigma^a$	$\pm 2\sigma^b$	MSWD	n (beads)
CRM 112a ^c	137.841	0.011	0.024	1.4	7
CRM 115	491.548	0.039	0.086	0.7	4
CRM U500 ^c	0.999781	0.000077	0.00017	1.0	35

^a propagating only components of uncertainty arising from random effects during measurement

^b propagating components of uncertainty arising from systematic and random effects

^c data from Condon et al. (2010)

Table 4.2: Matrix of correlation coefficients between the uncertainties reported in Table 4.1

	CRM 112a	CRM 115	CRM U500
CRM 112a	1		
CRM 115	0.825	1	
CRM U500	0.914	0.897	1

Table 4.3: Least squares solutions, random, and combined random and systematic uncertainties for the the Pb isotopic standards NBS 981, NBS 982, and Puratronic Pb used for tracer calibration, calculated with data reported in Amelin and Davis (2006)

		wtd. mean	$\pm 2\sigma^a$	$\pm 2\sigma^b$	n (blocks)
981	$^{204}\text{Pb}/^{206}\text{Pb}$	0.0590074	0.0000016	0.000022	160
	$^{207}\text{Pb}/^{206}\text{Pb}$	0.914683	0.000011	0.00015	
	$^{208}\text{Pb}/^{206}\text{Pb}^c$	<i>2.1681</i>	–	<i>0.0008</i>	
982	$^{204}\text{Pb}/^{206}\text{Pb}$	0.0272058	0.0000021	0.000010	160
	$^{207}\text{Pb}/^{206}\text{Pb}$	0.466967	0.000026	0.00008	
	$^{208}\text{Pb}/^{206}\text{Pb}$	1.000249	0.000056	0.00039	
Pur.	$^{204}\text{Pb}/^{206}\text{Pb}$	0.0548861	0.0000044	0.000021	36
	$^{207}\text{Pb}/^{206}\text{Pb}$	0.856720	0.000046	0.00015	
	$^{208}\text{Pb}/^{206}\text{Pb}$	2.10227	0.00011	0.00079	

^a propagating only components of uncertainty arising from random effects during measurement

^b propagating components of uncertainty arising from systematic and random effects

^c value from Catanzao et al. (1968), uncertainty regarded as systematic

Table 4.4: Matrix of correlation coefficients between the uncertainties in the Pb ICs used for tracer calibration. These uncertainties are correlated because they share common sources of uncertainty, largely due to common ratios being used for the fractionation correction. Correlation coefficients close to -1 or 1 indicate a high degree of correlation.

		NBS 981			NBS 982			Puratronic Pb		
		$\frac{^{204}\text{Pb}}{^{206}\text{Pb}}$	$\frac{^{207}\text{Pb}}{^{206}\text{Pb}}$	$\frac{^{208}\text{Pb}}{^{206}\text{Pb}}$	$\frac{^{204}\text{Pb}}{^{206}\text{Pb}}$	$\frac{^{207}\text{Pb}}{^{206}\text{Pb}}$	$\frac{^{208}\text{Pb}}{^{206}\text{Pb}}$	$\frac{^{204}\text{Pb}}{^{206}\text{Pb}}$	$\frac{^{207}\text{Pb}}{^{206}\text{Pb}}$	$\frac{^{208}\text{Pb}}{^{206}\text{Pb}}$
981	$^{204}\text{Pb}/^{206}\text{Pb}$	1								
	$^{207}\text{Pb}/^{206}\text{Pb}$	-0.974	1							
	$^{208}\text{Pb}/^{206}\text{Pb}$	-0.990	0.991	1						
982	$^{204}\text{Pb}/^{206}\text{Pb}$	0.939	-0.960	-0.958	1					
	$^{207}\text{Pb}/^{206}\text{Pb}$	-0.875	0.809	0.846	-0.753	1				
	$^{208}\text{Pb}/^{206}\text{Pb}$	-0.965	0.919	0.950	-0.883	0.943	1			
Pur.	$^{204}\text{Pb}/^{206}\text{Pb}$	0.974	0.958	-0.973	0.933	-0.848	-0.942	1		
	$^{207}\text{Pb}/^{206}\text{Pb}$	-0.941	0.939	0.948	-0.909	0.815	0.909	-0.948	1	
	$^{208}\text{Pb}/^{206}\text{Pb}$	-0.982	0.975	0.988	-0.947	0.850	0.950	-0.986	0.961	1

Table 4.5: Results of linear fit for tracer - blank mixing line

	ET535		ET2535		Pb blank		
	value	$\pm 2\sigma$	value	$\pm 2\sigma$	value	$\pm 2\sigma$	
$^{204}\text{Pb}/^{205}\text{Pb}^a$	0.000090	0.000018	0.000130	0.000050	$^{206}\text{Pb}/^{204}\text{Pb}$	18.41	0.48
$^{206}\text{Pb}/^{205}\text{Pb}$	0.00039	0.00034	0.00093	0.00092	$^{207}\text{Pb}/^{204}\text{Pb}$	15.41	0.29
$^{207}\text{Pb}/^{205}\text{Pb}$	0.00030	0.00028	0.00077	0.00077	$^{208}\text{Pb}/^{204}\text{Pb}$	37.61	1.13
$^{208}\text{Pb}/^{205}\text{Pb}$	0.00074	0.00070	0.0019	0.0019			

^a This value is chosen arbitrarily to be half the distance from a null composition to the analysis with the highest ratio of tracer to blank (see Section 4.4.2).

Table 4.6: Correlation coefficient matrix for ET535 and loading blank Pb IC.

		ET535 Pb IC				blank Pb IC		
		$\frac{^{204}\text{Pb}}{^{205}\text{Pb}}$	$\frac{^{206}\text{Pb}}{^{205}\text{Pb}}$	$\frac{^{207}\text{Pb}}{^{205}\text{Pb}}$	$\frac{^{208}\text{Pb}}{^{205}\text{Pb}}$	$\frac{^{206}\text{Pb}}{^{204}\text{Pb}}$	$\frac{^{207}\text{Pb}}{^{204}\text{Pb}}$	$\frac{^{208}\text{Pb}}{^{204}\text{Pb}}$
ET535	$^{204}\text{Pb}/^{205}\text{Pb}$	1						
	$^{206}\text{Pb}/^{205}\text{Pb}$	0.980	1					
	$^{207}\text{Pb}/^{205}\text{Pb}$	0.989	0.992	1				
	$^{208}\text{Pb}/^{205}\text{Pb}$	0.974	0.987	0.992	1			
blank	$^{206}\text{Pb}/^{204}\text{Pb}$	0	-0.136	-0.076	-0.114	1		
	$^{207}\text{Pb}/^{204}\text{Pb}$	0	-0.103	-0.100	-0.135	0.755	1	
	$^{208}\text{Pb}/^{204}\text{Pb}$	0	-0.099	-0.086	-0.156	0.729	0.864	1

Table 4.7: Derivatives of the U IC of ET(2)535 with respect to IRMM 3636. These values can be used to determine the covariance between a measured $^{238}\text{U}/^{235}\text{U}$ and the tracer, for propagating uncertainty in U-Pb dates.

		ET(2)535		
		$\frac{^{233}\text{U}}{^{235}\text{U}}$	$\frac{^{238}\text{U}}{^{235}\text{U}}$	$\frac{^{235}\text{U}}{^{205}\text{Pb}}$
IRMM3636	$^{233}\text{U}/^{236}\text{U}$	0.6707	0.002907	99.79
	$^{234}\text{U}/^{236}\text{U}$	-0.001262	4.209×10^{-6}	-0.1951
	$^{235}\text{U}/^{236}\text{U}$	-0.8686	0.005051	-121.8
	$^{238}\text{U}/^{236}\text{U}$	0.4466	-0.001505	68.93

Table 4.8: The U isotopic composition of ET(2)535 from the critical mixture experiment. The tracer was mixed with CRM 112a and SRM U500, whose ICs, uncertainties, and correlation coefficient are given in Section 4.3.1.

	MLE	$\pm 2\sigma^a$	$\pm 2\sigma^b$	ρ^c
$^{233}\text{U}/^{235}\text{U}$	0.995062	0.000009	0.00011	-0.599
$^{238}\text{U}/^{235}\text{U}$	0.00307993	0.00000064	0.00000080	

^a propagating only components of uncertainty arising from random effects during measurement

^b propagating components of uncertainty arising from systematic and random effects

^c correlation coefficient between $^{233}\text{U}/^{235}\text{U}$ and $^{238}\text{U}/^{235}\text{U}$, with all uncertainties propagated

Table 4.9: Purities of Pb isotopic standards measured by glow discharge mass spectrometry, with estimated symmetric 95% confidence intervals

	purity	95%CI
NBS 981	0.9999986	± 0.0000009
NBS 982	0.9999767	± 0.0000072
NBS 983	0.9999862	± 0.0000033
Puratronic	0.9999890	± 0.0000047

Table 4.10: Results of the gravimetric solution - tracer mixtures.

	MLE	$\pm 2\sigma^a$	$\pm 2\sigma^b$	ρ^c
$^{202}\text{Pb}/^{205}\text{Pb}$	0.999239	0.000019	0.00053	-0.915
$^{235}\text{U}/^{205}\text{Pb}$	100.2329	0.0022	0.047	

^a propagating only components of uncertainty arising from random effects during measurement

^b propagating components of uncertainty arising from systematic and random effects

^c correlation coefficient between $^{202}\text{Pb}/^{205}\text{Pb}$ and $^{235}\text{U}/^{205}\text{Pb}$, with all uncertainties propagated

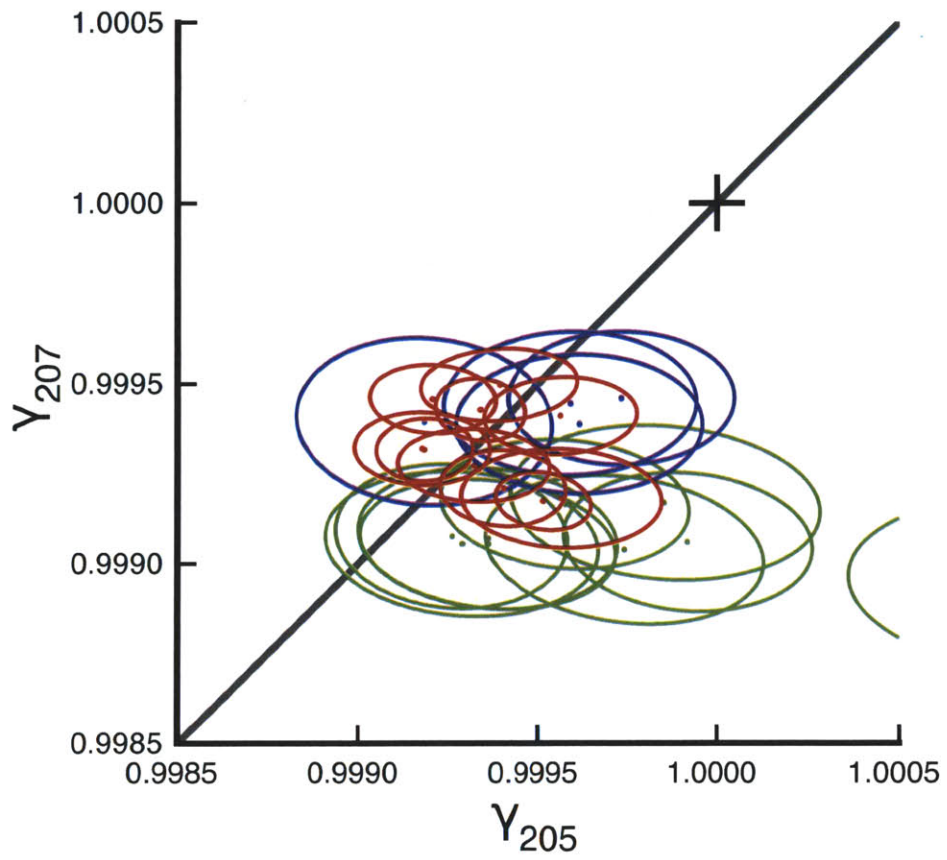


Figure 4-1: Mass independent fractionation of Pb.

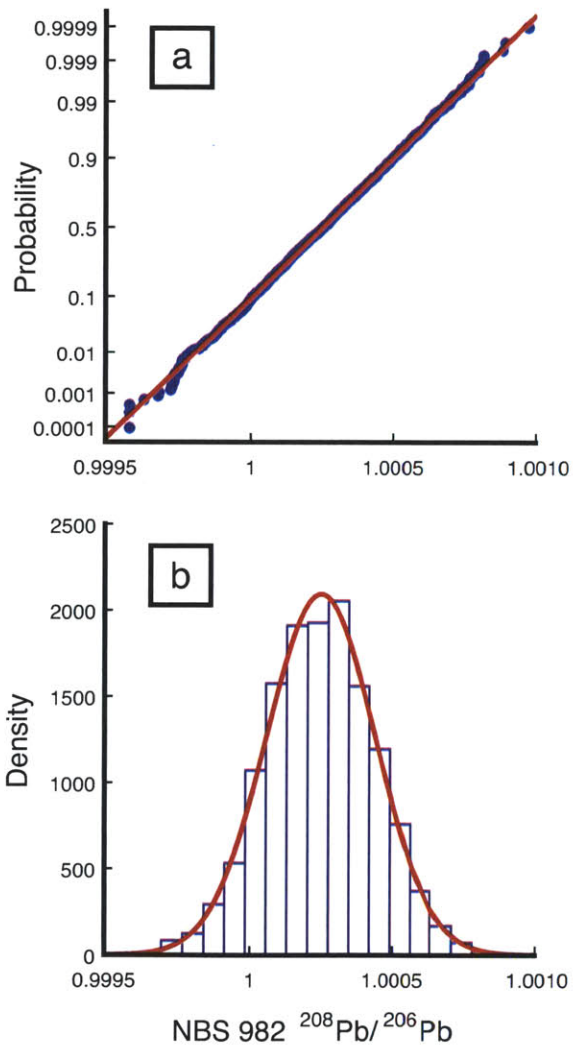


Figure 4-2: Monte Carlo simulations of the best-fit value of $^{208}\text{Pb}/^{206}\text{Pb}$ of NBS 982.

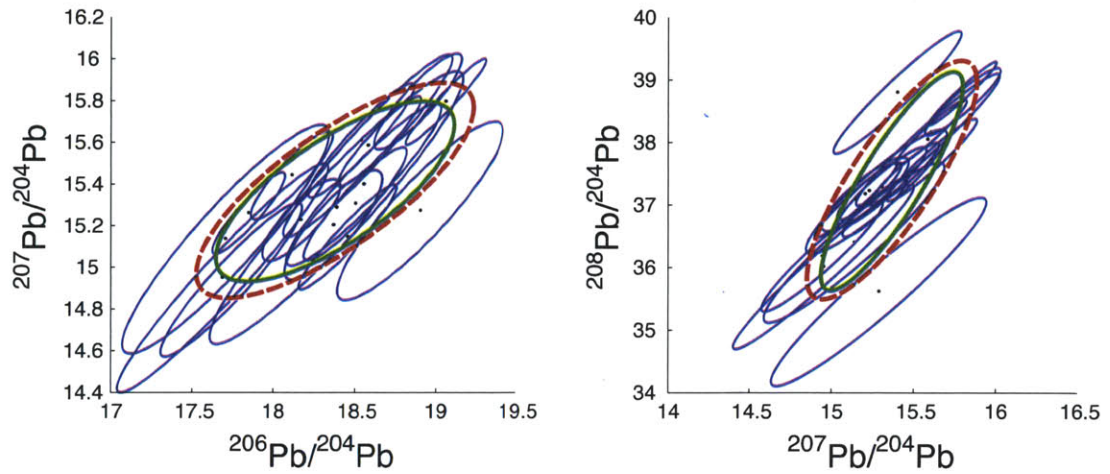


Figure 4-3: Measurements of the laboratory Pb blank isotopic composition.

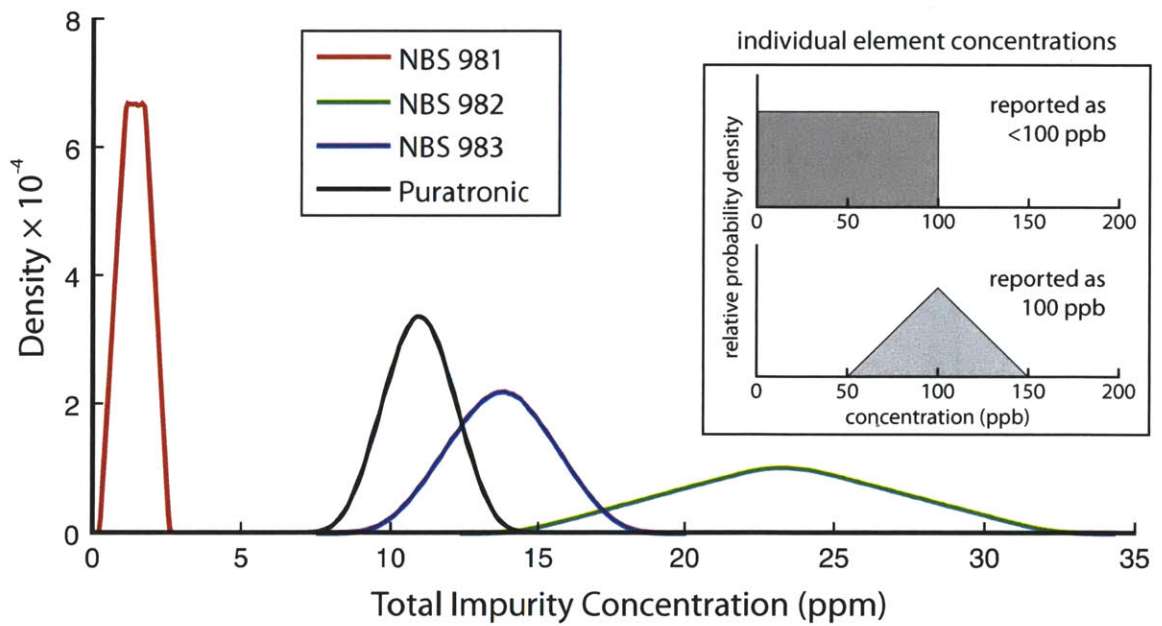


Figure 4-4: Probability distribution functions for the purity of four commonly used Pb standards.

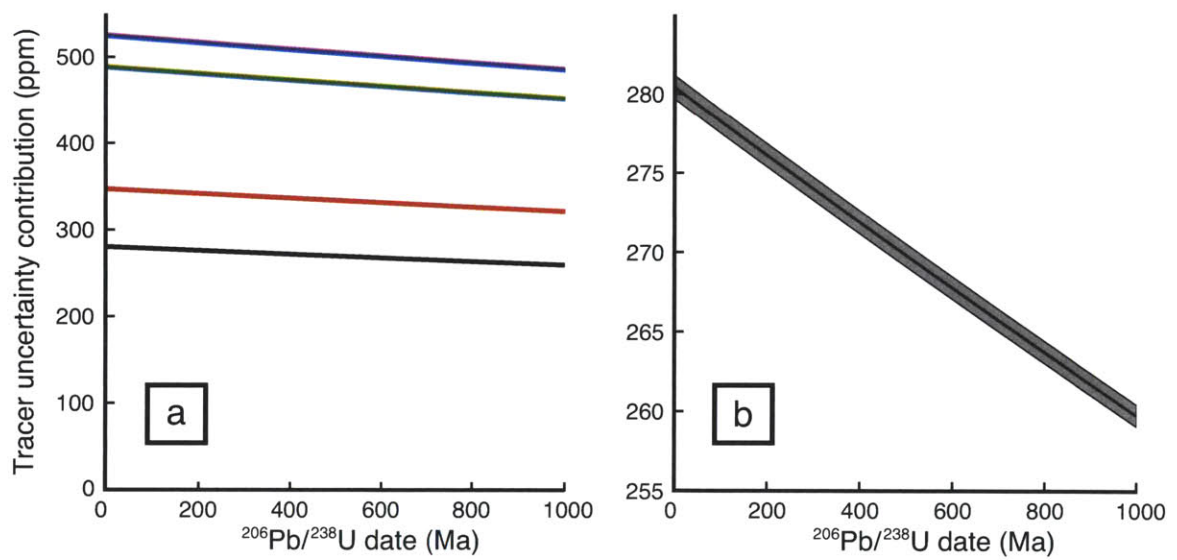


Figure 4-5: Relative uncertainty contribution (2σ , ppm) to the $^{206}\text{Pb}/^{238}\text{U}$ date from uncertainty in the tracer IC.

Chapter 5

Exhumation of the North Cascades core coincident with rapid sedimentation in adjacent nonmarine basins

Abstract

New high-precision zircon U-Pb geochronology demonstrates that igneous intrusion and ductile deformation in the North Cascades metamorphic core was ongoing during initiation and rapid infilling of proximal thick nonmarine basins. The youngest U-Pb dates from the crystalline core approximately coincide with ^{40}Ar - ^{39}Ar cooling dates of biotite, muscovite, and hornblende, consistent with rapid cooling. Taken together, available age constraints imply a dynamic relationship between rapid basin development and exhumation of the North Cascades core, consistent with a degree of coupling between the upper and lower crust during the major plate transition to the modern Cascades arc.

5.1 Introduction

The North Cascades metamorphic core is the southern terminus of the Coast Plutonic Complex, a 100 km wide belt of Cretaceous to Tertiary plutons and heterogeneous gneisses that parallels the western margin of North America through Canada and into southern Alaska. Since ca. 100 Ma, the North Cascades and the western Cordillera have shared a history of oblique subduction, west-vergent thrust stacking, and arc magmatism (e.g., Rubin et al., 1990). These crustal processes combined to yield thickened crust (speculated Moho depths of ≥ 55 km) in the late Cretaceous arc (Miller and Paterson, 2001). Subsequent episodic transtension and transpression are expressed in part by faults with complex dip-slip histories, such as the Straight Creek, Entiat, Leavenworth, and Ross Lake faults and the Dinkleman Decollement (Tabor et al., 1987, 2003). It has long been recognized that exhumation of the North Cascades metamorphic core was broadly coeval with sediment accumulation in the thick fluvial basins that flank it (Haugerud et al., 1991). A major unresolved question in the geologic history of the North Cascades is how the exhumation and sediment accumulation are related. High precision U-Pb geochronology provides an effective tool for testing temporal relationships, and by extension cause-and-effect hypotheses. Modern (2σ) uncertainties for zircon $^{206}\text{Pb}/^{238}\text{U}$ dates at ca. 50 Ma are often less than 0.1%, or better than ± 50 kyr, capable of resolving closely spaced events in the shallow and deep crust.

5.2 Geologic Setting

The North Cascades metamorphic core is dissected by the brittle, high-angle Entiat fault into the Wenatchee block to the southwest and the Chelan block to the northeast (Fig. 5-1b). The two blocks have different thermal histories: while the Chelan block was metamorphosed and intruded throughout 96-45 Ma arc magmatism and has Eocene ^{40}Ar - ^{39}Ar cooling ages, the Wenatchee block records only Cretaceous magmatism (Tabor et al., 1987). The Skagit Gneiss (Fig. 5-1b) occupies much of the

Chelan block and is composed of heterogeneous gneisses with peak pressures up to 9-10 kbar (e.g., Whitney, 1992) juxtaposed against terranes of amphibolite facies and lower (Misch, 1966). These rocks are thought to once have been part of a thick (Miller and Paterson, 2001) contractional arc of a wide Andean-type plateau Whitney et al. (2004). A recently developed contrarian view (Hildebrand, 2009) is that the Coast Plutonic Complex magmatism is the result of west-dipping slab failure and breakoff before the modern east-dipping subduction regime.

Contemporaneous with ductile deformation and continued magmatism in the North Cascades core is the deposition of thick sequences of non-marine sedimentary rocks in a series of fault-bounded transtensional basins, including the Chuckanut basin in northwestern Washington, the Swauk basin immediately to the south of the metamorphic core, and the Chumstick basin, which occupies a graben-like structure between the Wenatchee and Chelan blocks. Zircon fission track dates (Gresens et al., 1981; Johnson, 1984) and palynology indicate that the basins are Eocene, but all three basins lack a high-precision chronology. Subsidence history is difficult to determine from present-day fault configurations due to complex syndeformational fault rotation, but may be assessed by dating volcanic ash layers within the basins, which may then be compared with dates from the Cascades core.

5.3 U-Pb dates in the Skagit Gneiss

In order constrain the relationship between earlier deformation and metamorphism and to identify intrusions and fabrics involved in exhumation, 1:24K scale mapping was carried out on in three across-strike transects in the Skagit Gneiss. Using field and cross-cutting relationships, the youngest orthogneiss bodies were singled out for zircon U-Pb dating. U-Pb dates of zircons from orthogneisses and other non-deformed intrusive bodies constrain protolith crystallization. Modern high-precision (<0.1% relative uncertainty) U-Pb dates of complex igneous intrusions frequently exhibit resolvable variability, on the order of 10s to 100s of kyr, interpreted as a xenocrystic or autocrystic component (e.g., Matzel et al., 2006). However, the youngest zircon

date, after pre-treatment by chemical abrasion techniques to reduce Pb loss (Mattinson, 2005b), can be interpreted reliably as a maximum crystallization date. Although early reconnaissance geochronology in the Skagit Gneiss (Mattinson, 1972; Miller and Bowring, 1990) indicated largely Cretaceous crystallization followed by Eocene cooling, detailed geochronology has revealed significant Eocene magmatism and ductile deformation following a period of Paleocene quiescence. Our new dates extend the full length of the Skagit Gneiss and are described here from south to north.

The Rainbow Falls orthogneiss and the Purple Creek orthogneiss are hornblende-biotite tonalitic gneisses from the central Skagit gneiss (Michels, 2008). Each contains a penetrative solid-state foliation and lineation defined by elongate quartz and aligned biotite and hornblende crystals. Field relationships indicate that both bodies intrude older poly-deformed tonalitic gneiss. The youngest $^{206}\text{Pb}/^{238}\text{U}$ zircon dates from the Rainbow Falls orthogneiss define a weighted mean of 48.160 ± 0.031 Ma, and the four youngest dates from the Purple Creek orthogneiss define a weighted mean of 49.385 ± 0.032 Ma (Fig. 5-1d). Both samples contain older zircons likely inherited from older intrusions, and youngest dates are interpreted to reflect crystallization of the parent bodies.

In the northern Skagit Gneiss, two samples with Eocene crystallization dates exhibit solid-state deformation. In the northwestern Skagit Gneiss, a sheet of mylonitic hornblende-biotite tonalite ‘flecked gneiss’ (Miller et al., 2009) contains plagioclase phenocrysts cored by small euhedral sphene. Contacts between the flecked gneiss and its host tonalitic orthogneiss are subparallel to regional foliation, suggesting they were deformed together during regional folding. Three $^{206}\text{Pb}/^{238}\text{U}$ zircon dates agree with a weighted mean of 47.210 ± 0.020 Ma, with an MSWD of 0.70. The granodioritic Diablo Lake orthogneiss (Wintzer, 2009) outcrops as a ~ 1 km² body in the north-central Skagit Gneiss, and as late dikes intruding older polydeformed gneisses nearby. Elongate quartz grains and aligned biotite and plagioclase define a prominent lineation. Three overlapping zircon $^{206}\text{Pb}/^{238}\text{U}$ dates have a weighted mean of 44.856 ± 0.023 Ma, with a MSWD of 2.3.

5.4 U-Pb dates in non-marine basins

Volcanic tuffs have been described in the Chuckanut, Swauk, and Chumstick basins (Evans and Johnson, 1989; McClincy, 1986). Zircon $^{206}\text{Pb}/^{238}\text{U}$ data can be used to precisely constrain the depositional dates of the tuffs, but only five of the 20 sampled tuffs contained populations of Eocene zircons interpreted as pyroclastic in origin. Other sampled tuffs, which have been mapped over large aerial extent, contain zircons whose dates exceed available constraints, and are therefore detrital or from reworked volcanics. Detrital zircon data from these tuffs are included in the supplementary data.

The Chuckanut Formation is composed of up to 5000-7000 m of nonmarine sandstone, mudstone, and conglomerate (Johnson, 1984), interpreted as fluvial infill during Eocene regional extension and subsidence (Evans and Ristow, 1994). The oldest member of the Chuckanut Formation, the Bellingham Bay member (Fig. 5-1c), contains a single recognized lithic tuff. Eleven new zircon $^{206}\text{Pb}/^{238}\text{U}$ dates range from 56.7 to 57.5 Ma, varying significantly within measurement uncertainties, with no analyses younger than 56.69 ± 0.13 Ma. We interpret the spread of zircon dates to reflect protracted zircon growth history in the volcanic source of the tuff, and the youngest date, which overlaps the five youngest zircon analyses within 2σ uncertainty to reflect the best estimate of the time of deposition.

The Swauk Formation comprises a maximum thickness of 4800 m of arkosic sandstone, shale and conglomerate in the Swauk basin between the Straight Creek and Leavenworth fault zones (Tabor et al., 1984). Sandstones in the upper Swauk formation are interbedded with thick silicic tuffs, the Silver Pass Volcanics, that are primarily dacitic to andesitic in composition and reach a maximum thickness of ~ 1800 m at the type locality of Silver Pass. A sample of welded ash flow tuff collected at Silver Pass exhibits complex zircon systematics, with a ~ 1 Ma range in zircon dates from 52.2 to 51.2 Ma. The youngest four analyses overlap with a weighted mean of 51.345 ± 0.032 Ma with a MSWD of 0.92, interpreted as the best estimate of the time of eruption.

Farther east, adjacent to the Cascades core, the Chumstick Formation is a fault-bounded sequence of interbedded sandstone, conglomerate, and shale (Gresens et al., 1981), and contains abundant tuffs interbedded with continental fluvial and lacustrine sediments (McClincy, 1986). Two ashes from the Mission Creek and Clark Canyon tuffs yield tight populations of $^{206}\text{Pb}/^{238}\text{U}$ zircon dates of 48.169 ± 0.021 , and 47.976 ± 0.016 Ma (Fig. 5-1d).

5.5 Discussion

New U-Pb dates of deformed orthogneiss bodies encompass an episode of Eocene magmatism that straddles a time-transgressive transition from hot, ductile mid-crustal rocks to an exhumed upper crustal section intruded by Eocene plutons that record upper-crustal pressures. Ductile deformation in the southern Skagit Gneiss was locally complete by the intrusion of the non-deformed ca. 49 Ma Sunrise Lake pluton and the ca. 48 Ma Cooper Mountain batholith. In the northern Skagit, the ca. 48 Ma Golden Horn batholith displays no solid-state fabric and rapid cooling is dated by ca. 48-45 Ma hornblende and biotite cooling ages in the gneiss complex (e.g., Wernicke and Getty, 1997; Tabor et al., 2003). Thus the relatively young orthogneiss dates reflect maximum ages of local rather than regional strain fields. However, the late magmatism overlaps the regional ^{40}Ar - ^{39}Ar cooling ages, implying that, at least in a limited sense, the Cascades arc was still active during the transition to unroofing and exhumation.

The thickness of the Chumstick stratigraphic section between the Mission Creek and Clark Canyon tuffs is estimated to be ca. 3000 m (McClincy, 1986; Evans, 1991). Although these estimates are complicated by local faulting and limited outcrop of continuous sections, an estimated age difference of 193 ± 38 kyr yields an average sediment accumulation rate of 15 mm/yr during this interval. Furthermore, the Swauk and Chumstick tuffs also pre-date basin-wide folding events. In the Swauk basin, the folding must occur before the intrusion of the 47 ± 1 Ma Teanaway basalt flows and dikes.

The best previous date for the Chuckanut basin was a 49.9 ± 1.2 Ma zircon fission track analysis (Johnson, 1984) of the same tuff from Clayton beach, about 1225 m above the base of the Chuckanut Drive section of the Bellingham Bay Member (Breedlovestrout, 2010). Adopting the new, older age of 56.7 ± 0.1 Ma implies that the Chuckanut basin contains the Paleocene-Eocene boundary, at ca. 55.8 Ma (Charles et al., 2011). This revises downward estimated ages for the abundant floral and vertebrate faunal assemblages preserved in the Chuckanut, which record evidence for humid tropical forests as well as bird, reptile, and mammal tracks (Mustoe et al., 2007).

5.6 Conclusions

During a relatively short interval (55-45 Ma), the crystalline core of the North Cascades experienced a late episode of magmatism and ductile deformation, followed closely by rapid exhumation that was coeval with basin initiation and subsidence, as well as brittle extension outside the metamorphic core. To a first approximation, exposure of the metamorphic core of the North Cascades resembles the extensional core complexes of the Omineca belt farther east.

Figure 5-1

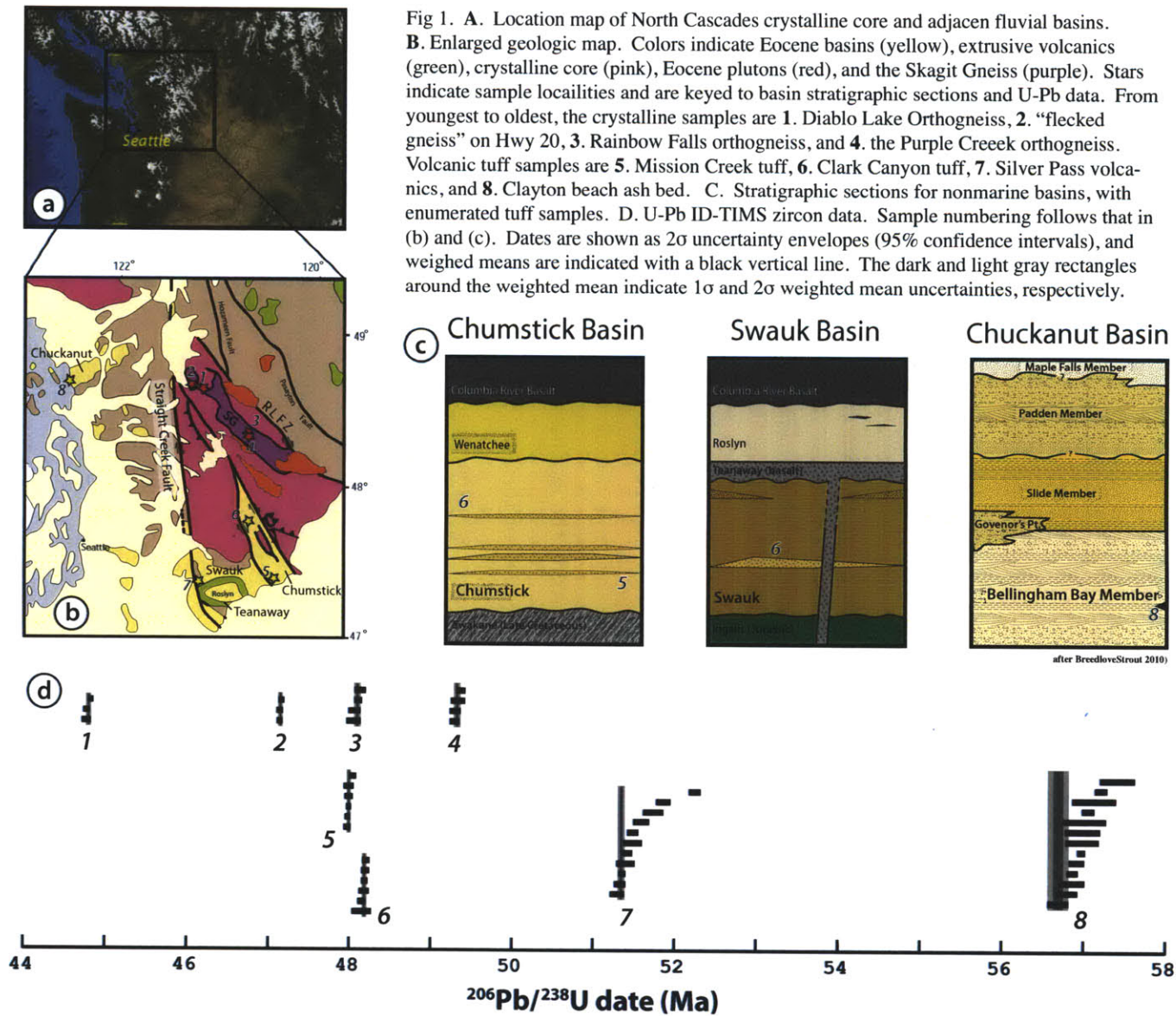


Table 5.1: U-Pb Data Table 1

	Isotopic Dates (Ma) ^a				Composition			Isotope Ratios							
	$\frac{^{206}\text{Pb}^b}{^{238}\text{U}}$	$\pm 2\sigma$	$\frac{^{207}\text{Pb}}{^{235}\text{U}}$	$\pm 2\sigma$	Pb _c ^c (pg)	$\frac{\text{Pb}^*d}{\text{Pb}_c}$	$\frac{\text{Th}^e}{\text{U}}$	$\frac{^{206}\text{Pb}^f}{^{204}\text{Pb}}$	$\frac{^{206}\text{Pb}^{ag}}{^{238}\text{U}}$	$\pm 2\sigma\%$	$\frac{^{207}\text{Pb}^g}{^{235}\text{U}}$	$\pm 2\sigma\%$	ρ^h	$\frac{^{207}\text{Pb}^g}{^{206}\text{Pb}}$	$\pm 2\sigma\%$
<i>NMNC 366-2: Chumstick Formation, Clark Canyon tuff</i>															
z1	47.956	0.041	48.12	0.33	0.85	18	0.47	1118	0.0074669	0.086	0.04853	0.71	0.545	0.04714	0.66
z2	47.976	0.061	47.93	0.87	0.95	7	0.49	461	0.0074700	0.13	0.04833	1.9	0.654	0.04693	1.8
z7	47.975	0.052	48.36	0.55	0.53	12	0.49	759	0.0074699	0.11	0.04878	1.2	0.514	0.04736	1.1
z10	47.975	0.031	48.01	0.23	0.54	27	0.52	1627	0.0074698	0.065	0.04841	0.49	0.367	0.04701	0.47
z11	48.027	0.040	48.28	0.24	0.34	25	0.43	1537	0.0074779	0.083	0.04870	0.52	0.527	0.04723	0.48
z12	47.959	0.032	48.12	0.16	0.50	40	0.60	2321	0.0074674	0.067	0.04853	0.35	0.327	0.04713	0.33
<i>NC-203: Chuckanut Formation, Clayton Beach ash</i>															
c	69.80	0.45	75.6	5.2	1.05	2	0.31	161	0.010887	0.65	0.0773	7.2	0.426	0.0516	7.0
f	57.13	0.27	54.5	3.2	0.40	3	0.48	200	0.008901	0.47	0.0551	6.1	0.338	0.0450	5.9
g	56.99	0.21	58.7	2.5	0.39	4	0.40	244	0.008879	0.38	0.0595	4.4	0.253	0.0487	4.3
j	75.475	0.083	75.22	0.62	0.37	34	0.26	2193	0.011777	0.11	0.07690	0.85	0.605	0.04742	0.79
k	61.27	0.11	60.93	0.99	0.22	11	0.36	730	0.009550	0.18	0.0618	1.7	0.392	0.04704	1.6
l	56.69	0.13	57.5	1.1	0.24	11	0.46	675	0.008833	0.23	0.0582	1.9	0.523	0.04790	1.8
m	57.210	0.075	57.6	1.2	0.19	10	0.35	668	0.008914	0.13	0.0583	2.2	0.280	0.0476	2.2
n	56.970	0.048	56.98	0.43	0.23	26	0.59	1532	0.0088766	0.085	0.05773	0.78	0.260	0.04724	0.77
o	56.862	0.066	57.19	0.50	0.28	22	0.35	1435	0.008860	0.12	0.05794	0.89	0.520	0.04752	0.84
p	57.056	0.075	56.85	0.73	0.35	13	0.46	832	0.008890	0.13	0.05759	1.3	0.394	0.04706	1.3
q	56.98	0.20	58.2	2.6	0.53	4	0.57	241	0.008878	0.36	0.0590	4.6	0.271	0.0483	4.5
s	58.58	0.16	59.6	1.8	0.57	5	0.30	360	0.009129	0.27	0.0605	3.2	0.191	0.0481	3.1
u	57.41	0.21	57.4	2.6	0.62	4	0.58	230	0.008945	0.37	0.0582	4.7	0.261	0.0473	4.6
v	56.86	0.16	57.0	1.9	0.27	5	0.35	311	0.008859	0.27	0.0577	3.5	0.291	0.0474	3.4
w	56.913	0.094	57.22	0.87	0.43	11	0.49	690	0.008868	0.17	0.05797	1.6	0.368	0.04749	1.5
zy	57.01	0.26	56.7	3.7	0.31	2	0.31	139	0.008883	0.46	0.0574	6.8	0.747	0.0470	6.4
zz	56.80	0.13	56.5	1.6	0.39	4	0.46	290	0.008850	0.23	0.0573	2.9	0.781	0.0470	2.8

^a Isotopic dates calculated using the decay constants $\lambda_{238} = 1.55125 \times 10^{-10}$ and $\lambda_{235} = 9.8485 \times 10^{-10}$ of Jaffey et al., (1971).

^b Corrected for initial Th/U disequilibrium using radiogenic ^{208}Pb and $\text{Th}/\text{U}_{\text{magma}} = 4$.

^c Total mass of common Pb.

^d Ratio of radiogenic Pb (including ^{208}Pb) to common Pb.

^e Th contents calculated from radiogenic ^{208}Pb and the Th-corrected $^{206}\text{Pb}/^{238}\text{U}$ date.

^f Measured ratio corrected for fractionation and tracer contribution only.

^g Measured ratios corrected for fractionation, tracer, and blank.

^h Correlation coefficient between Th-corrected $^{206}\text{Pb}/^{238}\text{U}$ and $^{207}\text{Pb}/^{235}\text{U}$ ratios.

Table 5.2: U-Pb Data Table 2

	Isotopic Dates (Ma) ^a				Composition			Isotope Ratios							
	$\frac{^{206}\text{Pb}^b}{^{238}\text{U}}$	$\pm 2\sigma$	$\frac{^{207}\text{Pb}}{^{235}\text{U}}$	$\pm 2\sigma$	Pb _c ^c (pg)	Pb* ^d / Pb _c	Th ^e / U	$\frac{^{206}\text{Pb}^f}{^{204}\text{Pb}}$	$\frac{^{206}\text{Pb}^{ag}}{^{238}\text{U}}$	$\pm 2\sigma\%$	$\frac{^{207}\text{Pb}^g}{^{235}\text{U}}$	$\pm 2\sigma\%$	ρ^h	$\frac{^{207}\text{Pb}^g}{^{206}\text{Pb}}$	$\pm 2\sigma\%$
<i>NC-190: Swauk Formation: Silver Pass volcanics</i>															
z1	51.332	0.070	51.24	0.58	0.55	12	0.33	753	0.007995	0.14	0.05176	1.2	0.599	0.04705	1.1
z3	51.40	0.11	51.8	1.2	0.65	6	0.44	391	0.008006	0.22	0.0524	2.3	0.423	0.0475	2.2
z4	52.249	0.073	54.32	0.63	0.42	12	0.35	768	0.008138	0.14	0.05495	1.2	0.572	0.04907	1.1
z5	51.299	0.086	51.65	0.58	0.94	13	0.48	786	0.007989	0.17	0.05218	1.2	0.457	0.04746	1.1
z6	51.74	0.12	52.5	1.1	0.93	7	0.33	440	0.008059	0.24	0.0531	2.1	0.594	0.04785	2.0
z7	51.595	0.098	52.1	1.2	0.63	5	0.27	353	0.008036	0.19	0.0526	2.4	0.711	0.0476	2.3
z8	51.359	0.042	51.56	0.32	0.66	18	0.31	1129	0.0079989	0.082	0.05209	0.64	0.572	0.04732	0.60
z9	51.49	0.11	50.9	1.3	0.56	5	0.22	328	0.008019	0.22	0.0515	2.5	0.750	0.0466	2.4
z13	51.422	0.061	51.55	0.48	0.45	15	0.32	935	0.0080087	0.12	0.05208	0.96	0.503	0.04726	0.91
z14	51.491	0.068	52.29	0.68	0.37	11	0.26	712	0.008019	0.13	0.05285	1.3	0.547	0.04789	1.3
z15	51.864	0.089	53.0	1.2	0.37	7	0.28	462	0.008078	0.17	0.0536	2.2	0.709	0.0482	2.1
<i>STC62-1: Chumstick Formation, Mission Creek tuff</i>															
z1	48.136	0.048	48.26	0.75	0.31	14	0.37	876	0.0074950	0.099	0.04867	1.6	0.747	0.04719	1.5
z2	48.190	0.044	48.41	0.27	0.39	28	0.59	1670	0.0075035	0.092	0.04883	0.58	0.256	0.04729	0.56
z3	48.180	0.050	48.15	0.50	0.33	13	0.38	838	0.0075020	0.10	0.04857	1.1	0.714	0.04705	0.98
z4	48.169	0.040	47.99	0.43	0.37	16	0.49	983	0.0075002	0.082	0.04840	0.92	0.564	0.04689	0.87
z6	68.384	0.050	68.30	0.26	0.57	38	0.39	2370	0.0106645	0.074	0.06958	0.39	0.424	0.04739	0.37
z7	48.164	0.063	48.20	0.75	0.57	11	0.43	708	0.0074994	0.13	0.04862	1.6	0.344	0.04711	1.6
z8	48.13	0.12	48.0	1.5	0.66	5	0.55	341	0.007495	0.25	0.0484	3.2	0.286	0.0470	3.2

^a Isotopic dates calculated using the decay constants $\lambda_{238} = 1.55125 \times 10^{-10}$ and $\lambda_{235} = 9.8485 \times 10^{-10}$ of Jaffey et al., (1971).

^b Corrected for initial Th/U disequilibrium using radiogenic ^{208}Pb and $\text{Th}/\text{U}_{\text{magma}} = 4$.

^c Total mass of common Pb.

^d Ratio of radiogenic Pb (including ^{208}Pb) to common Pb.

^e Th contents calculated from radiogenic ^{208}Pb and the Th-corrected $^{206}\text{Pb}/^{238}\text{U}$ date.

^f Measured ratio corrected for fractionation and tracer contribution only.

^g Measured ratios corrected for fractionation, tracer, and blank.

^h Correlation coefficient between Th-corrected $^{206}\text{Pb}/^{238}\text{U}$ and $^{207}\text{Pb}/^{235}\text{U}$ ratios.

Table 5.3: U-Pb Data Table 3

	Isotopic Dates (Ma) ^a				Composition			Isotope Ratios							
	$\frac{^{206}\text{Pb}^b}{^{238}\text{U}}$	$\pm 2\sigma$	$\frac{^{207}\text{Pb}}{^{235}\text{U}}$	$\pm 2\sigma$	Pb _c ^c (pg)	$\frac{\text{Pb}^{*d}}{\text{Pb}_c}$	$\frac{\text{Th}^e}{\text{U}}$	$\frac{^{206}\text{Pb}^f}{^{204}\text{Pb}}$	$\frac{^{206}\text{Pb}^{ag}}{^{238}\text{U}}$	$\pm 2\sigma\%$	$\frac{^{207}\text{Pb}^g}{^{235}\text{U}}$	$\pm 2\sigma\%$	ρ^h	$\frac{^{207}\text{Pb}^g}{^{206}\text{Pb}}$	$\pm 2\sigma\%$
<i>SGC-54: Purple Creek orthogneiss</i>															
L1b	51.59	0.19	51.2	2.5	0.44	3	0.32	218	0.008035	0.38	0.0517	5.0	0.206	0.0468	4.9
s5z	49.362	0.066	50.21	0.72	0.58	11	0.53	688	0.007687	0.13	0.05069	1.5	0.244	0.04792	1.4
s10	49.428	0.057	49.86	0.63	0.32	13	0.35	824	0.0076970	0.12	0.05033	1.3	0.239	0.04752	1.3
s21	49.353	0.059	49.70	0.62	0.47	13	0.36	831	0.0076852	0.12	0.05017	1.3	0.345	0.04744	1.3
zS1	53.618	0.067	53.56	0.65	0.42	13	0.20	855	0.008352	0.12	0.05417	1.2	0.372	0.04713	1.2
zs3	62.942	0.058	63.84	0.53	0.34	19	0.25	1249	0.0098118	0.092	0.06490	0.85	0.303	0.04805	0.83
zS11	49.396	0.086	49.2	1.1	0.40	7	0.18	480	0.007692	0.18	0.0496	2.3	0.293	0.0469	2.2
<i>SGC-2: Rainbow Falls orthogneiss</i>															
s3z	48.172	0.045	48.17	0.46	0.57	15	0.17	1045	0.0075007	0.094	0.04859	0.98	0.273	0.04708	0.96
s4z	52.23	0.13	53.7	1.6	0.57	5	0.22	332	0.008135	0.25	0.0543	3.1	0.234	0.0485	3.0
s9z	48.123	0.074	48.26	0.87	0.59	8	0.26	551	0.007493	0.15	0.04867	1.8	0.226	0.04721	1.8
s23z	56.82	0.10	57.0	1.3	0.81	6	0.19	439	0.008853	0.18	0.0577	2.3	0.226	0.0474	2.3
z22	48.114	0.085	48.2	1.1	1.02	7	0.23	450	0.007492	0.18	0.0486	2.3	0.227	0.0472	2.2
zs5	48.196	0.068	48.24	0.81	0.40	10	0.26	655	0.007504	0.14	0.04866	1.7	0.325	0.04712	1.7
<i>H20FG: 'flecked gneiss'</i>															
z1	47.203	0.038	47.363	0.090	0.38	78	0.18	5129	0.0073492	0.080	0.047751	0.19	0.034	0.047228	0.21
z2	47.199	0.034	47.29	0.24	0.46	26	0.22	1705	0.0073487	0.072	0.04768	0.51	0.663	0.04716	0.47
z3	66.944	0.041	66.87	0.13	0.39	112	0.12	7480	0.0104388	0.061	0.06807	0.21	0.571	0.047370	0.18
z6	47.226	0.034	47.33	0.38	0.90	19	0.33	1232	0.0073528	0.072	0.04771	0.83	0.584	0.04716	0.79
<i>NC-197: Diablo Lake orthogneiss</i>															
z1	44.827	0.054	45.01	0.61	0.61	12	0.28	765	0.0069780	0.12	0.04532	1.4	0.249	0.04721	1.4
z2	44.831	0.040	44.72	0.34	0.70	22	0.27	1421	0.0069786	0.089	0.04502	0.77	0.249	0.04690	0.76
z5	44.884	0.033	44.86	0.15	0.54	57	0.31	3646	0.0069869	0.073	0.04517	0.34	0.422	0.04700	0.32

^a Isotopic dates calculated using the decay constants $\lambda_{238} = 1.55125 \times 10^{-10}$ and $\lambda_{235} = 9.8485 \times 10^{-10}$ of Jaffey et al., (1971).

^b Corrected for initial Th/U disequilibrium using radiogenic ^{208}Pb and $\text{Th}/\text{U}_{\text{magma}} = 4$.

^c Total mass of common Pb.

^d Ratio of radiogenic Pb (including ^{208}Pb) to common Pb.

^e Th contents calculated from radiogenic ^{208}Pb and the Th-corrected $^{206}\text{Pb}/^{238}\text{U}$ date.

^f Measured ratio corrected for fractionation and tracer contribution only.

^g Measured ratios corrected for fractionation, tracer, and blank.

^h Correlation coefficient between Th-corrected $^{206}\text{Pb}/^{238}\text{U}$ and $^{207}\text{Pb}/^{235}\text{U}$ ratios.

Bibliography

- W. Abouchami, A. W. Hofmann, S. J. G. Galer, F. A. Frey, J. Eisele, and M. Feigenson. Lead isotopes reveal bilateral asymmetry and vertical continuity in the Hawaiian mantle plume. *Nature*, 434(7035):851–856, 04 2005. doi: 10.1038/nature03402. URL <http://dx.doi.org/10.1038/nature03402>.
- John Aitchison. The statistical analysis of geochemical compositions. *Mathematical Geology*, 16:531–564, 1984. ISSN 0882-8121. doi: 10.1007/BF01029316. URL <http://dx.doi.org/10.1007/BF01029316>.
- John Aitchison. *The statistical analysis of compositional data*. Chapman & Hall Ltd., London, 1986.
- John Aitchison. On criteria for measures of compositional difference. *Mathematical Geology*, 24:365–379, 1992. ISSN 0882-8121. doi: 10.1007/BF00891269. URL <http://dx.doi.org/10.1007/BF00891269>.
- Francis Albarede and Brian Beard. Analytical methods for non-traditional isotopes. *Reviews in Mineralogy and Geochemistry*, 55(1):113–152, 2004. doi: 10.2138/gsrmg.55.1.113. URL <http://ring.geoscienceworld.org>.
- Francis Albarède, Philippe Telouk, Janne Blichert-Toft, Maud Boyet, Arnaud Agranier, and Bruce Nelson. Precise and accurate isotopic measurements using multiple-collector ICPMS. *Geochimica et Cosmochimica Acta*, 68(12):2725–2744, 6 2004. doi: 10.1016/j.gca.2003.11.024.
- Y. Amelin and W. J. Davis. Isotopic analysis of lead in sub-nanogram quantities by TIMS using a ^{202}Pb - ^{205}Pb spike. *Journal of Analytical Atomic Spectrometry*, 21(10):1053–1061, 2006. doi: <http://dx.doi.org/10.1039/B606842A>. URL <http://dx.doi.org/10.1039/B606842A>.
- Y. Amelin, D. W. Davis, and W. J. Davis. Decoupled fractionation of even- and odd-mass isotopes of Pb in TIMS. *Geochimica et Cosmochimica Acta*, 69(10):A215, 2005.
- Y. Amelin, J. Connelly, R. E. Zartman, J. H. Chen, C. Göpel, and L. A. Neymark. Modern U–Pb chronometry of meteorites: Advancing to higher time resolution reveals new problems. *Geochimica et Cosmochimica Acta*, 73(17):5212–5223, 9 2009. URL <http://www.sciencedirect.com/science/article/pii/S0016703709003172>.

- Yuri Amelin, Alexander N. Krot, Ian D. Hutcheon, and Alexander A. Ulyanov. Lead Isotopic Ages of Chondrules and Calcium-Aluminum-Rich Inclusions. *Science*, 297(5587):1678–1683, 2002. doi: 10.1126/science.1073950. URL <http://www.sciencemag.org/cgi/content/abstract/297/5587/1678>.
- Yuri Amelin, Angela Kaltenbach, Tsuyoshi Iizuka, Claudine H. Stirling, Trevor R. Ireland, Michail Petaev, and Stein B. Jacobsen. U-Pb chronology of the Solar System’s oldest solids with variable $^{238}\text{U}/^{235}\text{U}$. *Earth and Planetary Science Letters*, In Press, Corrected Proof:–, 2010. doi: 10.1016/j.epsl.2010.10.015. URL <http://www.sciencedirect.com/science/article/B6V61-51F818R-1/2/8b42888f0ce9e34d6a3ffff3412419cf>.
- G. Audi, A. H. Wapstra, and C. Thibault. The Ame2003 atomic mass evaluation: (II). Tables, graphs and references. *Nuclear Physics A*, 729(1):337–676, 12 2003. doi: 10.1016/j.nuclphysa.2003.11.003. URL <http://www.sciencedirect.com/science/article/pii/S0375947403018098>.
- J. Brian Balta, Paul D. Asimow, and Jed L. Mosenfelder. Manganese partitioning during hydrous melting of peridotite. *Geochimica et Cosmochimica Acta*, 75(20): 5819 – 5833, 2011. ISSN 0016-7037. doi: 10.1016/j.gca.2011.05.026. URL <http://www.sciencedirect.com/science/article/pii/S0016703711002948>.
- Jacob Bigeleisen. The relative reaction velocities of isotopic molecules. *The Journal of Chemical Physics*, 17(8):675–678, August 1949. doi: doi:10.1063/1.1747368.
- Jacob Bigeleisen. Nuclear size and shape effects in chemical reactions. isotope chemistry of the heavy elements. *Journal of the American Chemical Society*, 118(15): 3676–3680, 1996. doi: 10.1021/ja954076k. URL <http://pubs.acs.org/doi/abs/10.1021/ja954076k>.
- BIPM, IEC, IFCC, ILAC, ISO, IUPAC, IUPAP, and OIML. *Evaluation of measurement data – Supplement to the “Guide to the Expression of uncertainty in measurement” – Propagation of distributions using a Monte Carlo method*, volume JCGM. Joint Committee for Guides in Metrology, 2008a.
- BIPM, IEC, IFCC, ISO, IUPAC, IUPAP, and OIML. *Evaluation of measurement data – Guide to the Expression of Uncertainty in Measurement*. International Organization for Standardization, first edition edition, September 2008b. URL <http://www.measurementuncertainty.org/mu/guide/>.
- Martin Bizzarro, Chad Paton, Kirsten Larsen, Martin Schiller, Anne Trinquier, and David Ulfbeck. High-precision Mg-isotope measurements of terrestrial and extraterrestrial material by HR-MC-ICPMS—implications for the relative and absolute Mg-isotope composition of the bulk silicate Earth. *J. Anal. At. Spectrom.*, 26: 565–577, 2011. doi: 10.1039/C0JA00190B. URL <http://dx.doi.org/10.1039/C0JA00190B>.

- J. K. Böhlke, J. R. de Laeter, P. De Bièvre, H. Hidaka, H. S. Peiser, K. J. R. Rosman, and P. D. P. Taylor. Isotopic compositions of the elements, 2001. *Journal of Physical and Chemical Reference Data*, 34(1):57–67, 2005. doi: 10.1063/1.1836764. URL <http://link.aip.org/link/?JPR/34/57/1>.
- J. F. Bowring, N. M. McLean, and S. A. Bowring. Engineering cyber infrastructure for u-pb geochronology: Tripoli and u-pb_redux. *Geochem. Geophys. Geosyst.*, 12, 06 2011. doi: 10.1029/2010GC003479. URL <http://dx.doi.org/10.1029/2010GC003479>.
- S. A. Bowring, D. H. Erwin, Y. G. Jin, M. W. Martin, K. Davidek, and W. Wang. U/Pb zircon geochronology and tempo of the end-Permian mass extinction. *Science*, 280(5366):1039–1045, 5 1998. doi: 10.1126/science.280.5366.1039. URL <http://www.sciencemag.org/cgi/content/abstract/280/5366/1039>.
- Maud Boyet and Richard W. Carlson. A new geochemical model for the Earth’s mantle inferred from ^{146}Sm – ^{142}Nd systematics. *Earth and Planetary Science Letters*, 250(1-2):254–268, 10 2006. URL <http://www.sciencedirect.com/science/article/pii/S0012821X0600553X>.
- Renee Breedlovestrout. *Paleofloristic Studies in the Paleogene Chuckanut Basin, Western Washington, USA*. PhD thesis, Universit of Idaho, 2010.
- G. A. Brennecka, S. Weyer, M. Wadhwa, P. E. Janney, J. Zipfel, and A. D. Anbar. $^{238}\text{U}/^{235}\text{U}$ variations in meteorites: Extant ^{247}Cm and implications for Pb-Pb dating. *Science*, 327(5964):449–451, 1 2010. doi: 10.1126/science.1180871. URL <http://www.sciencemag.org/cgi/content/abstract/327/5964/449>.
- Louis Briqueu and Henri de la Boisse. U-Pb geochronology: Systematic development of mixing equations and application of Monte Carlo numerical simulation to the error propagation in the Concordia diagram. *Chemical Geology*, 88(1-2):69–83, 10 1990. doi: 10.1016/0009-2541(90)90104-F. URL <http://www.sciencedirect.com/science/article/B6V5Y-4888K84-BX/2/52f560986cd5a5691321d56d37bd899c>.
- Anatoly L. Buchachenko. MIE versus CIE: Comparative analysis of magnetic and classical isotope effects. *Chemical Reviews*, 95(7):2507–2528, 1995. doi: 10.1021/cr00039a009. URL <http://pubs.acs.org/doi/abs/10.1021/cr00039a009>.
- E. J. Catanzao, T. J. Murphy, W. R. Shields, and E. L. Garner. Absolute isotopic abundane ratios of common, equal-atom, and radiogenic lead standards. *Journal of Research of the National Burea of Standards - A. Physics and Chemistry*, 72A(3):261–267, 5 1968.
- E. J. Catanzaro, T. J. Murphy, W. R. Shields, and E. L. Garner. Absolute isotopic abundane ratios of common, equal-atom, and radiogenic lead standards. *Journal of Research of the National Burea of Standards - A. Physics and Chemistry*, 72A(3):261–267, 5 1968.

- Adam J. Charles, Daniel J. Condon, Ian C. Harding, Heiko Pälike, John E. A. Marshall, Ying Cui, Lee Kump, and Ian W. Croudace. Constraints on the numerical age of the Paleocene-Eocene boundary. *Geochem. Geophys. Geosyst.*, 12, 06 2011. doi: 10.1029/2010GC003426. URL <http://dx.doi.org/10.1029/2010GC003426>.
- Daniel J. Condon, Noah McLean, Stephen R. Noble, and Samuel A. Bowring. Isotopic composition ($^{238}\text{U}/^{235}\text{U}$) of some commonly used uranium reference materials. *Geochimica et Cosmochimica Acta*, 74:7127–7143, 2010. URL <http://www.sciencedirect.com/science/article/B6V66-513VRHV-1/2/6f5f2d1f7333e7a2bde7dc7fa77033c8>.
- Daniel J. Condon, R. Blair Schoene, N. M. McLean, R. Parrish, and Samuel A. Bowring. Calibration of the EARTHTIME ^{235}U - ^{233}U - ^{205}Pb -(^{202}Pb) tracer for high-precision geochronology: Part I, metrology and mass spectrometry. submitted to *Geochem. Geophys. Geosyst.*, 2011.
- Maurice G Cox and Bernd R L Siebert. The use of a Monte Carlo method for evaluating uncertainty and expanded uncertainty. *Metrologia*, 43, 2006. doi: 10.1088/0026-1394/43/4/S03. URL <http://stacks.iop.org/0026-1394/43/i=4/a=S03>.
- J. L. Crowley, B. Schoene, and S. A. Bowring. U-Pb dating of zircon in the Bishop Tuff at the millennial scale. *Geology*, 35(12):1123–1126, 12 2007. doi: 10.1130/G24017A.1. URL <http://geology.gsapubs.org/cgi/content/abstract/35/12/1123>.
- G. L. Cumming and J. R. Richards. Ore lead isotope ratios in a continuously changing earth. *Earth and Planetary Science Letters*, 28(2):155–171, 12 1975. doi: 10.1016/0012-821X(75)90223-X. URL <http://www.sciencedirect.com/science/article/B6V61-472616D-75/2/ee67530e441462e2931beb09e6d82ca2>.
- Vladimir I. Davydov, James L. Crowley, Mark D. Schmitz, and Vladislav I. Poletaev. High-precision U-Pb zircon age calibration of the global Carboniferous time scale and Milankovitch band cyclicity in the Donets Basin, eastern Ukraine. *Geochem. Geophys. Geosyst.*, 11(2), 02 2010. doi: 10.1029/2009GC002736. URL <http://dx.doi.org/10.1029/2009GC002736>.
- A. P. Dempster, N. M. Laird, and D. B. Rubin. Maximum likelihood from incomplete data via the EM algorithm. *Journal of the Royal Statistical Society. Series B (Methodological)*, 39(1):1–38, 1977. URL <http://www.jstor.org/stable/2984875>.
- R Doucelance and G Manhès. Reevaluation of precise lead isotope measurements by thermal ionization mass spectrometry: comparison with determinations by plasma source mass spectrometry. *Chemical Geology*, 176(1-4):361–377, 7 2001. doi: 10.1016/S0009-2541(00)00409-5. URL <http://www.sciencedirect.com/science/article/pii/S0009254100004095>.

- J. Egozcue, V. Pawlowsky-Glahn, G. Mateu-Figueras, and C. Barceló-Vidal. Isometric logratio transformations for compositional data analysis. *Mathematical Geology*, 35 (3):279–300, 2003. doi: 10.1023/A:1023818214614. URL <http://dx.doi.org/10.1023/A:1023818214614>.
- Vladimir N. Epov, Dmitry Malinovskiy, Frank Vanhaecke, Didier Bégué, and Olivier F.X. Donard. Modern mass spectrometry for studying mass-independent fractionation of heavy stable isotopes in environmental and biological sciences. *J. Anal. At. Spectrom.*, 26:1142–1156, 2011. doi: 10.1039/C0JA00231C. URL <http://dx.doi.org/10.1039/C0JA00231C>.
- James E. Evans. Paleoclimatology and paleobotany of the Eocene Chumstick Formation, Cascade Range, Washington (USA): a rapidly subsiding alluvial basin. *Palaeogeography, Palaeoclimatology, Palaeoecology*, 88:239–264, 1991.
- James E. Evans and Samuel Y. Johnson. Paleogene strike-slip basins of central Washington: Swauk Formation and Chumstick Formation. In N. L. Joseph et al., editors, *Geologic guidebook for Washington and adjacent areas*, volume 86, pages 215–238. Washington Division of Geology and Earth Resources Information Circular, 1989.
- James E. Evans and John Ristow, Jr. Depositional history of the southeastern outcrop belt of the Chuckanut Formation: implications for the Darrington – Devil’s Mountain and Straight Creek fault zones, Washington (U.S.A.). *Canadian Journal of Earth Sciences*, 31:1727–1743, 1994.
- Z. Fekiacova, W. Abouchami, S. J. G. Galer, M. O. Garcia, and A. W. Hofmann. Origin and temporal evolution of Koolau Volcano, Hawaii: Inferences from isotope data on the Koolau Scientific Drilling Project (KSDP), the Honolulu volcanics and ODP site 843. *Earth and Planetary Science Letters*, 261(1-2):65–83, 9 2007. URL <http://www.sciencedirect.com/science/article/pii/S0012821X07003676>.
- H. Gerstenberger and G. Haase. A highly effective emitter substance for mass spectrometric Pb isotope ratio determinations. *Chemical Geology*, 136(3-4):309–312, 4 1997. doi: 10.1016/S0009-2541(96)00033-2. URL <http://www.sciencedirect.com/science/article/pii/S0009254196000332>.
- Gene H. Golub. Some modified matrix eigenvalue problems. *SIAM Review*, 15(2): 318–334, 04 1973. URL <http://www.jstor.org/stable/2028604>.
- Randall L. Gresens, Charles W. Naeser, and John W. Whetten. Stratigraphy and age of the Chumstick and Wenatchee Formations: Tertiary fluvial and lacustrine rocks, Chiwaukum graben, Washington. *Geological Society of America Bulletin*, 92:841–876, 1981.
- K. Habfast. Fractionation correction and multiple collectors in thermal ionization isotope ratio mass spectrometry. *International Journal of Mass Spectrometry*, 176 (1-2):133–148, 1998. ISSN 1387-3806. doi: 10.1016/S1387-3806(98)14030-7. URL <http://www.sciencedirect.com/science/article/pii/S1387380698140307>.

- R. A. Haugerud, P. Van der Heyden, R. W. Tabor, J. S. Stacey, and R. E. Zartman. Late Cretaceous and early Tertiary plutonism and deformation in the Skagit Gneiss Complex, North Cascade range, Washington and British Columbia. *Geological Society of America Bulletin*, 103:1297–1307, 1991.
- Joe Hiess, Daniel J. Condon, Noah M. McLean, and Stephen R. Noble. $^{238}\text{U}/^{235}\text{U}$ systematics in terrestrial U-bearing minerals. *Science*, in review.
- Robert S. Hildebrand. Did westward subduction cause Cretaceous–Tertiary orogeny in the North American Cordillera? *Geological Society of America Special Papers*, 457:1–71, 2009. doi: 10.1130/2009.2457. URL <http://specialpapers.gsapubs.org/content/457/1.abstract>.
- Albrecht Hofmann. Fractionation corrections for mixed-isotope spikes of Sr, K, and Pb. *Earth and Planetary Science Letters*, 10(4):397–402, 3 1971. doi: 10.1016/0012-821X(71)90087-2. URL <http://www.sciencedirect.com/science/article/pii/0012821X71900872>.
- Todd Housh and Samuel A. Bowring. Lead isotopic heterogeneities within alkali feldspars: Implications for the determination of initial lead isotopic compositions. *Geochimica et Cosmochimica Acta*, 55(8):2309–2316, 8 1991. doi: 10.1016/0016-7037(91)90106-F. URL <http://www.sciencedirect.com/science/article/B6V66-48C8K4P-14F/2/30235361c6b892d3259306fe541e58c0>.
- Richard J. Howarth. A history of regression and related model-fitting in the earth sciences (1636?–2000). *Natural Resources Research*, 10:241–286, 2001. ISSN 1520-7439. doi: 10.1023/A:1013928826796. URL <http://dx.doi.org/10.1023/A:1013928826796>.
- A. H. Jaffey, K. F. Flynn, L. E. Glendenin, W. C. Bentley, and A. M. Essling. Precision measurement of half-lives and specific activities of ^{235}U and ^{238}U . *Phys. Rev.*, C(4):1889–1906, 1971.
- Samuel Y. Johnson. Stratigraphy, age, and paleogeography of the Eocene Chuckanut Formation, northwest Washington. *Canadian Journal of Earth Sciences*, 21:92–106, 1984.
- G. F. Kessinger, T. Huett, and J. E. Delmore. Ag ion formation mechanisms in molten glass ion emitters. *International Journal of Mass Spectrometry*, 208(1-3):37–57, 7 2001. doi: 10.1016/S1387-3806(01)00378-5. URL <http://www.sciencedirect.com/science/article/pii/S1387380601003785>.
- F. L. King, J. Teng, and R. E. Steiner. Glow discharge mass spectrometry: Trace element determinations in solid samples. *Journal of Mass Spectrometry*, 30:1061–1075, 1995.
- T. E. Krogh. Strontium isotopic variation and whole rock isochron studies in the Grenville Province of Ontario. *MIT Annual Progress Reports (AEC Contract AT(30-1)-1381)*, 12:73, 1964.

- Alexander Kukush and Sabine Van Huffel. Consistency of elementwise-weighted total least squares estimator in a multivariate errors-in-variables model $AX = B$. *Metrika*, 59(1):75–97, February 2004. doi: 10.1007/s001840300272. URL <http://dx.doi.org/10.1007/s001840300272>.
- K. Levenberg. A method for the solution of certain non-linear problems in least squares. *Quarterly Journal of Applied Mathematics*, II(2):164–168, 1944.
- K Ludwig. Calculation of uncertainties of U-Pb isotope data. *Earth and Planetary Science Letters*, 46(2):212–220, January 1980. ISSN 0012821X. doi: 10.1016/0012-821X(80)90007-2. URL [http://dx.doi.org/10.1016/0012-821X\(80\)90007-2](http://dx.doi.org/10.1016/0012-821X(80)90007-2).
- Kenneth Ludwig. Errors of isotope ratios acquired by double interpolation. *Chemical Geology*, 268(1-2):24–26, 10 2009. doi: 10.1016/j.chemgeo.2009.07.004. URL <http://www.sciencedirect.com/science/article/B6V5Y-4WTHS7T-1/2/ce2da3710374a3a2552e4d6553f0b015>.
- Kenneth R. Ludwig. On the treatment of concordant uranium-lead ages. *Geochimica et Cosmochimica Acta*, 62(4):665–676, 2 1998a. doi: 10.1016/S0016-7037(98)00059-3. URL <http://www.sciencedirect.com/science/article/B6V66-3WGXV6P-9/2/f2afc361c113e043be479a90a110ac4e>.
- Kenneth R. Ludwig. On the treatment of concordant uranium-lead ages. *Geochimica et Cosmochimica Acta*, 62(4):665–676, 2 1998b. doi: 10.1016/S0016-7037(98)00059-3.
- Kenneth R. Ludwig. *Isoplot/Ex Version 3.00: A Geochronological Toolkit for Microsoft Excel*. Berkeley Geochronology Center, 2003. Special Publication 4, 73 p.
- Kenneth R. Ludwig and D. M. Titterton. Calculation of isochrons, ages, and errors. *Geochimica et Cosmochimica Acta*, 58(22):5031–5042, 11 1994. doi: 10.1016/0016-7037(94)90229-1.
- Louis Lyons, Duncan Gibaut, and Peter Clifford. How to combine correlated estimates of a single physical quantity. *Nuclear Instruments and Methods in Physics Research Section A: Accelerators, Spectrometers, Detectors and Associated Equipment*, 270(1):110–117, 7 1988. doi: 10.1016/0168-9002(88)90018-6. URL <http://www.sciencedirect.com/science/article/B6TJM-473DBY1-M/2/b585b7c1896787399c53868631a2376c>.
- Chloé Nadia Maréchal, Philippe Télouk, and Francis Albarède. Precise analysis of Cu and Zn isotopic compositions by plasma-source mass spectrometry. *Chemical Geology*, 156(1-4):251–273, 4 1999. doi: 10.1016/S0009-2541(98)00191-0. URL <http://www.sciencedirect.com/science/article/pii/S0009254198001910>.

- Ivan Markovsky and Sabine Van Huffel. Overview of total least-squares methods. *Signal Processing*, 87(10):2283 – 2302, 2007. ISSN 0165-1684. doi: 10.1016/j.sigpro.2007.04.004. URL <http://www.sciencedirect.com/science/article/pii/S0165168407001405>. Special Section: Total Least Squares and Errors-in-Variables Modeling.
- Ivan Markovsky, Maria Luisa Rastello, Amedeo Premoli, Alexander Kukush, and Sabine Van Huffel. The element-wise weighted total least-squares problem. *Comput. Stat. Data Anal.*, 50:181–209, January 2006. ISSN 0167-9473. doi: 10.1016/j.csda.2004.07.014. URL <http://dl.acm.org/citation.cfm?id=1647955.1648009>.
- Donald W. Marquardt. An algorithm for least-squares estimation of nonlinear parameters. *SIAM J. Appl. Math.*, 11(2):431–441, 1963. doi: 10.1137/0111030.
- James M. Mattinson. Ages of zircons from the Northern Cascade Mountains, Washington. *Geological Society of America Bulletin*, 83(12):3769–3784, 12 1972. URL <http://gsabulletin.gsapubs.org/content/83/12/3769.abstract>.
- James M. Mattinson. Anomalous isotopic composition of lead in young zircons. *Carnegie Institution Year Book*, 72:613–616, December 1973.
- James M. Mattinson. Zircon U-Pb chemical abrasion (“CA-TIMS”) method: Combined annealing and multi-step partial dissolution analysis for improved precision and accuracy of zircon ages. *Chemical Geology*, 220(1-2):47–66, JUL 12 2005a. ISSN 0009-2541. doi: 10.1016/j.chemgeo.2005.03.011.
- James M. Mattinson. Zircon U–Pb chemical abrasion (‘CA-TIMS’) method: Combined annealing and multi-step partial dissolution analysis for improved precision and accuracy of zircon ages. *Chemical Geology*, 220(1-2):47–66, 2005b. doi: doi:10.1016/j.chemgeo.2005.03.011. URL <http://www.sciencedirect.com/science/article/pii/S0009254105001452>.
- James M. Mattinson. Analysis of the relative decay constants of ^{235}U and ^{238}U by multi-step CA-TIMS measurements of closed-system natural zircon samples. *Chemical Geology*, 275(3-4):186–198, 8 2010. doi: doi:10.1016/j.chemgeo.2010.05.007. URL <http://www.sciencedirect.com/science/article/pii/S0009254110001713>.
- Jennifer E.P. Matzel, Samuel A. Bowring, and Robert B. Miller. Time scales of pluton construction at differing crustal levels: Examples from the Mount Stuart and Tenpeak intrusions, North Cascades, Washington. *Geological Society of America Bulletin*, 118(11-12):1412–1430, 2006. doi: 10.1130/B25923.1. URL <http://gsabulletin.gsapubs.org/content/118/11-12/1412.abstract>.
- Matthew J. McClincy. Tephrostratigraphy of the Chumstick Formation. Master’s thesis, Portland State University, 1986.

- N. M. McLean. Straight line regression through data with correlated uncertainties in two or more dimensions. submitted to *Geochim. et Cosmochim. Acta*, 2011.
- N. M. McLean, J. F. Bowring, and S. A. Bowring. An algorithm for U-Pb isotope dilution data reduction and uncertainty propagation. *Geochem. Geophys. Geosyst.*, 12, 06 2011. doi: 10.1029/2010GC003478.
- Zachary D. Michels. Structure of the central Skagit Gneiss Complex, North Cascades, Washington. Master's thesis, San José State University, 2008.
- Robert B. Miller and Samuel A. Bowring. Structure and chronology of the Oval Peak batholith and adjacent rocks: Implications for the Ross Lake fault zone, North Cascades, Washington. *Geological Society of America Bulletin*, 102(10):1361–1377, 1990. doi: 10.1130/0016-7606(1990)102. URL <http://gsabulletin.gsapubs.org/content/102/10/1361.abstract>.
- Robert B. Miller and Scott R. Paterson. Influence of lithological heterogeneity, mechanical anisotropy, and magmatism on the rheology of an arc, North Cascades, Washington. *Tectonophysics*, 342(3-4):351–370, 2001. doi: doi:10.1016/S0040-1951(01)00170-6. URL <http://www.sciencedirect.com/science/article/pii/S0040195101001706>.
- Robert B. Miller, Stacia M. Gordon, Samuel A. Bowring, Brigid A. Doran, Noah M. McLean, Zachary D. Michels, Erin K. Shea, Donna L. Whitney, Niki E. Wintzer, and Morgan K. Mendoza. Linking deep and shallow crustal processes in an exhumed continental arc, North Cascades, Washington. In J. E. O'Connor, editor, *Volcanoes to Vineyards: Geologic Field Trips through the Dynamic Landscape of the Pacific Northwest*, number 15. Geological Society of America Field Guide, 2009.
- Peter Misch. Tectonic evolution of the northern Cascades of Washington State – a west Cordilleran case history. *Canadian Institute of Mining and Metallurgy*, Special Volume 8:101–148, 1966.
- S. Moorbath, P. N. Taylor, J. L. Orpen, P. Treloar, and J. F. Wilson. First direct radiometric dating of Archaean stromatolitic limestone. *Nature*, 326(6116):865–867, 04 1987. doi: 10.1038/326865a0. URL <http://dx.doi.org/10.1038/326865a0>.
- G. E. Mustoe, R. M. Dillhoff, and T.A. Dillhoff. Geology and paleontology of the early Tertiary Chuckanut Formation. In P. Stelling and D. S. Tucker, editors, *Floods, Faults, and Fire: Geological Field Trips in Washington State and Southwest British Columbia*, number 9, pages 121–135. Geological Society of America Field Guide, 2007.
- Claire Patterson. Age of meteorites and the earth. *Geochimica et Cosmochimica Acta*, 10(4):230–237, 10 1956. doi: 10.1016/0016-7037(56)90036-9. URL <http://www.sciencedirect.com/science/article/B6V66-488Y22W-19/2/bee1c1b35dcf7c455915938e05f008cb>.

- V. Pawlowsky-Glahn and J. J. Egozcue. Compositional data and their analysis: an introduction. *Geological Society, London, Special Publications*, 264(1):1–10, 2006. doi: 10.1144/GSL.SP.2006.264.01.01. URL <http://sp.lyellcollection.org/content/264/1/1.abstract>.
- Roger Powell, Janet Hergt, and Jon Woodhead. Improving isochron calculations with robust statistics and the bootstrap. *Chemical Geology*, 185(3-4):191–204, 5 2002. doi: 10.1016/S0009-2541(01)00403-X. URL <http://www.sciencedirect.com/science/article/pii/S000925410100403X>.
- Paul R. Renne, Roland Mundil, Greg Balco, Kyoungwon Min, and Kenneth R. Ludwig. Joint determination of ^{40}K decay constants and $^{40}\text{Ar}^*/^{40}\text{K}$ for the Fish Canyon sanidine standard, and improved accuracy for $^{40}\text{Ar}/^{39}\text{Ar}$ geochronology. *Geochimica et Cosmochimica Acta*, 74(18):5349–5367, 9 2010. URL <http://www.sciencedirect.com/science/article/pii/S0016703710003571>.
- Matthew Rioux, Samuel Bowring, Frank Dudás, and Richard Hanson. Characterizing the U–Pb systematics of baddeleyite through chemical abrasion: application of multi-step digestion methods to baddeleyite geochronology. *Contributions to Mineralogy and Petrology*, 160:777–801, 2010. ISSN 0010-7999. doi: 10.1007/s00410-010-0507-1. URL <http://dx.doi.org/10.1007/s00410-010-0507-1>.
- J. C Roddick. Generalized numerical error analysis with applications to geochronology and thermodynamics. *Geochimica et Cosmochimica Acta*, 51(8):2129–2135, 8 1987. URL <http://www.sciencedirect.com/science/article/B6V66-488Y4V5-1JV/2/a50fdfe0228a3a291cc130d8f58a1db5>.
- Charles M. Rubin, Jason B. Saleeby, Darrel S. Cowan, Mark T. Brandon, and Michael F. McGroder. Regionally extensive mid-Cretaceous west-vergent thrust system in the northwestern Cordillera: Implications for continent-margin tectonism. *Geology*, 18(3):276–280, 1990. doi: 10.1130/0091-7613(1990)018<0276:REMCWV>2.3.CO;2. URL <http://geology.gsapubs.org/content/18/3/276.abstract>.
- W. A. Russell, D. A. Papanastassiou, and T. A. Tombrello. Ca isotope fractionation on the Earth and other solar system materials. *Geochimica et Cosmochimica Acta*, 42(8):1075–1090, 8 1978. doi: 10.1016/0016-7037(78)90105-9.
- Stephane Scaillet. Numerical error analysis in $^{40}\text{Ar}/^{39}\text{Ar}$ dating. *Chemical Geology*, 162(3-4):269–298, 1 2000. doi: 10.1016/S0009-2541(99)00149-7. URL <http://www.sciencedirect.com/science/article/B6V5Y-3Y9V0PJ-4/2/14fd9ad2abcd3a914b8e74fe8a6a8500>.
- Urs Schärer. The effect of initial ^{230}Th disequilibrium on young U–Pb ages: the Makalu case, Himalaya. *Earth and Planetary Science Letters*, 67(2):191–204, 2 1984. doi: 10.1016/0012-821X(84)90114-6. URL <http://www.sciencedirect.com/science/article/B6V61-476F232-3P/2/a0d758f5f1c07cbe078f81d8fc56cc36>.

- Edwin A. Schauble. Role of nuclear volume in driving equilibrium stable isotope fractionation of mercury, thallium, and other very heavy elements. *Geochimica et Cosmochimica Acta*, 71(9):2170–2189, 5 2007. doi: 10.1016/j.gca.2007.02.004. URL <http://www.sciencedirect.com/science/article/pii/S0016703707000798>.
- Mark D. Schmitz and Blair Schoene. Derivation of isotope ratios, errors, and error correlations for U-Pb geochronology using ^{205}Pb - ^{235}U -(^{233}U)-spiked isotope dilution thermal ionization mass spectrometric data. *Geochem. Geophys. Geosyst.*, 8(8), 08 2007. doi: 10.1029/2006GC001492. URL <http://dx.doi.org/10.1029/2006GC001492>.
- Blair Schoene and Samuel Bowring. U-Pb systematics of the McClure Mountain syenite: thermochronological constraints on the age of the $^{40}\text{Ar}/^{39}\text{Ar}$ standard MMhb. *Contributions to Mineralogy and Petrology*, 151(5):615–630, 5 2006. doi: 10.1007/s00410-006-0077-4. URL <http://dx.doi.org/10.1007/s00410-006-0077-4>.
- Blair Schoene, James L. Crowley, Daniel J. Condon, Mark D. Schmitz, and Samuel A. Bowring. Reassessing the uranium decay constants for geochronology using ID-TIMS U-Pb data. *Geochimica et Cosmochimica Acta*, 70(2):426–445, 1 2006. doi: doi:10.1016/j.gca.2005.09.007. URL <http://www.sciencedirect.com/science/article/pii/S0016703705007714>.
- Blair Schoene, Maarten J. de Wit, and Samuel A. Bowring. Mesoarchean assembly and stabilization of the eastern kaapvaal craton: A structural-thermochronological perspective. *Tectonics*, 27(5), 10 2008. doi: 10.1029/2008TC002267. URL <http://dx.doi.org/10.1029/2008TC002267>.
- R. A. Sohn and W. Menke. Application of maximum likelihood and bootstrap methods to nonlinear curve-fit problems in geochemistry. *Geochem. Geophys. Geosyst.*, 3(7), 07 2002. doi: 10.1029/2001GC000253. URL <http://dx.doi.org/10.1029/2001GC000253>.
- R. R. Sokal and F. J. Rohlf. *Biometry: the principles and practice of statistics in biological research*. W. H. Freeman and Co., New York, 3rd edition, 1995.
- J Stacey and J Kramers. Approximation of terrestrial lead isotope evolution by a two-stage model. *Earth and Planetary Science Letters*, 26(2):207–221, June 1975. ISSN 0012821X. doi: 10.1016/0012-821X(75)90088-6. URL [http://dx.doi.org/10.1016/0012-821X\(75\)90088-6](http://dx.doi.org/10.1016/0012-821X(75)90088-6).
- R.H. Steiger and E. Jager. Subcommittee on geochronology: Convention on the use of decay constants in geo- and cosmochronology. *Earth and Planetary Science Letters*, 36(3):359 – 362, 1977. ISSN 0012-821X. doi: 10.1016/0012-821X(77)90060-7. URL <http://www.sciencedirect.com/science/article/B6V61-473FFKD-4R/2/7bf332e11c594a99cfbb5e21a8e5ce81>.

- Claudine H. Stirling, Morten B. Andersen, Emma-Kate Potter, and Alex N. Halliday. Low-temperature isotopic fractionation of uranium. *Earth and Planetary Science Letters*, 264(1-2):208–225, 12 2007. doi: 10.1016/j.epsl.2007.09.019. URL <http://www.sciencedirect.com/science/article/B6V61-4PT2988-8/2/807894a1e0571d6540837615c7755890>.
- R. W. Tabor, V. A. Frizzell, J. A. Vance, and C. W. Naeser. Ages and stratigraphy of lower and middle Tertiary sedimentary and volcanic rocks of the central Cascades, Washington: Application to the tectonic history of the Straight Creek fault. *Geological Society of America Bulletin*, 95(1):26–44, 1984.
- R. W. Tabor, Virgil A. Frizzell, J. T. Whetten, R. B. Waitt, D. A. Swanson, G. R. Byerly, D. B. Booth, M. J. Hetherington, and R. E. Zartman. *Geologic Map of the Chelan 30-minute by 60-minute Quadrangle, Washington*. U.S. Geological Survey Miscellaneous Investigations Series Map I-1661, 1987.
- R. W. Tabor, R. A. Haugerud, W. Hildreth, and E. H. Brown. *Geologic map of the Mount Baker 30- by 60-minute quadrangle, Washington*. U.S. Geological Survey Miscellaneous Investigations Series Map I-2660, 2003.
- Albert Tarantola. *Inverse Problem Theory and Methods for Model Parameter Estimation*. SIAM, Philadelphia, Pennsylvania, 2005.
- Albert Tarantola and Bernard Valette. Generalized nonlinear inverse problems solved using the least squares criterion. *Review of Geophysics and Space Physics*, 20:219–232, 1982a.
- Albert Tarantola and Bernard Valette. Inverse problems = quest for information. *Journal of Geophysics*, 50:159–170, 1982b.
- M. F. Thirlwall. Inter-laboratory and other errors in Pb isotope analyses investigated using a ^{207}Pb - ^{204}Pb double spike. *Chemical Geology*, 163(1-4):299–322, 2 2000. doi: 10.1016/S0009-2541(99)00135-7. URL <http://www.sciencedirect.com/science/article/pii/S0009254199001357>.
- D. Michael Titterton and Alex N. Halliday. On the fitting of parallel isochrons and the method of maximum likelihood. *Chemical Geology*, 26(3-4):183–195, 9 1979. doi: 10.1016/0009-2541(79)90045-7. URL <http://www.sciencedirect.com/science/article/pii/0009254179900457>.
- Andrea Valassi. Combining correlated measurements of several different physical quantities. *Nuclear Instruments and Methods in Physics Research Section A: Accelerators, Spectrometers, Detectors and Associated Equipment*, 500(1-3):391–405, 3 2003. doi: 10.1016/S0168-9002(03)00329-2. URL <http://www.sciencedirect.com/science/article/B6TJM-47T1SRS-3/2/8ed1207a06872deb312324a1a4434611>.

- Sabine Van Huffel and Ivan Markovsky. *The Total Least Squares Problem: Computational Aspects and Analysis*, volume 9 of *Frontiers in Applied Mathematics*. SIAM, Philadelphia, Pennsylvania, 1991.
- Sabine Van Huffel and Joos Vandewalle. Analysis and properties of the generalized total least squares problem $AX \approx B$ when some or all columns in A are subject to error. *SIAM J. Matrix Anal. & Appl.*, 10(3):294–315, July 1989. doi: doi/10.1137/0610023.
- A. Verbruggen, R. Eykens, F. Kehoe, H. Kühn, S. Richter, and Y. Aregbe. Preparation and certification of IRMM-3636, IRMM-3636a and IRMM-3636b. Technical report, JRC Scientific and Technical Reports, 2008. URL <http://publications.jrc.ec.europa.eu/repository/handle/111111111/4450>.
- Pieter Vermeesch. Helioplot, and the treatment of overdispersed (U-Th-Sm)/He data. *Chemical Geology*, 271(3-4):108–111, 3 2010. doi: 10.1016/j.chemgeo.2010.01.002. URL <http://www.sciencedirect.com/science/article/B6V5Y-4Y5GY1B-2/2/0daf855520cd5f1606717bb69762cae7>.
- Jeff D. Vervoort, Terry Plank, and Julie Prytulak. The Hf–Nd isotopic composition of marine sediments. *Geochimica et Cosmochimica Acta*, 75(20):5903–5926, 2011. ISSN 0016-7037. doi: 10.1016/j.gca.2011.07.046. URL <http://www.sciencedirect.com/science/article/pii/S0016703711004443>.
- I. Wendt and C. Carl. The statistical distribution of the mean squared weighted deviation. *Chemical Geology: Isotope Geoscience section*, 86(4):275–285, 4 1991. doi: 10.1016/0168-9622(91)90010-T. URL <http://www.sciencedirect.com/science/article/pii/016896229190010T>.
- Brian Wernicke and Stephen R. Getty. Intracrustal subduction and gravity currents in the deep crust: Sm–Nd, Ar–Ar, and thermobarometric constraints from the Skagit Gneiss Complex, Washington. *Geological Society of America Bulletin*, 109(9):1149–1166, 1997. doi: 10.1130/0016-7606(1997)109. URL <http://gsabulletin.gsapubs.org/content/109/9/1149.abstract>.
- S. Weyer, A. D. Anbar, A. Gerdes, G. W. Gordon, T. J. Algeo, and E. A. Boyle. Natural fractionation of $^{238}\text{U}/^{235}\text{U}$. *Geochimica et Cosmochimica Acta*, 72(2):345–359, 1 2008. doi: 10.1016/j.gca.2007.11.012. URL <http://www.sciencedirect.com/science/article/B6V66-4R644RK-4/2/5ebeb2870133d985f31ab26de4330818>.
- D. L. Whitney. High pressure metamorphism in the western Cordillera of North America: an example from the Skagit Gneiss, North Cascades, Washington. *Journal of Metamorphic Geology*, 10:71–85, 1992.
- Donna L. Whitney, Scott R. Paterson, Keegan L. Schmidt, Allen F. Glazner, and Christopher F. Kopf. Growth and demise of continental arcs and orogenic plateaux in the North American Cordillera: from Baja to British Columbia. *Geological Society, London, Special Publications*, 227(1):167–175, 2004. doi: 10.1144/GSL.

- SP.2004.227.01.09. URL <http://sp.lyellcollection.org/content/227/1/167.abstract>.
- Niki E. Wintzer. Structure of the Skagit Gneiss in the Diablo Lake area, North Cascades, WA. Master's thesis, San José State University, 2009.
- Derek York. Least-squares fitting of a straight line. *Canadian Journal of Physics*, 44: 1079, 1966.
- Derek York. Least squares fitting of a straight line with correlated errors. *Earth and Planetary Science Letters*, 5:320–324, 1968. doi: 10.1016/S0012-821X(68)80059-7.
- Derek York, N. M. Evensen, M. L. Martinez, and J. D. Delgado. Unified equations for the slope, intercept, and standard errors of the best straight line. *American Journal of Physics*, 72(3):367–375, 3 2004. ISSN 0002-9505. doi: 10.1119/1.1632486.
- Edward D. Young, Albert Galy, and Hiroko Nagahara. Kinetic and equilibrium mass-dependent isotope fractionation laws in nature and their geochemical and cosmochemical significance. *Geochimica et Cosmochimica Acta*, 66(6):1095 – 1104, 2002. ISSN 0016-7037. doi: 10.1016/S0016-7037(01)00832-8. URL <http://www.sciencedirect.com/science/article/pii/S0016703701008328>.
- Junjun Zhang, Nicolas Dauphas, Andrew M. Davis, and Ali Pourmand. A new method for MC-ICPMS measurement of titanium isotopic composition: Identification of correlated isotope anomalies in meteorites. *J. Anal. At. Spectrom.*, pages –, 2011. doi: 10.1039/C1JA10181A. URL <http://dx.doi.org/10.1039/C1JA10181A>.